tions of the Astronomy Department of
the Eötvös Loránd University
No.11.

NATIONAL POSTGRADUATE REUNION IN ASTRONOMY & ASTROPHYSICS

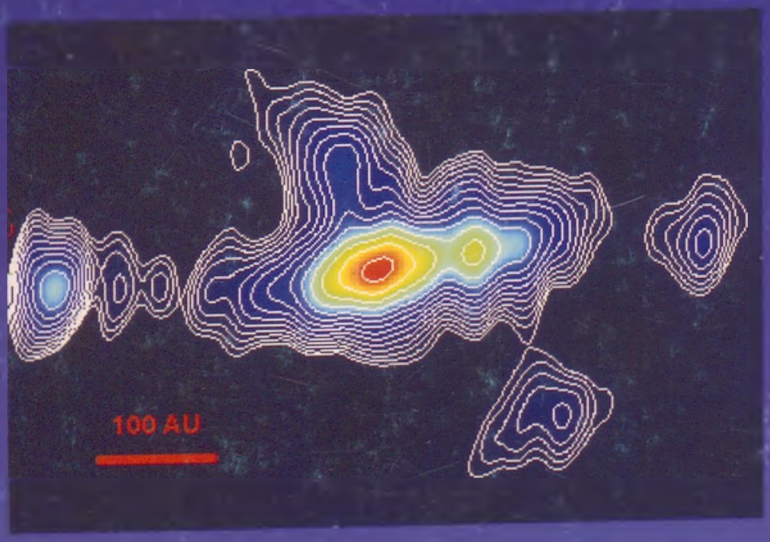

Hungary, November 2000

Edited by
E. Forgács-Dajka and Zs. Sándor

Budapest 2001

Publications of the Department of Astronomy of
the Eötvös Loránd University
No.11.

National Postgraduate Reunion in Astronomy & Astrophysics

Hungary, November 2000

EDITED BY
E. Forgács-Dajka and Zs. Sándor

ORGANISING COMMITTEE
Z. Kolláth (President)
D. Marik and Sz. Csizmadia

Published by the Department of Astronomy of the Eötvös University and
the Konkoly Observatory of the Hungarian Academy of Science
Budapest 2001

ISBN 963 463 480 X
HU ISSN 0238-2423
Responsible editor: dr. Bálint Érdi

Cover: The inner radio structure of SS433, a galactic X-ray binary star, as observed at 1.6 GHz with the European and US VLBI networks on June 6, 1998. The equatorial emission region (discovered by Paragi et al. 1999, A & A 348, 910) nearly perpendicular to the E-W radio jet direction is quasi-symmetrical to the location of the central engine (a black hole or neutron star).

Contents

Solar Physics

Variable Stars

Other areas of Astronomy

Preface

This meeting of postgraduate students in Astronomy and Astrophysics was a result of two independent initiatives of the Department of Astronomy of Eötvös University and Konkoly Observatory of the Hungarian Academy of Sciences. Although this workshop was the first occasion for the PhD students to meet, present and discuss their research, the organizers would like to start a tradition. Lectures were presented from diverse fields of astronomy and we hope that the reader can find in this book worthy and interesting ideas and results.
The speakers gave their talks covering the following areas of astronomy:

- Binary and Multiple Stellar Systems
- Celestial Mechanics
- Extragalactic Astronomy
- Infrared Astronomy
- Solar Physics
- Variable Stars
- Other areas of Astronomy

The meeting was held at the Konkoly Observatory during November 16-17, 2000. The participants thank the staff of the Konkoly Observatory for the warm hospitality. We are grateful to Konkoly Observatory, to the Department of Astronomy of the Eötvös University and to the National Federation of PhD Students for their financial support.

The Editors

List of Participants

Name	Address
Bakos, G.Á.	Konkoly Observatory H-1525 Budapest, P.O.Box 67., Hungary bakos@konkoly.hu
Bíró, I.B.	Baja Astronomical Observatory of Bács-Kiskun County H-6500, Baja, Szegedi út, P.O.Box 766., Hungary barna@electra.bajaobs.hu
Borkovits, T.	Baja Astronomical Observatory of Bács-Kiskun County H-6500, Baja, Szegedi út, P.O.Box 766., Hungary borko@electra.bajaobs.hu
Budavári, T.	Eötvös Loránd University Department of Physics of Complex Systems H-1117 Budapest, Pázmány P. sétány 1/A, Hungary budavari@complex.elte.hu
Csillik, I.	"Babeş–Bolyai" University, Astronomical Observatory 3400 Cluj-Napoca, str. Cireşilor, nr. 19, Romania iharka@math.ubbcluj.ro
Csizmadia, Sz.	Konkoly Observatory H-1525 Budapest, P.O.Box 67., Hungary csizmadia@konkoly.hu
Forgács-Dajka, E.	Eötvös Loránd University Department of Astronomy H-1518 Budapest, P.O.Box 32., Hungary andro@astro.elte.hu
Frey, S.	FÖMI Satellite Geodetic Observatory, Penc H-1373 Budapest, P.O. Box 546., Hungary frey@sgo.fomi.hu
Kiss, Cs.	Konkoly Observatory H-1525 Budapest, P.O.Box 67., Hungary pkisscs@astro.elte.hu
Kiss, L.L.	University of Szeged Department of Experimental Physics H-6720 Szeged, Dóm tér 9., Hungary l.kiss@physx.u-szeged.hu

Kolláth, Z.	Konkoly Observatory H-1525 Budapest, P.O.Box 67., Hungary kollath@konkoly.hu
Marik, D.	Eötvös Loránd University Department of Astronomy H-1518 Budapest, P.O.Box 32., Hungary dmarik@astro.elte.hu
Moór, A.	Eötvös Loránd University Department of Astronomy H-1518 Budapest, P.O.Box 32., Hungary moor@astro.elte.hu
Paragi, Zs.	FÖMI Satellite Geodetic Observatory, Penc H-1373 Budapest, P.O. Box 546., Hungary paragi@sgo.fomi.hu
Pócs, M.	Konkoly Observatory H-1525 Budapest, P.O.Box 67., Hungary pocs@konkoly.hu
Regály, Zs.	Eötvös Loránd University Institute for Theoretical Physics H-1117 Budapest, Pázmány P. sétány 1/A, Hungary regaly@matrix.elte.hu
Sándor, Zs.	Eötvös Loránd University Department of Astronomy H-1518 Budapest, P.O.Box 32., Hungary szsolt@astro.elte.hu
Süli, Á.	Eötvös Loránd University Department of Astronomy H-1518 Budapest, P.O.Box 32., Hungary saron@astro.elte.hu
Szabó, Gy.	University of Szeged Department of Experimental Physics H-6720 Szeged, Dóm tér 9., Hungary szgy@neptun.physx.u-szeged.hu
Szabó, R.	Konkoly Observatory H-1525 Budapest, P.O.Box 67., Hungary rszabo@konkoly.hu

Varga, E.

Eötvös Loránd University
Department of Astronomy
H-1518 Budapest, P.O.Box 32., Hungary
vemese@astro.elte.hu

Photometric analysis of eclipsing cataclysmic variables

Imre Barna Bíró
Baja Astronomical Observatory of Bács-Kiskun County
H-6500, Baja, Szegedi út, P.O.Box 766., Hungary
E-mail:barna@electra.bajaobs.hu

Abstract

Eclipsing cataclysmic variables provide the best opportunity for studying accretion discs. Information on the intensity distribution of the disc is convolved in the eclipse profile, and may be restored using the Eclipse Mapping method. Radial temperature profiles can be reconstructed from multivawelength light curves, and can be used for testing theoretical models. This paper describes the development and tests of a customly written eclipse mapping code. As an application, results on the novalike variable DW UMa are presented briefly.
Keywords: *stars: cataclysmic variables, accretion discs*

1. Introduction

Cataclysmic variables are all known to be semi-detached binary systems, with mass transfer proceeding from the less massive secondary towards the white dwarf primary, producing an accretion disc around it. Processes connected to the disc are held responsible for the vehement nature of these systems (classical and dwarf nova outbursts, flickering). An excellent review of cataclysmic variables is given in Warner (1995).

The accretion disc is generally the brightest component of these systems. This is why they are most appropriate for studying accretion discs as astrophysical object, many details of which are yet to be unraveled. In *eclipsing* cataclysmic variables the primary eclipse od caused by periodic occultation of the accretion disc by the much fainter secondary. The intensity distribution of the disc is therefore coded in the eclipse profile (though in a highly convolved

form), and can be restored in principle. Apart from direct model fitting, the Eclipse Mapping method is frequently used for this purpose, as it makes minimal assumptions on the physical properties of the disc. Moreover, the position of an eventual bright spot at the stream impact location can also be determined.

2. The Eclipse Mapping Method

The method of Eclipse Mapping was introduced by Horne (1985a) and is described in detail there. Here only the main idea is given. The shape of the secondary can be approximated by its critical Roche-lobe. This, together with the mass ratio and inclination of the system (related to each other via the eclipse half-width, see Horne 1985b), determines the geometry of the eclipses. Fig. 1 shows a modeled eclipse of a standard flat accretion disc, with mass ratio $q = 0.35$, inclination $i = 75°$ and disc radius of 0.8 X_{L_1}. Occultation of the disc

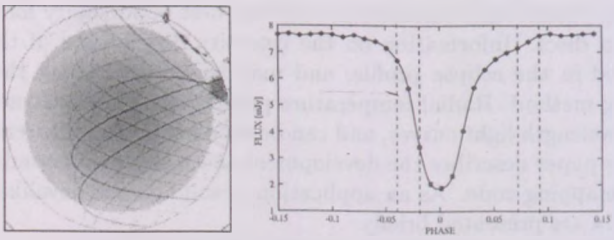

Figure 1: Eclipse geometry in cataclysmic vatriables. *Left*: a model brightness distribution on the accretion disc (in inverse scale), overlaid with arches of ingress/egress. *Right*: the resulting light curve. Thick arches and dashed lines correspond to ingress and egress phases of the bright spot.

occurs along arches of constant ingress and egress phases, corresponding to the projection of the secondary's shadow on the disc (as seen by the observer) [1]. Digitizing the disc into N pixels and having M phase points, the light curve can be determined as $d_\varphi = \sum_{k=1}^{N} R_{\varphi k} f_k \quad (\varphi = 1 \ldots M)$, or $\underline{\mathbf{d}} = \underline{\underline{\mathbf{R}}}\,\underline{\mathbf{f}}$, where $\underline{\mathbf{f}}$ is the intensity map of the disc (N pixels), $\underline{\mathbf{d}}$ holds the light curve (M data), and $\underline{\underline{\mathbf{R}}}$ is the convolution matrix of the problem ($R_{\varphi k}$ is the visibility of the k. pixel at phase φ). Generally $N \gg M$, therefore the inverse problem is badly

[1] From this point of view, the problem shows much similarity with Medical Tomography, the disc corresponding to the human body, the arches to the path of the X-ray through it and the observed change in intensity to the light attenuation in the body along the arch. See Horne 1985a for discussion.

underdetermined, with many different maps fitting the data within error. The eclipse mapping exploits the Maximum Entropy Method as a further selection criterion, introduced by Jaynes (1957), and used widely in various scientific areas (medicine, chemistry; see Narayan & Nityananda 1986 for a review of its applications in astronomy). The idea is to select the simplest map (i.e. with the least information content) consistent with the data. It can be shown on the basis of Bayesian probability theory that this can be achieved by maximizing the *informational entropy* $S(\mathbf{f}) = -\sum_{j=1}^{N} (f_j/A_j)\,[\ln(f_j/A_j) - 1]$ relative to a *default map* $\underline{\mathbf{A}}$, which codes our *prior* knowledge or expectation about the intensity map. The maximization is made subject to a constraint on the fit to the data, measured by some statistics (usually chi-square, but see Baptista & Steiner 1993 for improvemed statistics).

The Eclipse Mapping was succesfully applied to reconstruct the accretion disc intensity maps in several cataclysmics (see Wood 1992 and Warner 1995 for examples). Performing the reconstructions in several bandpasses (from multicolor photometric data) provides inferences on the radiation properties of the disc, distance estimates by main sequence fitting (considering each pixel as a star) and radial temperature profiles, which then can be compared with theory. (e.g. the $T_{\rm eff} \propto R^{-3/4}$ prediction of the standard alfa-disc model).

3. The code

Various procedures can be employed in performing the constrained maximization $S = \max|_{C=C_{\rm aim}}$. The one used here implements a general algorithm constructed by Skilling & Bryan (1984). It exploits Lagrange multipliers to convert the problem to a series of unconstrained maximizations, which are solved by a modified conjugate gradients method. The light curve synthesis is heavily employed by the algorithm for computing the goodness-of-fit and for building up the conjugate search directions. Therefore, this part has to be coded efficiently. A further refinement was introduced by calculating fractional visibilites for each pixel (instead of simple 0/1 values). This is important especially for low resolutions. The model assumes a fully opaque and dark secondary filling its critical Roche-lobe exactly and circular rotation. The accretion disc is allowed to have an opening angle and a rim on its edge; moreover, arbitrary pixel masks can also be used to simulate for example a disc with a central hole (believed to be present in intermediate polar systems). A polar grid is used for dividing the disc into pixels; the applied resolution is chosen so that the spatial resolution be equivalent with the mean phase resolution of the light curve.

The default map controls the property to be measured by the entropy, and can be chosen to drive the algorithm towards a specific type of solution. Two cases are of interest here: 1) a constant default map provides the "smoothest" solution, which restores the positions of intensity peaks (central bulge or bright spot), but smears the radial structure, and 2) a "most axisymmetric" solution is achieved by using the azimuthally average of the result of the last iteration as the current default map, together with a limited radial blurring; this restores the radial profile, but smears out any excentric peak into a ring.

4. Tests

Testing the performance of the code was done with light curves generated artificially from steady-state, optically thick accretion disc models, with the addition of different gaussian noise levels. Fig. 2 summarizes the results for two such noise levels. It can be seen that the radial temperature profile structure is acceptably reconstructed even from medium to low quality data.

Tests also showed some limited capability of the method to establish reasonable limits on the geometrical parameters and any uneclipsed light; the set of values for which the entropy of the reconstructed map is the highest proved to give a reasonable estimate of the real parameters. This does not work, however, in case of large departures from axisymmetry (e.g. prominent bright spots).

5. Application: eclipse mapping of DW UMa

The algorithm was used to investigate the accretion disc in the novalike variable DW UMa. The results are summarized in Fig. 3 (a geometrically flat disc was assumed; for details see Bíró 2001). Color-magnitude diagrams of the reconstructed maps suggest and optically thick disc; nevertheless, the temperature profiles deviate significantly from the standard model. Two alternative explanations have been examined. A self-occulting thick disc model did not resolve the discrepancy, although recently Knigge et al. (2000) have arived on this conclusion based on spectroscopic data. A disrupted disc with an inner hole radius of 0.1 X_{L_1} could explain the apparent flatness, suggesting that DW UMa might be an intermediate polar (similar results have been found for V Per, Wood et al. 1992). Although there is some observational evidence supporting the presence of a weak magnetic field (specific emission lines and sporadic quasi-periodic oscillations), it is not enough for differentiating among the above assumptions.

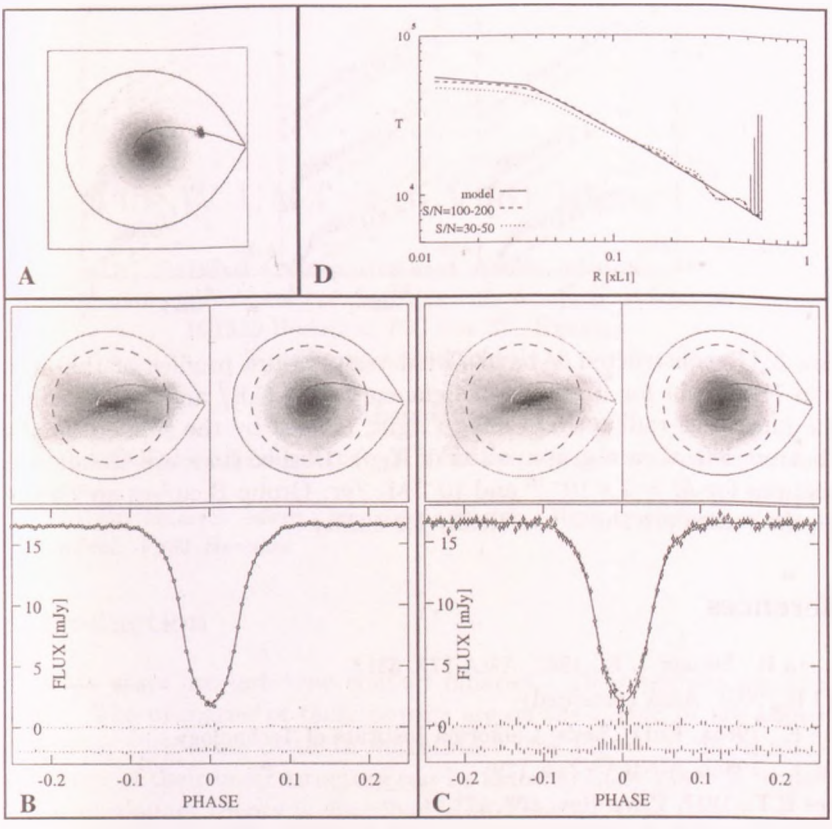

Figure 2: Results on testing the MEM code. **Panel A**: the model. **Panel B**: reconstruction, S/N = 100-200. *Top left/right*: most uniform/axisymmetric case; *Bottom*: fits and residuals. **Panel C**: same as **B**, except S/N = 30-50. **Panel D**: the reconstructed temperature profiles (most axysimmetric solution).

Acknowledgements

This work pas supported in part by the OTKA T030743 National Grant.

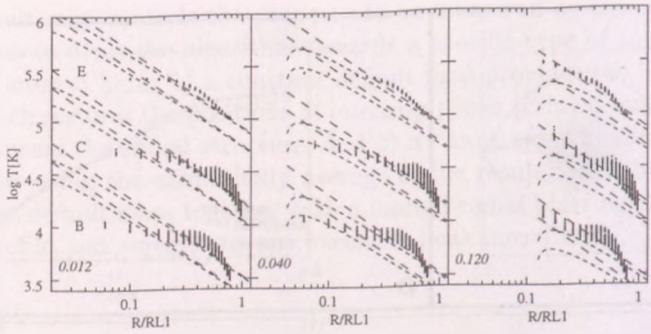

Figure 3: Reconstructed V-band radial temperature profiles of the accretion disc in DW UMa for 3 groups of light curves (B,C,E) and 3 different values of the inner disc radius (from left to right, labeled by the slanted numbers in the bottom left of each graph, units of X_{L_1}). Dashed lines are standard model predictions for $\dot{M} = 2 \times 10^{-10}$ and $10^{-9} M_\odot$/yr. Group B curves are on the true scale, the others are shifted vertically for clarity.

References

Baptista R., Steiner J. E., 1993, A&A 277, 331

Bíró I.B., 2001, A&A (accepted)

Horne K., 1985a, PhD Thesis, California Institute of Technology

Horne K., 1985b, MNRAS 213, 129

Jaynes E.T., 1957, Phys. Rev. 108, 171

Knigge C., Long K. S, Hoard D., et al., 2000, ApJ 539, L49

Narayan R., Nityananda R., 1986, ARA&A 24, 127

Skilling J., Bryan R. K., 1984, MNRAS 211, 111

Spruit H. C., 1994, A&A 289, 441

Warner B., 1995, *Cataclysmic Variable Stars*, Cambr. Astr. Ser. Vol. 28, CUP

Wood J. H., 1992, in: APS Conf. Ser. 56, pp. 48

Wood J. H., Abbott T. M. C., Shafter A. W., 1992, ApJ 393, 729

The W UMa star V861 Herculis

Szilárd Csizmadia and Attila Molnár
Konkoly Observatory of the Hungarian Academy of Sciences
H-1525 Budapest, P.O.Box 67., Hungary
E-mail: csizmadia@konkoly.hu

Abstract

The first CCD $V(RI)_C$ light-curve of V861 Herculis will be presented and analysed.
KEYWORDS:*binaries: close - binaries: eclipsing - stars: evolution - stars: individual: V861 Herculis*

1. Introduction

The W UMa stars are late-type contact binaries. Their periods are smaller than 1 day. The primaries of these objects are on the ZAMS or are above the main-sequence with some of tenth magnitudes (see Figure 3. in Mochnacki, 1981). Theory of their inner structure can be found in Lucy 1968a,b. Presently accepted evolutionary theory is described in Mochnacki, 1981.

Period variations are present in every well-studied cases (Kreiner, 1977), but the physical mechanism of the short- as well as long-term variations is not known (for a review of the possible reasons see Kalimeris et. al, 1994 and van't Veer, 1991).

The shape of the light-curve of the W UMa stars are also variable in time scales of the order of months or years. The O'Connell-effect (which means that there are differences between the height of the maxima) is frequently present and its rate can be even 0.1 magnitude high and it and can vary.

The importance of studying of poorly observed W UMa-stars is explicated in Maceroni & van't Veer (1996). One of such systems is V861 Her.

V861 Herculis = Antipin 44 = GSC 3079 - 201 is a recently discovered W UMa star with $P = 0.3446322$ day. Its maximum brightness is at $V = 13.09$ magnitude and at the maximum the colour index $(B-V) = 0.63$ (Antipin, 1997).

According to our knowledge there are no available photometric or spectrosocopic data for this faint system.

2. The light curve

To get a precise multi-colour light curve we observed V861 Her on five nights in 2000, using the 102cm RCC-telescope of the Konkoly Observatory. The instrument, the detector, the reduction steps and the details of the standard transformation are described in Csizmadia & Sándor, 2000. At the first quadrature ($\phi = 0.25$) the $V(RI)_C$ magnitudes of V861 Her are: $V = 12.79, V - R = 0.34, V - I = 0.74$. (We note that there is some difference between Antipin's V value and our one ($\Delta V = 0.3$ mag.).) Since GSC 3079 - 194 and 3079 - 192 have very similar colours, V861 Her was measured to these stars. Figure 1 shows the $V(RI)_C$ light curves.

The light-curve of V861 Her shows a remarkable O'Connell-effect (0.05 magnitude in V).

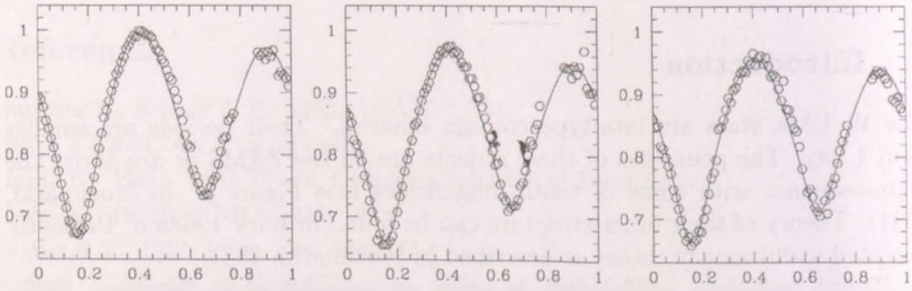

Figure 1: Phased light curves of V861 Her in V (left), in R (middle) and in I (right). The lines are the light-curve solution

3. Light-curve solution

The modelling of the light-curve of V861 Her is difficult because of the large O'Connell-effect and the unknown spectroscopical mass ratio.

In order to construct a modell we used the Wilson-Devinney Method (Wilson & Devinney, 1971, Wilson, 1979, 1998). The initial parameters were estimated by the following way: T_1, T_2 from a $[(V-I) \rightarrow T_{eff}]$ transformation (Bessell et

Table 1: Light-curve solution parameter set of V861 Herculis

Parameter	Value	Parameter	Value
Φ_γ	-0.3465 ± 0.0008	third light	0
i	64.74 ± 0.18	$\Omega_1 = \Omega_2$	3.36520
$T_1(K)$	$5474 \pm 84\ K$	$T_2(K)$	$6361 \pm 25\ K$
$q = M_2/M_1$	0.820 ± 0.005	$(\frac{L_1}{L_1+L_2})_V$	0.378 ± 0.004
$(\frac{L_1}{L_1+L_2})_R$	0.407 ± 0.007	$(\frac{L_1}{L_1+L_2})_I$	0.423 ± 0.009
r_1 (pole)	0.3846 ± 0.0016	r_2 (pole)	0.3515 ± 0.0017
r_1 (side)	0.4073 ± 0.0021	r_2 (side)	0.3705 ± 0.0022
r_1 (back)	0.4435 ± 0.0031	r_2 (back)	0.4090 ± 0.0035

al, 1998); $x_V = 0.600, x_R = 0.510, x_I = 0.430$ (see tables of Al-Naimy (1978), we applied the linear limb-darkening law); $F_1 = F_2 = 1.0, A_1 = A_2 = 1.0, g_1 = g_2 = 0.32$ (see the meanings of the symbols e.g. in Borkovits & Bíró, 1999). The following parameters were adjusted: i (inclination), $\Omega_1 = \Omega_2$ (a linear non-dimensional function of the surface gravity potential, see Wilson, 1979), $L_1/(L_1 + L_2)$ (fractional luminosity of primary), phase-shift and q (mass-ratio). Because of the difference between the depth of the minima we allowed some temperature-difference between the components.

In a standard way the O'Connell effect is explained by star-spot activity. Introducing a polar spot, as suggested by Maceroni & van't Veer (1993), the fitting was better than the unspotted solution, however the residuals remained too high. Therefore we applied a second spot and later the longitudes and latitudes of the spots were also adjusted. The final solution is presented in Table 1-2.

The view of the system can be seen in Figure2

4. Disscussions

4.1. Distance

In order to estimate the absolute magnitude of V861 Her we used two different methods.

Table 2: Spot-parameters

Star	longitude (deg)	latitude (deg)	angular radius (deg)	ΔT
1	-43 ± 8	128 ± 15	94 ± 9	$+62K$
2	-82 ± 6	91 ± 13	65 ± 4	$-619K$

The first one is based on the $M_V = M_V(P, CI, i)$ calibration of W UMa stars (Rucinski & Duerbeck, 1997). From our light-curve solution we got $i = 64.74$ deg. Antipin (1997) determined $P = 0.34463$ and $(B - V) = 0.63$. In the direction of V861 Her $E_{B-V} = 0.02$ (Schlegel et al., 1998) and using the basic equation $A_V = 3.0E_{B-V}$ we found $A_V = 0.06$. Thus we got $M_V = 3.97 \pm 0.60$. From this the distance can be estimated 596 ± 161 pc.

The second method is based on the assumption on thermal eqillibrium of the components. According to the solution this is an approximation. In this case the colour index of the system is equal to the colour index of one of the components. After a $[(V - I) \rightarrow M_V]$ transformation (assuming $[Fe/H] > 0.3$, Hawley et al., 1999) we got $M_V = 4.91$. Because the minima is almost equal the system is brighter than this with about 0.75 magnitude. Therefore the M_V of the system is 4.16 magnitude. The distance is 547 ± 250 pc.

The final distance estimation is 583 ± 183 pc with a weight 3 of the first method.

4.2. Absolute dimensions

One can write that $M_V = 4.62 - 2.5log\frac{L_1+L_2}{L_\odot}$. From the light-curve solution we know the ratio of the luminosities. Combining this with the previous definition we can compute $L_1 and L_2$. Using the modell-temperatures the average radii can be computed, too. From Kepler's third law the average densities can be determined and therefore the masses can be estimeted, too. The distance between the centres of the components was computed from the equation $A = \frac{1}{2}(\frac{R_1}{r_1} + \frac{R_2}{r_2})$. The results are presented in Table 3.

Table 3: Absolute dimension of system V861 Herculis

Parameter	Value	Parameter	Value
L_1	$0.69L_\odot$	L_2	$1.13L_\odot$
R_1	$0.92R_\odot$	R_2	$0.88R_\odot$
ρ_1	$1.321g/cm^3$	ρ_2	$1.437g/cm^3$
M_1	$0.72M_\odot$	M_2	$0.68M_\odot$
A	$2.26R_\odot$		

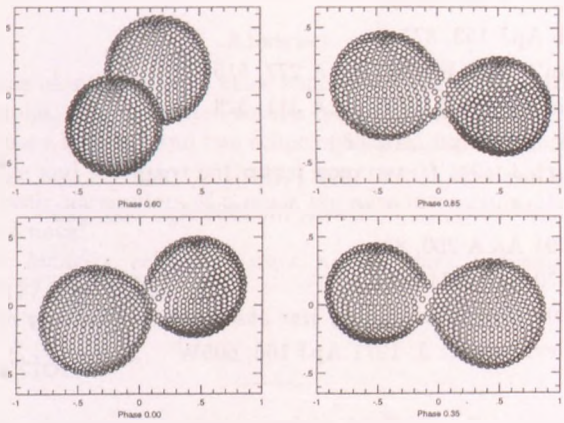

Figure 2: The view of the system at four different phases

5. Future work

In order to determine the mass-ratio it would be need spectroscopic measurements from the systems.

The determination of the exact period and the presence of possible period-variations need further minima-observations. The expected variability of the O'Connell-effect needs new multi-colour light-curves in the next years.

References

Al-Naimy, H. M. 1978 AP&SS 53, 181

Antipin, S. V. 1997 IBVS No. 4360

Borkovits T., Bíró I. B., 1998 A&A 349, 515

Csizmadia Sz., Sándor Zs. 2000, IBVS in prep.

Bessell, M. S., Castelli, F., Plez, B. 1998 A&A 333, 231

Hawley, S. L., Tourtellot, J. G., Reid, I. N. 1999 AJ, 117 1341

Kalimeris, A, Rovithis-Livaniou, H., Rovithis, P., Oprescu, G., Dumitrescu, A., Suran, M.D. A&A 291, 765

Kreiner J.M., 1977 in: *The Interaction of Variable Stars with their Environment* Proc. of IAU Colloq. 42. Ed.: R. Kippenhahn, J. Rahe & W. Strohmeier

Lucy, L.B. 1968a ApJ 151, 1123

Lucy, L.B. 1968b ApJ 153, 877

Maceroni, C., van't Veer, F. 1993 A&A 277, 515

Maceroni, C., van't Veer, F. 1996 A&A 311, 523

Mochnacki, S. W. 1981 ApJ, 245, 630

Rucinski, S. M., Duerbeck, H. W. 1997 PASP 109, 1340

Schlegel, D. J., Finkbeiner, D, P., Davis, M, 1998 ApJ 500, 525

van't Veer, F. 1991 A&A 250, 84

Wilson, R. E. 1979 ApJ, 234 1054

Wilson, R. E. 1998 *Computing binary star observables*, University of Florida

Wilson, R. E., Devinney, E. J. 1971 ApJ 166, 605W

Observational examples of interaction in close binary systems

László L. Kiss
Department of Experimental Physics, University of Szeged
H-6720 Szeged, Dóm tér 9., Hungary
E-mail: l.kiss@physx.u-szeged.hu

Abstract

Various forms of interaction in close binaries are illustrated with observational examples. The presented results include period studies of the sdB eclipsing binary HW Vir and two eclipsing central stars of planetary nebulae (UU Sge and V477 Lyr). Optical spectra of V1494 Aql are used to determine basic parameters of a much stronger interaction, the outburst of a classical nova*.
Keywords: *binaries: eclipsing – stars: novae – stars: individual: HW Vir, UU Sge, V477 Lyr, V1494 Aql*

1. Introduction

Close binary stars (here we restrict ourselves to $P_{orb} < 1^d$) show many forms of interaction during their evolution. The slowly changing orbital elements, mass-transfer or magnetic braking may result in observable period variation, thus the primary indicator is the orbital period. Eclipsing binaries are the best examples where the accurate period determination ($\delta P/P \sim 10^{-9}$) allows studying very fine systematic changes. On the other hand, some classes of close binaries suffer much stronger interaction, namely dramatic mass-transfer processes via accretion disks. Classical novae show one of the most energetic events caused by thermonuclear runaway on the surface of the white dwarf primaries. In those cases the interaction could be studied more directly, for instance, with help of high-resolution spectroscopy.

*Based on data obtained at the David Dunlap Observatory, University of Toronto

The main aim of this paper is to illustrate different cases of interactions through recent photometric and spectroscopic observations. The presented results cover the period variations of the sdB eclipsing binary HW Virginis and two eclipsing binary planetary nebula central stars (UU Sagittae and V477 Lyrae), while low- and medium-resolution spectra gave some basic parameters of the outburst of the classical nova V1494 Aquilae (Nova Aquila 2000 No.2).

2. Observations

CCD photometric observations of HW Vir were obtained at the University of Szeged using a 0.28-m Schmidt-Cassegrain telescope located in the very center of the city of Szeged on four night in May, 2000. The detector was an SBIG ST-6 CCD camera (30 sec exposures). The eclipsing binary PN nuclei were observed at the Piszkéstető Station of Konkoly Observatory with the 60/90/180 cm Schmidt-telescope on 5 nights in August, 2000. The detector was a Photometrics AT200 CCD camera (1536x1024 pixels, KAF-1600 chip with UV-coating). All photometric reductions (image processing, digital photometry) were done with the corresponding IRAF tasks.

We obtained digital objective-prism spectra of HW Vir at the Piszkéstető Station of Konkoly Observatory with the same instrument as above supplemented with an objective prism (refracting angle: 5°, 580 Å/mm image scale at Hγ). The wavelength- and flux-calibrated spectra were also used to calculate standard Cousins VRI differential light curves relative to a comparison star located on the same field of view.

The spectroscopic observations of V1494 Aql were carried out with the Cassegrain-spectrograph attached to the 1.88-m telescope of the David Dunlap Observatory (Richmond Hill, Canada). The spectra were obtained on four nights in December, 1999. The detector was a Thomson 1024x1024 CCD chip. A low resolution broad band spectrum was taken on the first night of observations, while we took only medium resolution spectra to study the line profiles in detail on the following three nights.

3. Results

3.1. HW Virginis

HW Vir is one of the brightest members of the pre-cataclysmic binaries, in which the primary component is a hot subdwarf or white dwarf star, while the secondary is a main-sequence K or M-type dwarf. Eclipsing pre-cataclysmic

binaries offer a very good opportunity to determine absolute parameters being representative in this important evolutionary phase.

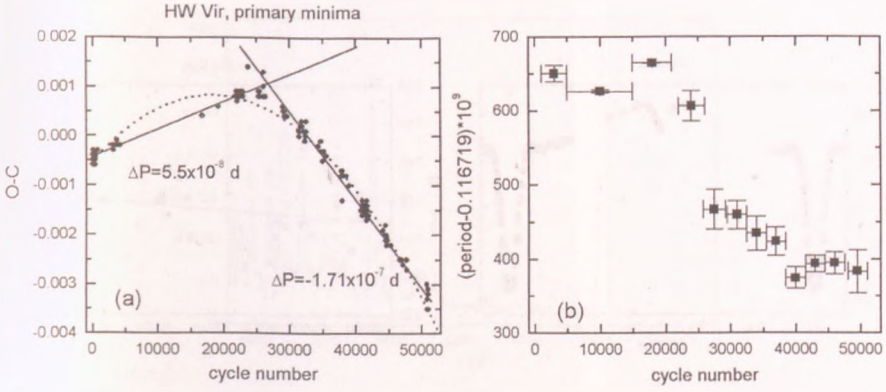

Figure 1: Left: the O−C diagram of HW Vir; right: changes of the instantaneous period

The eclipsing binary nature of HW Vir ($P_{orb} = 0.1167$ d) was discovered by Menzies (1986). Since then the continuous eclipse timings revealed a strong period decrease around 1991, see Kilkenny et al. (1994). Our work addressed the recent behaviour of the period change.

Nine new epochs of minimum have been determined from the CCD photometric and objectiv prism spectrophotometric observations. We have collected all available times of minimum from the literature. The resulting O−C diagram is shown in the left panel of Fig.1. The overall appearance can be described with two linear fits supporting the sudden change of the period. Short-term changes are described with the "instantaneous" period (right panel of Fig.1). Obviously, there have been additional smooth changes beside the large decrease.

The reason for the sudden period change is still unknown. Commonly, it is assumed, that mass transfer may be responsible, however in a detached system such as HW Vir it is not expected. Nevertheless, adopting mass transfer, the primary star had to transfer a mass of about $\sim 3.5 \cdot 10^{-5}$ $M_{\odot}$. It is unclear why such an event would occur. One could consider outer accretion, e.g., engulfing a planet-size body. The required mass (double the amount above to get the same change of the mass-ratio) is only in the range of tens of Earth masses, however, since we have no additional data, this is only rough speculation. Further physical

parameters of HW Vir have been presented in Kiss et al. (2000a).

3.2. UU Sagittae and V477 Lyrae

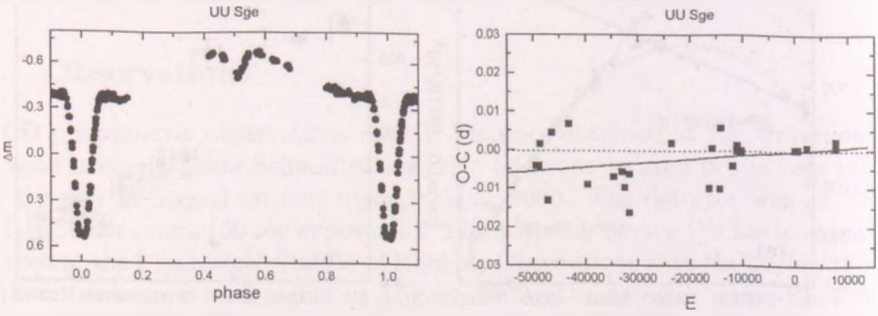

Figure 2: Left: the phase diagram; right: the O−C diagram of UU Sge

Eclipsing binary central stars of planetary nebulae are key objects in determining absolute parameters of central compact systems through light curve modelling. Although eight such objects are listed in the catalog of Ritter & Kolb (1998), only two of them, UU Sge and V477 Lyr are well-covered by the observations. Earlier studies suggested possible period changes which was the subject of our work.

Both stars have orbital periods about 0.5 d, thus we could not cover the whole cycles. However, six epochs of minimum could be determined from the new CCD photometric light curves. They have been added to the full lists of minima collected from the literature. The main question was the stability of the orbital periods in these detached binaries where strong interaction is not expected thanks to the relatively large separation of the components.

The resulting light curve (phased with the adopted ephemeris) and O−C diagram of UU Sge are plotted in Fig.2. The main conclusion is that there is only weak evidence for possible period change in UU Sge, while we could not detect definite period variation in V477 Lyr. A slightly improved ephemeris for UU Sge is HJD(Min.I)=2451766.5285+0.46506921·E. In the case of V477 Lyr, the earlier ephemeris of Pollacco & Bell (1994) has not been surpassed (more details can be found in Kiss et al. (2000b)).

3.3. Nova (V1494) Aquilae 2000 No. 2

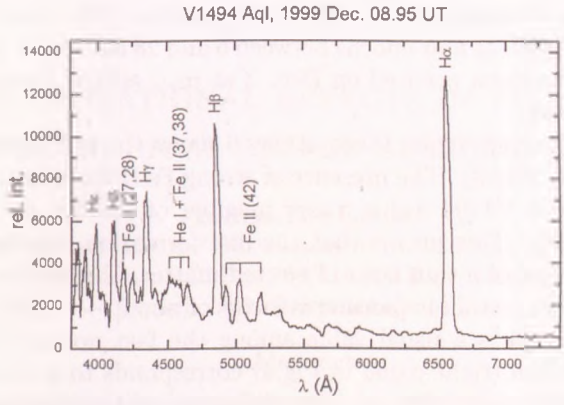

Figure 3: The whole optical spectrum of V1494 Aql showing the strong hydrogen and iron emission lines

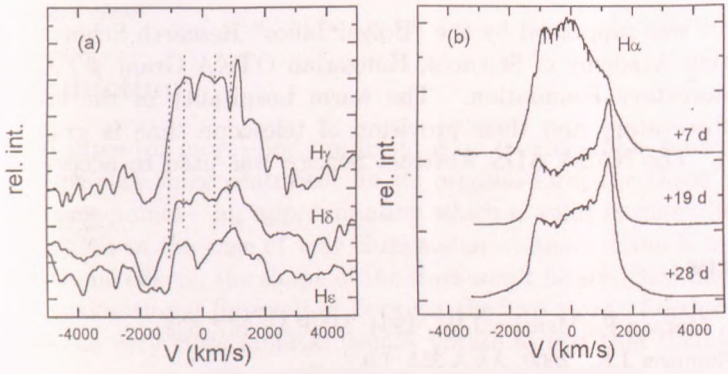

Figure 4: Left: three Balmer series line profiles with similar P Cyg-structures implying an expansion velocity of ~ -1900 km s^{-1}. Right: the evolution of the Hα line.

V1494 Aql was the brightest nova in the northern hemisphere after Nova (V1500) Cygni 1975, therefore, it provided a good opportunity to carry out

thorough studies of a nova explosion by various instruments. It was discovered visually by A. Pereira on Dec. 1.875 UT, 1999 at magnitude m_{vis}=6.0. The spectroscopic confirmation was given by subsequent low-resolution observations revealing hydrogen Balmer series with P Cyg-profiles. We have followed the spectroscopic evolution at four epochs between 6 and 28 days after the maximum brightness (the maximum occured on Dec. 3 at $m_{vis} \approx 4.0$). Here we outline a few basic conclusions.

The low-resolution spectrum taken at day 6 shows the principal plus diffuse-enhanced spectrum (Fig.3). The presence of strong Fe II multiplets with P Cyg-profiles suggests that V1494 Aql is a new member of the "Fe II" class defined by Williams (1992). This means that the line formation happens in a post-outburst wind instead of a thin layer of ejected matter. The medium-resolution hydrogen profiles suggest an expansion velocity of about ~ -1900 km s^{-1} (left panel in Fig.4), which is a usual value among the fast novae. The observed saddle-shaped Hα line (right panel in Fig.4) corresponds to an equatorial ring seen most probably nearly edge-on. The difference of the blue and red peaks in the Hα can be associated with possible small-scale clumpiness in the shell. Further discussion can be found in Kiss & Thomson (2000).

Acknowledgments

This research was supported by the "Bolyai János" Research Scholarship from the Hungarian Academy of Sciences, Hungarian OTKA Grant #T032258 and Szeged Observatory Foundation. The warm hospitality of the staff of the Konkoly Observatory and their provision of telescope time is gratefully acknowledged. The NASA ADS Abstract Service was used to access data and references.

References

Kilkenny D., Marang F., Menzies J.W., 1994, MNRAS 267, 535

Kiss L.L., Thomson J.R., 2000, A&A 355, L9

Kiss L.L., Csák B., Szatmáry K., Fűrész G., Sziládi K., 2000, A&A 364, 199

Kiss L.L., Kasza J., Borza S., 2000, IBVS No. 4962

Menzies J.W., 1986, Ann. Rep. S. Afr. Astron. Obs. 1985, p.20

Pollacco D.L., Bell S.A., 1994, MNRAS 267, 452

Ritter H., Kolb U., 1998, A&AS 129, 83

Williams R.E., 1992, AJ 104, 725

Tidal and rotational effects in the evolution of hierarchical triple stellar systems

Tamás Borkovits
Baja Astronomical Observatory of Bács-Kiskun County
Szegedi út, P.O. Box 766, H-6500 Baja, Hungary
E-mail: borko@electra.bajaobs.hu

Abstract

A new numerical integrator was developed by the author for studying together the orbital and spin evolution of hierarchical triple stellar systems. The code includes equilibrium tide approximations with arbitrary direction of rotational axes. After an introduction of the main features of the physical model the results of the first runs are illustrated.
Keywords: *Celestial mechanics, stellar dynamics – Stars: multiple – binaries: close*

1. Introduction

The general three-(or more)-body problem is an inexhaustible source of topics for several scholars since centuries. In its original form the three bodies are treated as mass-points – an approximation which is valid in many fields of astronomy, but not in the case of very close stellar systems. Even if we omit the non-gravitational effects, the shape of the stars won't be spherical due to purely the strong gravitational interaction between the two stars. Furthermore, the members of the very close binaries usually rotate so fast that their oblateness gives another non-spherical contribution to their gravitational field. These effects may be strong enough to cause observable orbital changes on a time scale of years. Here we refer especially the apsidal motion observed in several eclipsing binaries.

Furthermore, as a star is neither rigid, nor unviscous, as the (tidal) forces acting upon it changes, its shape varies, causing some dissipation of the potential energy, the effect called as tidal dissipation. There are two principle formalisms

for discussing this effect: the "equilibrium tide" model and the "dynamical tide" one. (For a very short description of the two methods see the introduction of Eggleton et al. 1998.)

Recently Kiseleva et al. (1998) studied the effects of tidal friction in triple stars with numeric integration based on the model of Eggleton et al. (1998). The relatively more sophisticated model of the equilibrium tides and tidal friction of Kopal (1978) was used by the present author to study simultaneously the orbital motion of hierarchical triple systems (containing two distorted stars consisting of linear viscous fluid rotating uni-axially around an arbitrarily directed axis, and a more distant third body treated as a mass-point), and the rotation of the members of the close binary (which is the main novelty of this work).

In the next section the equations of motions are presented, and in Sect. 3 I give a short illustration of the first results.

2. Equations of motions

In formulating the equation of motions for the close pair I mainly followed the treatment of Kopal (1978). The stars were considered as liquid, viscous bodies. The initial orientation of the axis of rotation of each component can be arbitrary. The angular velocity of the rotation can differ from the Keplerian angular velocity. Only the first order terms were treated. For the more distant third companion only a mass-point model was applied. This means the effect of the third body was calculated only as a point mass-point mass interaction.

2.1. Equations of the orbital motion

The equations of orbital motion of the three body calculated in the usual Jacobian coordinates have the following form:

$$\ddot{\boldsymbol{\rho}}_2 = \frac{M_{12}}{m_1 m_2} \frac{\partial (U + W_{12})}{\partial \boldsymbol{\rho}_2} + \sum_{i=1}^{2} \boldsymbol{f}_{t_i}, \tag{1}$$

$$\ddot{\boldsymbol{\rho}}_3 = \frac{M_{123}}{M_{12} m_3} \frac{\partial U}{\partial \boldsymbol{\rho}_3}, \tag{2}$$

where M_{12} the total mass of the close binary, while M_{123} is the same for the triple system. Furthermore, U is the mass-point part of the three-body potential,

$$W_{12} = \frac{G m_1 m_2}{\rho_2} \left[\sum_{i=1}^{2} \left(\sum_{j=2}^{4} \frac{m_{3-i}}{m_i} k_j^{(i)} \left(\frac{R_i}{\rho_2} \right)^{2j+1} - \frac{\omega_{z'i}^2}{3 G m_i} k_2^{(i)} \frac{R_i^5}{\rho_2^2} P_2(\nu_{1i}^{"}) \right) \right] \tag{3}$$

contains the equilibrium tide and the rotational part of the potential function, where ν_{1i} denotes the directional cosine between the radius-vector and the axis of rotation of the ith component, R_i stands for the radius of the i-th star, while the other letters have their usual meaning. Finally, the last term in Eq. (1) stands for the extra force arising from the dissipation of the tides (see later). The Eq. (1) are coupled with the (Eulerian) equation of the stellar rotation through the centrifugal and the dissipative terms.

2.2. The equations of the stellar rotation

The well-known Eulerian equations of a deformable, dissipative body in vectorial form the following (Tokis, 1974).

$$\begin{aligned} &\boldsymbol{I}\dot{\boldsymbol{\omega}} + \boldsymbol{\omega} \wedge \boldsymbol{I}\boldsymbol{\omega} + \dot{\boldsymbol{I}}\boldsymbol{\omega} - \\ -\boldsymbol{\omega} \wedge \int \boldsymbol{r} \wedge \dot{\boldsymbol{r}}_0' \mathrm{d}m + \int \boldsymbol{r} \wedge \ddot{\boldsymbol{r}}_0' \mathrm{d}m &= \int \boldsymbol{r} \wedge \nabla U \mathrm{d}m + \int \boldsymbol{r} \wedge \nabla \mathcal{D} \mathrm{d}V, \quad (4) \end{aligned}$$

where the different terms have the following meaning:

$\boldsymbol{I}$ – is the inertia tensor of the current star ,

$\dot{\boldsymbol{I}}\boldsymbol{\omega} - \boldsymbol{\omega} \wedge \int \boldsymbol{r} \wedge \dot{\boldsymbol{r}}_0' \mathrm{d}m$ – is the gyroscopic term (which hide the Coriolis acceleration $2\boldsymbol{\omega} \wedge \dot{\boldsymbol{r}}_0'$).

$\int \boldsymbol{r} \wedge \ddot{\boldsymbol{r}}_0' \mathrm{d}m$ – arising from acceleration of deformation $\ddot{\boldsymbol{r}}_0'$,

$\int \boldsymbol{r} \wedge \nabla U \mathrm{d}m$ – arising from the centrifugal potential, and

$\int \boldsymbol{r} \wedge \nabla \mathcal{D} \mathrm{d}V$ – containing the dissipative term.

The primed velocity and acceleration vectors refer to the velocity and acceleration of the mass element of the star with respect to a coordinate system co-rotates with the body, but expressed in the fixed system.

The calculation of the explicit form of the following terms can be found in Kopal (1978). Here I present only the result which is the following (for one of the stars):

$$\begin{aligned} &m_1 h_1^2 \dot{\boldsymbol{\omega}} + \alpha \left\{ K_2 \left[\frac{2\boldsymbol{\rho}_2(\boldsymbol{\omega} \wedge \boldsymbol{\omega}^*) - \boldsymbol{\rho}_2(7\dot{\boldsymbol{\omega}} + \dot{\boldsymbol{\omega}}^*)}{\rho_2^2} \boldsymbol{\rho}_2 + \frac{8\boldsymbol{\rho}_2 \boldsymbol{\omega}}{\rho_2^2} \boldsymbol{\rho}_2 \wedge \boldsymbol{\omega} - \right.\right. \\ &\quad - \frac{\boldsymbol{p}\boldsymbol{\rho}_2}{\rho_2^2} \boldsymbol{\rho}_2 \wedge \boldsymbol{p} - \frac{8\omega_{z'}\boldsymbol{\rho}_2}{\rho_2^2} \boldsymbol{\rho}_2 \wedge \boldsymbol{\omega}_{z'} + \frac{1}{3}(7\dot{\boldsymbol{\omega}} + \dot{\boldsymbol{\omega}}^* + 2\boldsymbol{\omega} \wedge \boldsymbol{\omega}^*) \left.\right] + \\ &+ 2H_2 \left(\frac{1}{3}\boldsymbol{\omega}^* - \frac{\boldsymbol{\omega}^* \boldsymbol{\rho}_2}{\rho_2^2} \boldsymbol{\rho}_2 \right) + 8 \frac{\omega_{z'}^2}{3Gm_1} \left[\frac{\omega_{z'}\dot{\boldsymbol{\omega}}}{\omega_{z'}^2} \boldsymbol{\omega}_{z'} + \frac{\omega_{z'}\boldsymbol{\omega}}{\omega_{z'}^2} \boldsymbol{\omega} \wedge \boldsymbol{\omega}_{z'} - \frac{1}{3}\dot{\boldsymbol{\omega}} \right] \left.\right\} - \\ &\quad - \frac{4}{5}\pi \frac{K_2}{\rho_2^2} \mu_1 R_1^6 \left(3\boldsymbol{\rho}_2 \wedge (\boldsymbol{\rho}_2 \wedge \boldsymbol{p}) + 2\rho_2^2 \boldsymbol{p} \right) = 0, \quad (5) \end{aligned}$$

where m_1 is the mass, h_1 is the gyration radius of the star, ω is the angular velocity vector of the star (depends only on time), $\omega_{z'}$ the angular velocity vector of the star's rotation around its rotational axis (denoted as z'). Furthermore, K_2 is the amplitude of the lowest harmonic of the tidal distortion arised by the companion's gravity as follows:

$$K_2 = (1 + k_2)\frac{m_2}{m_1}\frac{1}{\rho_2^3}, \tag{6}$$

while H_2 is its time derivative as well as:

$$H_2 = -3K_2\frac{\dot{\rho}_2}{\rho_2}, \tag{7}$$

and

$$\alpha = \int_\tau \rho r^7 \mathrm{d}r \approx \frac{1}{4}k_2 m_1 R_1^5. \tag{8}$$

Finally, the angular velocity vector ω^* occurs in the transformation from a fixed coordinate system to another frame of references, the x'' direction of which is always parallel to the radius vector of the two stars [e.g. $\boldsymbol{\rho}_2 \equiv \rho_2(1;0;0)$], while the auxiliary vector $\boldsymbol{p}$ denotes the $\omega - \omega^*$ difference.

The last term in Eq. (5) stands for the dissipation caused by the tides. This was calculated directly from the divergence of the viscous stress tensor. In the scheme of our approximation it doesn't give any direct contribution to the Eq. (1) of the orbital motion, e.g. $\boldsymbol{f}_{t_i} \equiv \boldsymbol{0}$, (which picture dramatically would change if we allowed for the interaction between the rotational and tidal distortion). Nevertheless, this term has indirect effect on the orbital motion, changing the speed of the rotation of the star as well as the direction its rotational axis. (Both of them occur in the centrifugal term of the Eq. 3 potential.)

3. Illustration of the results

I integrated the Algol system in three ways with the same parameters which Harrington (1984) used. First a mass–point approximation was used. The evolution of the orbital elements is shown in Fig. 1a. The presence of the Kozai resonance (Kozai, 1962) is evident. This makes the system unstable.

As a second step different politropic models were used for the stars of the eclipsing system, with synchronous rotation. In that cases the picture changed dramatically. The system became clearly stable (cf. Söderhjelm 1984, Kiseleva et al. 1998) in the sense of Kozai resonance. The eccentricity of the close

orbit shows only lower amplitude fluctuations on at least two different time scales (from decades to centuries). Nevertheless, the visible inclination (and the longitude of the node) of the binary vary in two different ways. The large amplitude variation is due to the rotation of the orbital plane of the binary caused by the distant third body which would yield easily observable effects on a time scale of a century (eg. the change of the eclipse depth in eclipsing binaries, and a virtual period change). (See Fig. 1b.) There is also a few tenths degree of fluctuation (which cannot be seen in the figure) produced by the precession of the stars, which illustrates the interaction between the spin and the orbital angular momentum.

Finally I 'inclined' the rotational axis of the secondary star, and 'made' the primary to rotate two times faster than its average Keplerian angular velocity (see Fig. 1c, 2.). In that case the behaviour of the stars became completely 'crazy', a phenomenon which is the subject of my future work.

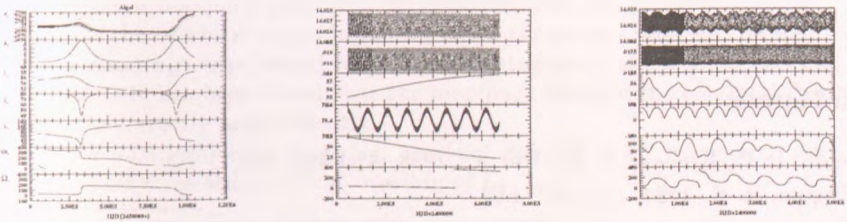

Figure 1: The variation of the osculating orbital elements of the Algol system, in the mass–point (a), the dissipative synchronous politropic (b), and the non-dissipative inclined, fast-rotating politropic model (c). The elements from top to bottom: (a): e_1, e_0, i_1, i_{mutual}, i_0, ω_0, Ω_0; (b) and (c): a_0, e_0, i_1, i_m, i_0, Ω_0.

This work is in its first stage yet. In the following I plan several runs with different initial conditions in the geometrical and physical parameters. The studies will concentrate on the following three main topics: (a) Short term observable effects produced by the interaction between rotation and tides, as well as the presence of the third body, (b) the effectiveness of the dissipation in the synchronization of such systems, finally, (c) the formation, and stability of triple stellar systems.

Acknowledgements

This work was supported by the OTKA F030147 National Grant.

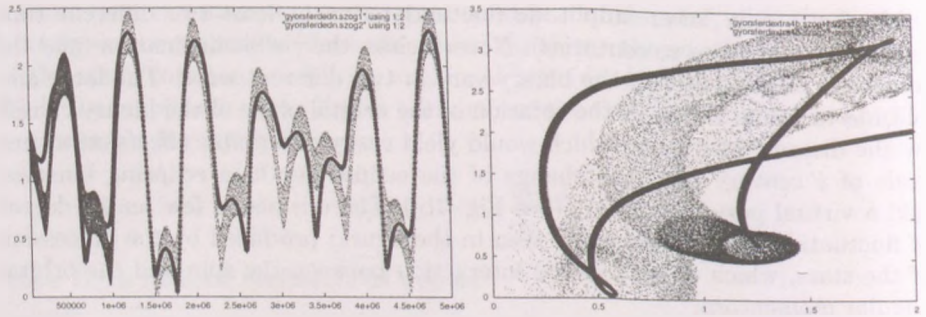

Figure 2: The evolution of the Eulerian angles of rotation of the stars during the inclined fast rotator run (see Fig. 1c). (*a*): The time evolution of θ. (The time is given in days). (*b*): Precession and nutation in the first one million days of the current run on the $\theta - \phi$ plane. (The thick, black line refers to the primary star.)

References

Eggleton, P. P., Kiseleva, L. G., Hut, P., 1998, ApJ 499, 853

Harrington, R. S., 1984, ApJ 277, L69

Kiseleva, L. G., Eggleton, P. P., Mikkola, S., 1998, MNRAS 300, 292

Kopal, Z. , 1978, *Dynamics of Close Binary Systems*, D. Reidel, Dordrecht

Kozai, Y., 1962, AJ 67, 591

Söderhjelm, S., 1984, A&A 141, 232

Tokis, J. N. , 1974, Ap&SS 26, 447

MAPPING REPRESENTATIONS OF THE COORBITAL DYNAMICS

Zsolt Sándor
Deptartment of Astronomy, Eötvös Loránd University
H-1518 Budapest, P.O.Box 32., Hungary
E-mail: szsolt@astro.elte.hu

Abstract

Symplectic mappings have been developed to study the phase space structure of the coorbital region in the restricted three-body problem (RTBP). The mappings were tested by numerical integration of the equations of motion. It has been found that the mappings describe the coorbital dynamics correctly and efficiently.

KEYWORDS: *symplectic mapping, coorbital dynamics, 1:1 resonance, the restricted three-body problem, stability of L_4*

1. Introduction

A motion is said to be *coorbital* when two bodies are revolving in nearly identical orbits around a central massive body. In the Solar System there are several objects satisfying the above criterion; the *Trojan* asteroids share their orbits with Jupiter, there are Trojan-like objects in the Saturnian satellite system, and recently, coorbital companions of Mars and Earth have been found.

In this work we summarize our results in constructing an analytic symplectic mapping for the coorbital dynamics in the RTBP Sándor and Morais (2000), Sándor (2000), and we present a semi-numerical technique, which allows to study the coorbital dynamics at large eccentricities of the coorbiting objects.

Our mappings have been constructed by using the method suggested by Hadjidemetriou (1991). Although this mapping technique has been applied widely for several cases of different mean motion resonances, no applications has been done yet for the 1:1 resonance, which is the main feature of the coorbital dynamics. On the other hand, the 1:1 resonance is an outstanding problem, (see Érdi (1997) for a recent review), and it deserves continuous attention.

2. Analytic mapping for the coorbital dynamics

As the generating function of our mapping we used the averaged Hamiltonian, where the perturbing function was expanded up to $O(e^2)$ and the short period terms were averaged out.

The Hamiltonian of the RTBP is (Brown and Shook , 1933):

$$H = 1/[2(x+1)^2] + x + 1 + \mu a' R(x, x_2, \tau, \omega)/r', \tag{1}$$

where R is the perturbing function, μ is the mass parameter, $x = (a/a')^{1/2} - 1$, $x_2 = (x+1)(\sqrt{1-e^2} - 1)$ are action like variables, $\tau = \lambda - \lambda'$ (mean synodic longitude), and ω (argument of the perihelion) are angle variables.

If we keep only the long-period terms and expand R up to $O(e^2)$, then

$$\begin{aligned} H(x, \tau, x_2) = \; & 1/[2(x+1)^2] + x + 1 + \mu R_0(\tau) + \\ & + \mu e^2 R_1(\tau) + \mu e^2 \alpha^2 R_2(\tau)/4 \; , \end{aligned} \tag{2}$$

where $\alpha = a'/a$, $R_0 = 1/[(2 - 2\cos\tau)^{1/2}] - \cos\tau - 1/2$, $R_1 = \partial^2 R_0/\partial\tau^2$, and $R_2 = \partial^2 R_0/\partial\alpha^2$. Moreover, noticing that $e^2 = 1 - [x_2/(x+1) + 1]^2$ and $\alpha = (x+1)^{-2}$, we can write the coefficients of R_1 and R_2 as $f_1(x, x_2) = e^2$ and $f_2(x, x_2) = e^2\alpha^2/4$, respectively. The generating function of the mapping is then:

$$\begin{aligned} W = \; & x_{n+1}\tau_n + T/[2(x_{n+1}+1)^2] + T(x_{n+1}+1) + \mu T R_0(\tau_n) + \\ & + \mu T f_1(x_{n+1}, x_2) R_1(\tau_n) + \mu T f_2(x_{n+1}, x_2) R_2(\tau_n) \; , \end{aligned} \tag{3}$$

where $T = 2\pi$ is the period of the resonant periodic orbit, and x_2 is the parameter of the mapping.

The mapping is obtained via eqs. $x_n = \partial W/\partial\tau_n, \tau_{n+1} = \partial W/\partial x_{n+1}$:

$$\begin{aligned} x_{n+1} &= x_n - \mu T R_0'(\tau_n) - \mu T f_1(x_{n+1}, x_2) R_1'(\tau_n) \\ &\quad - \mu T f_2(x_{n+1}, x_2) R_2'(\tau_n) \\ \tau_{n+1} &= \tau_n - T[(x_{n+1}+1)^{-3} - 1] + \mu T f_1'(x_{n+1}, x_2) R_1(\tau_n) \\ &\quad + \mu T f_2'(x_{n+1}, x_2) R_2(\tau_n), \end{aligned} \tag{4}$$

where $R_i'(\tau_n) = dR_i/d\tau_n$, and $f_i'(x_{n+1}, x_2) = \partial f_i/\partial x_{n+1}$. The first equation of the mapping is implicit (in x_{n+1}), therefore a numerical procedure should be applied to solve it.

It can be proved, that the 1-period fixed points of the mapping correspond to the stationary points of the averaged system (Sándor , 2000). The stationary

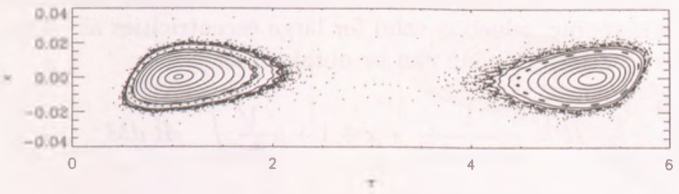

Figure 1: The phase space structure obtained by the mapping (4).

points of the averaged system correspond to the periodic orbits in the original (non-averaged) system. Thus the 1-period fixed points of the mapping correspond to the periodic solutions of the original system.

It is also true, that the stability indices of the fixed points of the mapping and the corresponding periodic orbits are the same. (The stability indices of the Lagrangian points in the mapping and the corresponding periodic orbits in the original system are: $Tr(L_3) = 2 + 21\mu\pi^2/2 > 2$ and $Tr(L_4) = Tr(L_5) = 2 - 27\mu\pi^2 < 2$.)

These two conditions, mentioned above, are necessary to obtain a mapping which describes the original system not only qualitatively, but quantitatively as well, see the details in (Hadjidemetriou , 1991).

The phase space structure of our mapping represents well the features of the original system. The fixed points can be identified as the Lagrangian points $L_{4,5}$ and L_3, and their stability reflects the stability of the corresponding equilibrium solutions ($L_{4,5}$ are stable, L_3 is unstable). Around the stable Lagrangian points there are invariant curves corresponding to the quasi-periodic librations in the original system. If μ is small there are horseshoe orbits encircling L_4, L_3, and L_5, and tadpole orbits around L_4 and L_5. If μ is larger, there are only stable tadpole orbits. The phase space structure for $\mu = 0.001$ (Sun-Jupiter case) and $x_2 = -0.002$, obtained by the mapping, is shown in Figure 1.

3. The semi-mumerical mapping

It was shown recently by Namouni (1999) and by Namouni and Murray (2000), that the presence of large eccentricity and inclination in the coorbital problem can result in a rich dynamical behaviour. Since the analytic mapping (4) was generated by a second order generating function, it is valid only for small eccen-

tricities. Therefore, we averaged the perturbing function numerically, and we developed a mapping, which is valid for large eccentricities as well.

The averaged Hamiltonian can be obtained as:

$$\bar{H} = \frac{1}{2(x+1)^2} + x + 1 + \mu \frac{1}{2\pi} \int_0^{2\pi} R \, dM \, . \tag{5}$$

The perturbing funcion for the circular case is:

$$R = \frac{1}{\Delta} - \frac{1}{r} - r\cos\phi + \frac{1}{2} \, , \tag{6}$$

where ϕ is the angle between the radii directing from the Sun to Jupiter and the test particle.

Since $\Delta^2 = r^2 - 2r\cos\phi + 1$, $r = a(1 - e\cos E)$, and $\phi = \tau + v - M$, where $a = (x+1)^{-2}$, $e^2 = 1 - [x_2/(x+1)+1]^2$ and the difference between the true and mean anomaly can be expressed as: $v - M = 2\arctan[\sqrt{(1+e)/(1-e)}\tan(E/2)] - E + e\sin E$, it is convenient to use the eccentric anomaly E instead of the mean anomaly M. Using the Keplerian equation, the integral in (5) can be written as:

$$\frac{1}{2\pi} \int_0^{2\pi} R \, dM = \frac{1}{2\pi} \int_0^{2\pi} R(1 - e\cos E) \, dE =: < R(x, x_2, \tau) > \, . \tag{7}$$

During the averaging process only E is varied, the other variables in R are kept fixed. We note that this averaging technique was first used by Schubart (1964).

The generating function of the semi-numerical mapping is:

$$W = x_{n+1}\tau_n + 2\pi H_0(x_{n+1}) + 2\pi\mu < R(x_{n+1}, x_2, \tau_n) > \, , \tag{8}$$

and the corresponding mapping:

$$\begin{aligned} x_{n+1} &= x_x - 2\pi\mu \frac{\partial}{\partial \tau_n} < R(x_{n+1}, x_2, \tau_n) > \, , \\ \tau_{n+1} &= \tau_n + 2\pi \frac{\partial}{\partial x_{n+1}} H_0(x_{n+1}) + 2\pi\mu \frac{\partial}{\partial x_{n+1}} < R(x_{n+1}, x_2, \tau_n) > \, . \end{aligned} \tag{9}$$

The first equation of (9) is an implicit integral equation for x_{n+1}. When we evaluate numericaly the derivatives of $< R(x_{n+1}, x_2, \tau_n) >$ with respect to τ_n and x_{n+1} we use the approximation:

$$\frac{\partial}{\partial *} < R(x_{n+1}, x_2, \tau_n) > \approx \frac{1}{N} \sum_{j=1}^{N} \frac{\partial}{\partial *} [R(x_{n+1}, x_2, \tau_n, E_j)(1 - e\cos E_j)] \, , \tag{10}$$

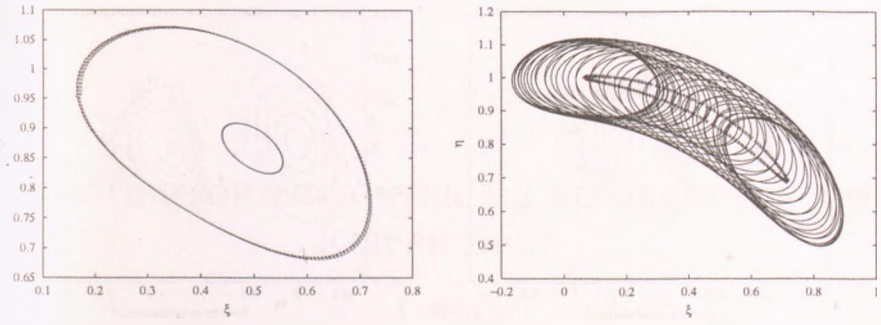

Figure 2: On the left (a): Two periodic orbits corresponding to the fixed points of the mapping. For the inner orbit $e = 0.03$ for the outer one $e = 0.15$. On the right (b): A quasi-periodic orbit for $e = 0.11$ and its *guiding center* obtained by the mapping (9).

where in both cases $E_j = 2j\pi/N$, $j = 1, ..., N$, and the $*$ represents τ_n or x_{n+1}.

Solving the first equation of (9) for x_{n+1} we used the approximation (10). If x_{n+1} is calculated one should substitute it into the second equation of the mapping, and τ_{n+1} can be calculated by using (10) as well.

4. Validity of the semi-numerical mapping

We tested the semi-numerical mapping by numerical integrations of the equations of motion of the RTBP.

From the fixed points of the mapping we calculated the initial conditions for the periodic orbits. We have found, that there is a good coincidence at small eccentricities, however, in the case of larger eccentricites the corresponding orbits in the original system were not exactly the periodic orbits. Some of the resulting periodic and "nearly" periodic orbits are shown in Figure 2a. The variables of the mapping (x_i, τ_i) can be transformed to the usual synodic Cartesian system (ξ, η) of the RTBP using the equations $\xi = a\cos\tau$ and $\eta = a\sin\tau$. Thus calculating the initial conditions for the equations of motion from x, τ, and x_2, one can compare the orbits obtained by the mapping and by the numerical integration (Figure 2b). Studying Figure 2b one can conclude that an orbit obtained by the mapping is the *guiding center's approximation* of the original orbit.

Finally, Figure 3 shows the phase space structure for large eccentricities of the test particle. One can observe, that the region filled by *retrograde satellite orbits* around Jupiter increases with e.

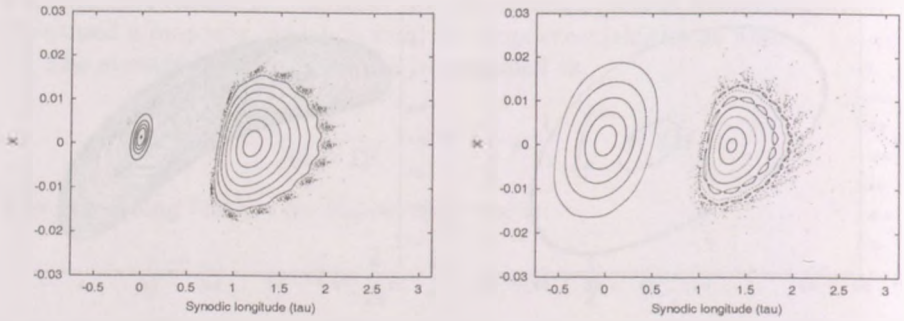

Figure 3: The phase space structure for large eccentricities; on the left figure $e = 0.27$, on the right figure $e = 0.39$.

Acknowledgments

I would like to thank the helpfull discussions with Prof. B. Érdi, Prof. R. Dvorak, Dr. H. Morais, and Dr. K. Wodnar. This work was supported by the Hungarian NRF under the grant OTKA F030147.

References

Brown, E. W. and Shook, C. A.: 1933, *Planetary Theory*, Cambridge University Press, Cambridge

Érdi, B.: 1997, *Cel. Mech. and Dyn. Astron.* **65**, 149.

Hadjidemetriou, J. D.: 1991, in A. E. Roy (ed) *Predictability, Stability and Chaos in N-body Dynamical Systems*, Plenum Press, New York, pp. 157-175

Namouni, F.: 1999, *Icarus* **137**, 293.

Namouni, F. and Murray, C. D.: 2000, *Cel. Mech. and Dyn. Astron.* **76**, 131.

Sándor, Zs. and Morais, M. H.: 2000, in *Proceedings of the US-European Celestial Mechanics Workshop* (to be appear)

Sándor, Zs.: 2000, in F. Freistetter, R. Dvorak, and B. Érdi (eds.) *Proceedings of the 2nd Austro-Hungarian Workshop on Trojans and Related Topics*, Eötvös University, Budapest and University of Vienna (in press)

Schubart, J.: 1964, *SAO Research in Space Science Special Report* **149**, Cambridge, Massachusetts

Structure of the outer 1:2 resonance in the Kuiper Belt

Á. Süli
Eötvös Loránd University, Department of Astronomy
H-1518 Budapest, P.O.Box 32., Hungary

Abstract

The stability of orbits near the 1:2 resonance with Neptune in the planar restricted three-body problem is investigated by computing their stochasticity using the Lyapunov Characteristic Exponents (LCE) and the Fast Lyapunov Indicators (FLI).

1. Introduction

The trans-Neptunian region of the Solar System has become the focus of considerable interest, mainly due to the detection of hundreds of 100 km sized bodies beyond Neptune's orbit (see http://galileo.ifa.hawaii.edu/users/jewitt/kb.html). This reservoir, known as the Edgeworth-Kuiper-Belt is one of the major discoveries of Solar System science in recent years (Luu and Jewitt , 1993). The existence of the Kuiper-belt objects (hereafter KBO) was originally postulated from considerations of mass distribution in the early Solar System (Kuiper , 1951). Observations of extended discs around main-sequence stars and the need for a source of short period comets have also supported this theory.

Duncan et al. (1995) performed integrations of thousands of test particles for up to 4 Gyrs in order to complete a dynamical survey of the trans-Neptunian region. Their main results can be seen in Fig.3 and include the following features:

1. For test particles with low eccentricity there is a relatively stable band between 36 and 40 AU and almost complete stability beyond 42 AU. The lack of observed KBOs between 36 and 40 AU is possibly due to the formation process of the Solar System and due to the early dynamical

evolution of the outer planets. The observed KBOs beyond 42 AU form the *classical group of KBOs.*

2. For higher eccentricities the region interior to 42 AU is largely unstable except for stable bands near mean motion resonances with Neptune, such as the 2:3 near 39.5 AU within which lies Pluto. The KBOs in the 2:3 resonance are the *Plutinos* (little Plutos). This name marks the dynamical similarity with Pluto.

So far there are four observed objects which possess large, eccentric, inclined orbits that have perihelion distances near 35 AU. These observations make it clear that these objects, the so called *scattered Kuiper-belt objects* are a distinct dynamical population in the Kuiper-belt, separate from the classical and resonant objects.

2. Numerical experiments in the framework of the planar RTB

In order to develop a basic understanding of the behaviour of objects in the 1:2 resonance with Neptune it is necesssary to cover as wide range in the orbital elements space as possible while integrating the equations of motion as long as possible. The ability to integrate the orbits of objects in the complete Solar System in the 1:2 resonance for the age of the Solar System is still beyond the reach of modern computers. Thus, in a first attempt we choose the simplest model, the well known planar restricted problem of three bodies.

2.1. Equations of motion

In this problem two point masses (the primaries) orbit one another in circular Keplerian orbit, each attracting, but not influenced by a third body of infinitesimal mass. The problem is to determine the motion of this third body. We used the following equations of motion of the problem, which are valid in a coordinate system rotating uniformly together with the primaries and having its center at one of the primaries (in our model at the more massive one).

$$\begin{aligned} \dot{x}_1 &= x_3, \\ \dot{x}_2 &= x_4, \end{aligned} \tag{1}$$

$$\begin{aligned} \dot{x}_3 &= 2x_4 + \frac{\partial \Omega}{\partial x_1}, \\ \dot{x}_4 &= -2x_3 + \frac{\partial \Omega}{\partial x_2}, \end{aligned}$$

where

$$\begin{aligned} \Omega &= (1-\mu)\left(\frac{1}{r_1} + \frac{r_1^2}{2}\right) + \mu\left(\frac{1}{r_2} + \frac{r_2^2}{2}\right), \\ r_1^2 &= x_1^2 + x_2^2, \\ r_2^2 &= (x_1 - 1)^2 + x_2^2. \end{aligned}$$

In Equations (1) the dot ($\dot{}$) denotes differentiation with respect to the time, x_1 and x_2 are the rectangular coordinates of the third body, and μ is the mass parameter. The units are the usual: the unit distance is the distance of the primaries, the unit mass is the total mass of the primaries and the rotation period of the primaries is 2π time units. In these units the gravitational constant is 1 ($k = 1$).

In those cases when the distance between the third body and one of the primaries becomes small it is necessary to regularize the equations of motion. In our investigations the Levi-Civita regularization was used whenever the massless particle entered Neptune's Hill sphere.

2.2. Initial conditions

Our intent was to achive reasonably high resolution in the semimajor axis and in the eccentricity, therefore we used the following initial conditions:

$$\begin{aligned} a_0 &= 47.0 + i \cdot \Delta a, \quad \Delta a = 0.02\ AU, \quad i = 0 \ldots 100 \\ e_0 &= 0.0 + j \cdot \Delta e, \quad \Delta e = 0.025, \quad j = 0 \ldots 12 \end{aligned}$$

The initial longitude of perihelion and the mean anomaly of each test particle were set to zero. This set of orbital elements corresponds to the most unstable outer resonant configuration because when a test particle is at its perihelion than Neptune and the test particle are in conjuction. Using these initial conditions we integrated the eauations of motion for 10.000 time units, which corresponds approximetly to 250.000 years.

The numerical integrations were carried out by means of the Bulirsh-Stoer integration method. For the calculation of the Lyapunov Characteristic Exponents - which are defined as the local variations of the tangent vectors to the flow

(Benettin et al. , 1976) - the program employs the Gram-Schmidt procedure to replace evolved tangent vectors by new orthonormalized ones.

3. Stability of test particles in the 1:2 resonance

The main results can be seen in Fig.1 and Fig.2. Figure 1 was obtained by calculating the test particle's LCE whereas Figure 2 was obtained by calculating the FLI. As expected the two figures show almost the same dynamical structure. In both figures the 1:2 resonance can be clearly seen, and the usual U form of the resonance is also visible.

Note that the boundary between regular and chaotic domains on the LCE map are not so sharp as on the FLI map, indicating that the method of the FLI is more sensitive to chaotic motion.

A comparison of Fig.1. with Fig.2. shows a fine agreement regarding the question of stability. In Fig.1 and Fig.2 there is complete stability for nearly circular orbits except for some unstable bands near the resonance. These bands are clearly visible in Fig.2 and also in Fig.3. These features are poorly detectable in Fig.1.

It is a striking feature that the most stable particles have initial semimajor axis approximately 47.73 AU (center of the 1:2 resonance) and eccentricity as high as 0.25, 0.275 and 0.3. These properties are also visible in Fig.3.

For higher eccentricities the region between 47 and 49 AU is largely unstable except for stable bands near the 1:2 resonance.

The results of computations of the planar restricted three-body problem indicate, that fictitious KBOs are moving in stable orbits near the 1:2 resonance if their eccentricities are lower than 0.25. In deep resonance objects with eccentricity as high as 0.275 and 0.3 are stable.

4. Conclusions

We can conclude that fictitious KBOs in the 1:2 resonance are stable, and the vicinity of this resonance is stable too. This has been confirmed by using two different methods, the method of LCE and FLI. It is reassuring that using the simplest model of the planar RTBP provided results which are in fine agreement with former results obtained by integrating a more realistic model. This implies that Fig.1 and Fig.2 are reliable and of course much more detailed than Fig. 4.

As a continuation of this work we intend to integrate the spatial elliptic restricted three-body problem for longer time span to obtain a more reliable

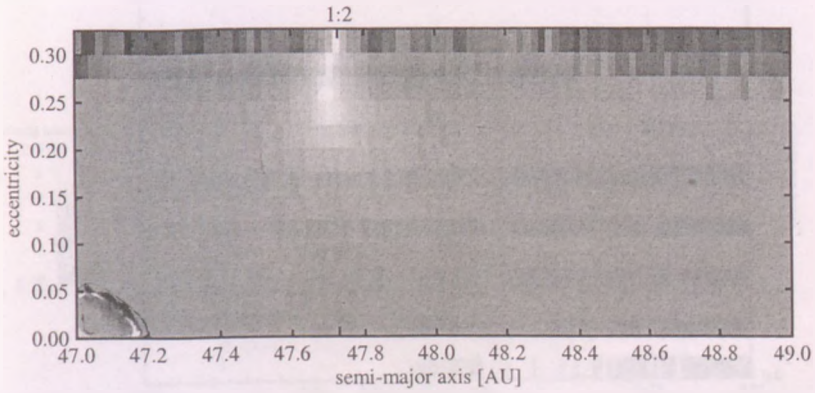

Figure 1: Dynamical stability map for test particles in a range of semimajor axis and eccentricity. Each particle is represented by a narrow vertical strip of colour, whose lower left corner is at the particle's initial a and e. The colour of each strip represents the dynamical lifetime of the particle. Strips that are coloured white represent objects that survive for the length of the integration. Dark regions are particulary unstable. The colours were obtained by fitting lines to the $log(t) - log(LCE)$ curves by using the least squares method.

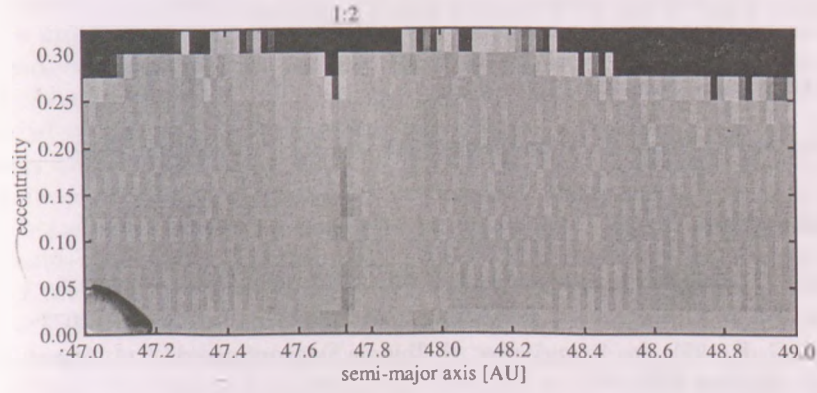

Figure 2: See explanation below Fig.1. This figure is based on the FLI values of the massless particles.

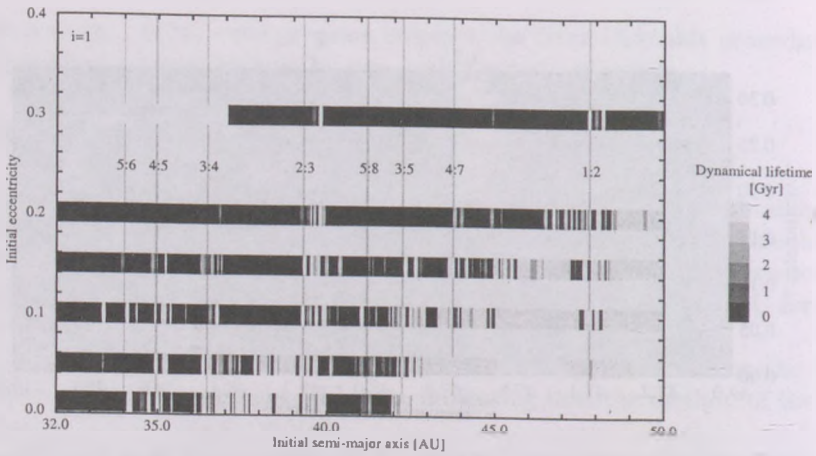

Figure 3: Dynamical lifetime before first close encounter with Neptune for test particles in a range of semi-major axes and eccentricities, with initial inclination 1^0 (Duncan et al. , 1995) Each particle is represented by a narrow vertical strip, centered at the particle's initial eccentricity and semi-major axis. The lightest coloured strips represents particles that survived the length of the integration (4 billion years). Dark regions are particulary unstable. The locations of low order mean motion resonances with Neptune are also shown.

"stability map" of the 1:2 resonance and it's vicinity.

Acknowledgments

I would like to thank the helpfull discussions with Prof. Bálint Érdi.

References

Benettin, G., Galgani, L., and Strelcyn, J. M.: 1976, *Phys. Rev.* **A14**, 2338

Duncan, M. J., Levison, H. F., and Budd, S. M. (1995) *Astron. J.* **110**, 3073

Kuiper, G. P. 1951. *In Astrophysics: A Topical Symposium,* ed. J. A. Hynek, (New York: McGraw Hill), 357

Luu, J. and Jewitt, D. (1993) *Nature* **362**, 730

Photometric Redshifts

Tamás Budavári
Eötvös Loránd University, Department of Physics of Complex Systems
H-1117 Budapest, Pázmány P. sétány 1/A, Hungary
E-mail: budavari@complex.elte.hu

Abstract

We review the basic techniques of photometric redshifts and propose a hybrid method of empirical and template fitting to combine their advantages without any of their drawbacks. We deduce spectral templates from photometry and redshifts by improving on the agreement of measured and synthetic colors. The resulting templates give better redshift estimates.
KEYWORDS: *galaxies: photometry — galaxies: distances and redshifts*

1. Introduction

The Universe is expanding. Observed photons of objects moving with the Hubble flow appear to be redder than emitted. This red-shift is typically measured by identifying spectral features (e.g. H&K break, Ly-α, etc.) in the observed, high resolution spectrum. One can compare the location of these lines to those measured in laboratories and obtain the redshift z with high accuracy. Spectroscopy takes a tremendous amount of time for faint objects (if possible) and also quite often only one spectral feature is found, which makes it hard to identify. Photometry is faster and goes deeper, since collecting photons in $\sim$2000Å wide bands gives better signal-to-noise ratio for thousands of objects at the same time. Estimating z based on photometric data is a great opportunity and has been already utilized in statistical studies of galaxy properties. SubbaRao et al. (1996) measured the luminosity function by treating all galaxies as probability distributions in absolute magnitude and Connolly et al. (1997) derived the star formation rate in the Hubble Deep Field (HDF) for a redshift range currently reachable only via photometric redshifts. The photometric redshifts are also ideally suited for studying clustering evolution, gravitational lensing, etc. and frequently used in spectroscopic target selection.

1.1. Historical overview

The concept of photometric redshift is not new. Baum (1962) used photometric data first to measure redshifts. With 9 filters he observed elliptical galaxies in clusters and compared the average of their "rough spectrum" to each other. Having known the distance of the Virgo cluster he could estimate the redshift of a few others. His technique was reasonably accurate but strongly dependent on the 4000Å break and only worked for elliptical galaxies.

Koo (1985) looked at the problem from a different point of view. He used synthetic spectra (Bruzual, 1983) to trace iso-redshift lines in color-shape diagrams (e.g. $U-J$ vs. $-U+J+F-N$). Comparing the color-shape plots of measured $UJFN$ magnitudes to the simulated iso-z tracks he could estimate redshifts for a hundred faint galaxies.

Loh & Spillar (1986) used a similar approach as Baum. They observed 34 galaxies of known redshifts in 6 custom bands and used them as templates for another thousand objects.

Connolly et al. (1995a) assumed the redshift to be a simple analytic function of the magnitudes (or colors). The technique they developed required a training set of large number of galaxies at known distances. A linear or quadratic fitting function was derived which could be very quickly evaluated at other parameters.

Steidel et al. (1996) looked for ultra-violet "dropouts" in a custom U_n filter. They could detect if the Lyman limit (at restframe 912Å) passed through the band with redshift and set a lower limit, $z \geq 2$.

2. Review and development

Photometric redshift techniques can be categorized into two basic classes. One class of methods use a training set of galaxies with known photometry and spectroscopic redshift to derive an empirical relation between colors and redshift (Connolly et al., 1995a; Wang Bahcall & Turner, 1998). After calibration, the method can predict z for objects with only photometry. Both advantages and disadvantages lie in its empirical nature. Effects of dust and evolution are also present in the training set (+), but the estimator can predict redshift only for objects similar to those in the training set (–) and one needs a training set for every survey (–).

The other class of techniques, the template based redshift estimators use spectral energy distributions (SEDs) (Koo, 1985; Connolly et al., 1995b; Gwyn & Hartwick, 1996; Fernández-Soto et al., 1999; Benítez, 2000; Csabai et al., 2000; Budavári et al., 2000). One can find a best matching spectral type and

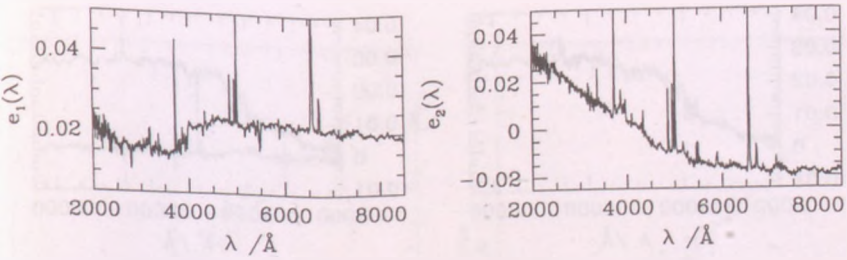

Figure 1: Galaxy spectra can be approximated with a linear combination of the above 2 orthogonal templates at the 99% level. See figure 2 for an example.

redshift by minimizing the difference between the measured and synthetic spectra. Apparently this method has more physical outcome (+). Our expertise is encoded in the templates, so this method works for any survey without calibration (+), but templates are used as they come and usually do not fulfill our expectations (−).

2.1. Orthogonal approach

Using principal component analysis (PCA) Connolly et al. (1995b) have shown that empirical SEDs could be accuratelly approximated with linear combinations of 2 or 3 orthogonal functions, the eigentemplates. Figure 1 shows the first two eigencomponents for the Kinney et al. (1996) spectra. If every SED in the original template library is described by two coefficients (see figure 2), photometric redshifts can be worked out by varying these coefficients besides the redshift. This formalism provides a continuum number of SEDs as opposed to traditional template fitting, where we have a finite number of discrete templates. Another improvement is that one can propagate errors properly starting with photometric uncertainties.

The Hubble Deep Field (Williams et al., 1996) has been a testbed for photometric redshift applications. Figure 3 shows the results of the HDF-N/NICMOS photometric catalog (Dickinson et al., 2000) as computed by the above method using Coleman, Wu & Weedman (1980) based eigenspectra (hereafter CWW).

When projecting the CWW SEDs onto the subspace spanned by 3 orthogonal eigentemplates we find that they lie on a one dimensional locus and in fact most of the estimated coefficients occupy the same region. One can derive the fitting function of this locus (a small circle on the 3D unit sphere) and use it for

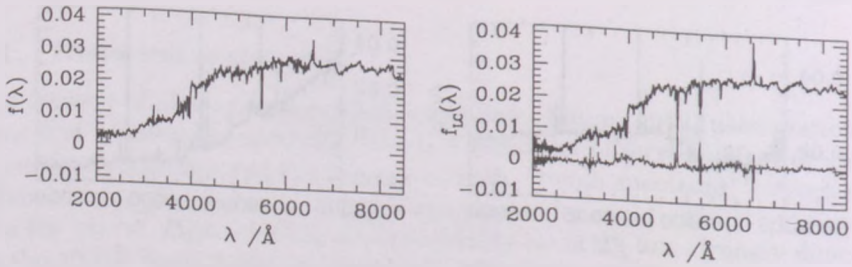

Figure 2: The SED of an Sb galaxy (left) and its projection to the subspace spanned by the eigetemplates. The thin line in the right panel is the residual.

photometric redshifts. This physical interpolation scheme yields more robust estimated SEDs even for very high redshift galaxies at $z \sim 3$.

2.2. Spectra from photometry

So far we have been dealing with SEDs directly derived from a template library. In other words, all possible spectra ever used were stuck in the same subspace determined by the orignal templates. The question is how we can get rid of this problem. Can we combine the advantages of the empirical and template fitting methods by somehow training the templates?

Since galaxies are at different redshifts, the filters sample their restframe spectra at different wavelengths. Having a large, deep enough, multicolor survey with spectroscopic redshifts allows us to statistically refine the underlying eigentemplates. Csabai et al. (2000) treats the problem by successively solving for parameters of templates, e.g. fluxes f_λ, and coefficients of objects.

Another approach is an iterative procedure (Budavári et al., 2000), where every step gives a new set of orthogonal basis that represents the photometry better. The skeleton of this algorithm is simple. First of all, we determine the most likely type and corresponding SED for all galaxies based on their known redshifts and then adjust spectra according to their photometry. We end up with a large number of SEDs. Applying the PCA again to these *repaired* spectra gives a new orthogonal basis, which spans a subspace different from the original.

The spectrum reparation is not trivial. A simple and effective way of doing it is solving an optimization problem for the spectrum, minimizing the deviation of simulated fluxes ($\tilde{f}_n$) from the actual photometry while keeping the resulting

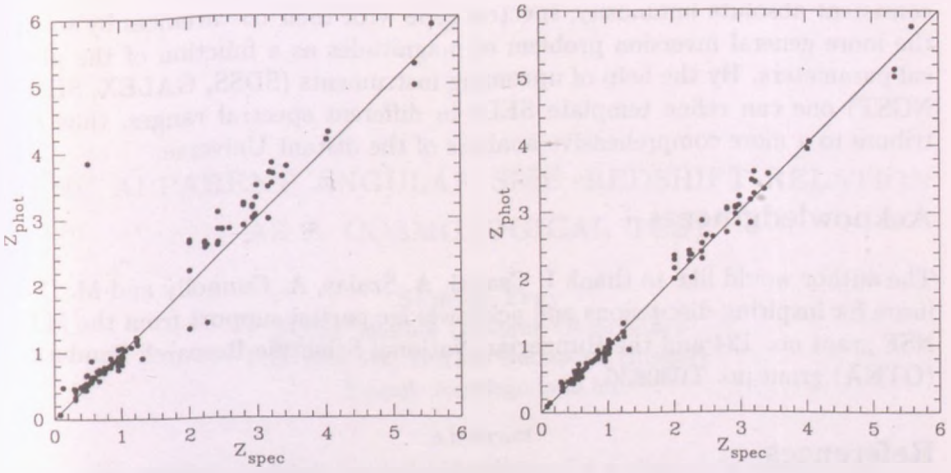

Figure 3: Comparing photometric redshifts to actual values shows a good agreement. The CWW based estimates (on the left) appear to have systematic errors and larger scatter than those based on trained spectral templates after 5 iterations.

spectrum $s_k = S(\lambda_k)$ close to the original $\hat{s}_k$.

$$\chi^2(\vec{s}) = \sum_n \left(\frac{f_n(\vec{s}) - \hat{f}_n}{\Delta_n} \right)^2 + \sum_k \left(\frac{s_k - \hat{s}_k}{\sigma_k} \right)^2 ,$$

where Δ_n is the photometric uncertainty in the nth band and σ_k is some function describing our prior information about the goodness of the current eigenspectra as a function of the wavelength.

Figure 3 compares photometric and spectroscopic redshifts. The left panel shows results from the CWW eigenspectra and in the right panel the improved estimates are seen computed from the trained eigenspectra after 5 iterations. The accuracy of the redshift prediction increased by a factor of 2.

3. Conclusions

Photometric redshift estimation provides an excellent tool for studying the evolution of galaxy properties. It is more than just redshifts! An estimator yields

consistent absolute luminosity, spectral type with their co-variances by solving the more general inversion problem of magnitudes as a function of the physical parameters. By the help of upcoming instruments (SDSS, GALEX, SIRTF, NGST) one can refine template SEDs in different spectral ranges, thus contribute to a more comprehensive analysis of the distant Universe.

Acknowledgments

The author would like to thank I. Csabai, A. Szalay, A. Connolly and M. Dickinson for inspiring discussions and acknowledge partial support from the MTA-NSF grant no. 124 and the Hungarian National Scientific Research Fundations (OTKA) grant no. T030836.

References

Baum, W.A., 1962, IAU Symposium No. 15, 390

Benítez, N., 2000, ApJ, 536, 571

Budavári, T., Szalay, A.S., Connolly, A.J., Csabai, I. & Dickinson, M.E., 2000, AJ, 120, 1588

Coleman, G.D., Wu., C.-C., & Weedman, D.W., 1980, ApJS, 43, 393

Connolly, A.J., Csabai, I., Szalay, A.S., Koo, D.C., Kron, R.G., & Munn, J.A., 1995a, AJ 110, 2655

Connolly, A.J., Szalay, A.S., Bershady, M.A., Kinney, A.L., & Calzetti, D., 1995b, AJ, 110, 1071

Csabai, I., Connolly, A.J., Szalay, A.S., & Budavári, T., 2000, AJ, 119, 69

Fernández-Soto, A., Lanzetta, K.M., & Yahil, A., 1999, ApJ, 513, 34

Gwyn, S.D.J., & Hartwick, F.D.A., 1996, ApJ, 468, L77

Kinney, A.L., Calzetti, D., Bohlin, R.C., McQuade, K., Storchi-Bergmann, T., & Schmitt, H.R., 1996, ApJ, 467, 38

Koo, D.C., 1985, AJ, 90, 148

Loh, E.D., & Spillar, E.J., 1986, ApJL, 303, L154

Sawicki, M.J., Lin, H., & Yee, H.K.C, 1997, AJ, 113, 1

Steidel, C.C., Giavalisco, M., Dickinson, M., & Adelberger, K.L., 1996, AJ, 112, 352

Williams, R.E., et al., 1996, AJ, 112, 1335

The apparent angular size–redshift relation as a cosmological test

Sándor Frey
FÖMI Satellite Geodetic Observatory
P.O. Box 546, H–1373 Budapest, Hungary
E-mail: frey@sgo.fomi.hu

Abstract

The apparent angular size–redshift relation for a class of "standard" objects is a classical test of cosmological models. Different models predict different dependence of the apparent angular size of objects having a constant metric size ("standard rods") with redshift. A brief review is given on how this test was used in the past, with special emphasis on objects observed with radio astronomical techniques. Recent results obtained from studying the parsec scale structures of radio-loud active galactic nuclei (AGNs) with the VLBI technique are summarised.

Keywords: *radio continuum: galaxies – cosmology: observations*

1. Introduction

Soon after the discovery of double-lobed radio sources, it was suggested by Hoyle (1959) to study the angular separation of the observed components in "Cygnus A-like" radio sources as a function of redshift z. According to Hoyle, if similar sources are found at higher redshifts, one can easily distinguish between the predictions of the Einstein–de Sitter and steady-state cosmological models. In the steady-state cosmology, the observed angular size θ of a standard rod with fixed linear size l would always decrease with increasing distance. In relativistic cosmological models with $q_0 > 0$ (non-empty Universe), the angular size–redshift dependence has a minimum at a particular redshift. The shape of the curve and the location of the observed minimum angular size depends on the parameters of the cosmological model (Fig. 1). In principle, this opens up a possibility to estimate the model parameters from measured data, namely the deceleration parameter q_0 and the cosmological constant Λ.

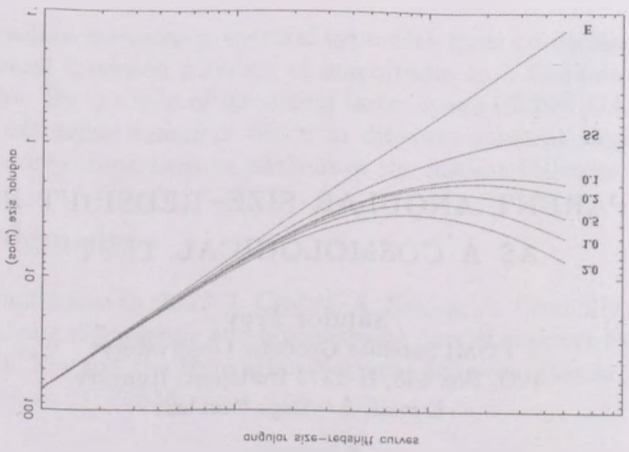

Figure 1: Theoretical $\theta(z)$ curves for a metric rod of $l = 10/h$ pc linear size (h is a dimensionless factor in the expression of the Hubble constant $H_0 h$, where $H_0 = 100$ km s^{-1} Mpc^{-1}). The straight line would represent a hypothetical Euclidean Universe (E) with $\theta \propto 1/z$, the other curves indicate the expected dependence in the steady-state (SS) model and various Friedmann models with different values of q_0.

There have been efforts to use measured angular diameters for galaxies at optical wavelengths for angular size–redshift tests. However, due to the small sizes in question, these measurements are limited by angular resolution provided by ground-based optical astronomy. Also, the surface brightness of quasar envelopes (galaxies) fades away rapidly with increasing z. Possible galaxy evolutionary effects may also play an important role and suppress the influence of the geometry of the Universe on the observed $\theta(z)$ dependence.

2. Double-lobed radio sources

There have been many attempts to use Hoyle's original idea to investigate the apparent angular size–redshift relation of double radio structures on scales from about tens to hundreds of arcseconds (e.g. Nilsson et al. (1993), and numerous references therein). In fact, the upper envelopes of the observed angular size versus redshift dependences can be used if the "rods" are oriented randomly with respect to the line of sight. Until recently, these studies achieved little suc-

cess in the sense that the observed data appeared to be consistent with a static Euclidean Universe (the straight line in Fig. 1) rather than any other feasible cosmological model. This can be interpreted as an effect of a decreasing intrinsic linear size with increasing redshift. Alternatively, it could be a selection effect leading to preferential detections of the higher luminosity sources at higher redshift which tend to be smaller due to an inverse correlation between luminosity and linear size (Singal, 1988). Curiously, the combination of cosmological and selection effects apparently cause the $\theta \propto 1/z$ relation.

Recently Buchalter et al. (1998) defined a sample of double-lobed quasars from the VLA FIRST survey at 1.4 GHz. Their new approach of carefully selecting a homogeneous and complete sample of 103 sources led to the conclusion that the data are entirely consistent with the Friedmann models with reasonable values of $\Omega_0 \leq 1$. ($\Omega_0 = 2q_0 + \Omega_\Lambda$, the ratio of the present density of the Universe to the critical density. $\Omega_\Lambda = \Lambda/3(H_0 h)^2$; $\Omega_0 = 2q_0$ in models with zero cosmological constant.) Although data are not sufficient to distinguish conclusively between the different models considered, including a set of models with non-zero Λ, the Euclidean model had a comparatively bad fit to the observed $\theta(z)$ dependence

3. Compact active galactic nuclei (AGNs)

Kellermann (1993a,b) and Gurvits (1993, 1994) pointed out that the angular size–redshift relation for compact radio sources observed with Very Long Baseline Interferometry (VLBI) shows a non-Euclidean behaviour, for the first time in the history of such tests. Kellermann (1993b) plotted the mean angular size of 82 sources versus redshift and concluded that data are in agreement with predictions of standard Friedmann–Robertson–Walker (FRW) models with q_0 close to 0.5, corresponding to the cosmological density near the critical value. According to Kellermann (1993b), compact radio sources, unlike double-lobed quasars, may largely be free from systematic evolutionary effects. These objects have relatively short radiative lifetime (up to several hundred years), which is negligible compared to the age of the Universe even at the earliest cosmological epochs (the highest redshifts) from where quasars are observable. Also, their size is much smaller than host galaxy sizes. Therefore their structure should be independent from the intergalactic medium which has systematically higher density at higher redshifts; this may, at least in part, be responsible for the apparently smaller intrinsic size of the double-lobed sources. Due to relativistic beaming, compact sources are thought to be aligned close to the line of sight,

and not randomly oriented in space like the extended radio sources. Angular sizes were defined as the separation between the peak and the most distant extended feature with peak brightness more than 2% of the core brightness in published VLBI contour maps.

In a similar and independent analysis based on a different sample, Gurvits (1994) found the same qualitative result (i.e. that the observed relation is non-Euclidean). Furthermore, he made an attempt to quantitatively estimate q_0, as well as the parameters characterizing the dependence of the source linear size on luminosity and emitted frequency. Using data on 337 sources from a non-imaging VLBI survey at 2.3 GHz, Gurvits (1994) found that the estimated value of $q_0 = 0.16 \pm 0.71$ is favorable for the open models within the framework of FRW cosmologies with $\Lambda = 0$.

The results above, especially those of Kellermann (1993b), stimulated extensive discussion and different aspects of the angular size–redshift test for compact radio sources were investigated in the past few years. Krauss & Schramm (1993) showed that the $\theta(z)$ relation, especially the location of the observed minimum depends sensitively on Λ. Careful analysis of the data, if evolutionary effects are ruled out, may place a limit on the value of the cosmological constant in a flat Universe ($\Omega = 1$) or on Ω in an open Universe. Others tried to fit cosmological models with more degrees of freedom to the same data set used by Kellermann (Stelmach, 1994; Jackson & Dodgson, 1996) and concluded that several models may equally be consistent with the observed dependence. A quantitative reanalysis of the Kellermann (1993b) data without binning by Stepanas & Saha (1995) showed that while the form of the angular size–redshift relation is consistent with $q_0 = 0.5$, it does not rule out extreme values of q_0 and thus does not usefully constrain the value of the deceleration parameter. Nearly at the same time, Kayser (1995) arrived at the same conclusion: data are not sufficient to rule out a significant part of the (Ω_0, Λ) plane. Dabrowsky et al. (1995) carried out Monte Carlo simulations to estimate, under certain assumptions, how many sources would be needed to constrain q_0 with reasonable error using the angular size–redshift test. The minimum numbers are ranging from 300 to 600, depending on the actual real value of q_0, the smaller sample being required for an open Universe ($q_0 = 0.25$).

Wilkinson et al. (1998) analysed VLBI images of 160 sources from the Caltech–Jodrell Bank flat-spectrum sample. Their angular size was defined as the distance between the core and the most distant component exceeding 1% of the peak brightness. They attempted to minimize the effect of the different linear resolution of low and high redshift sources arising from a nearly uniform angular resolution of their VLBI maps, and re-convolved each map to

a constant linear resolution. Their results are in qualitative agreement with the earlier results of Kellermann (1993b) and Gurvits (1994): the median angular sizes appear to decrease with increasing redshift until $z \sim 0.5$, then the $\theta(z)$ curve flattens off at $z \geq 0.5$.

Most recently, Gurvits et al. (1999) studied a sample of 330 AGNs, all having high resolution VLBI images at 5 GHz available in the literature. The analysis of the $\theta(z)$ dependence of this relatively large sample showed the same qualitative behaviour. They concluded that the milliarcsecond-scale VLBI data are consistent with standard FRW cosmologies with an open universe ($q_0 < 0.5$ and $\Lambda = 0$), without the need to introduce evolution of the source population or to appeal to selection effects due to the possible linear size–luminosity dependence (Gurvits et al., 1999). They found that eliminating the sources with extreme spectral properties helped to decrease the dispersion in the angular size data. A four-parameter regression model (Frey, 2000) was applied to estimate not only q_0 but the characteristic linear size of the sources and two parameters describing the phenomenological dependence of the angular size on source redshift and luminosity. Their best fit model gave $q_0 = 0.33 \pm 0.11$ (Gurvits et al., 1999).

There are a number of questions to be addressed in the future studies of the $\theta(z)$ relation on milliarcsecond scales in AGNs. First of all, the angular size can be defined in a different way from measuring jet and core angular distances in contour maps. Model fitting to VLBI visibility data has several advantages. This method allows us to combine observations made at a wide range of imaging sensitivity, and thus to increase the sample. It is also possible to combine observations made at different frequencies. The latter is important for designing a sample observed at similar rest-frame frequencies, rather than at a constant observed frequency, to minimize possible selection effect. The first demonstration of using VLBI visibility data led to promising results (Frey, 1999), in qualitative agreement with what was found in earlier $\theta(z)$ studies. The luminosity selection effect can mostly be avoided by involving VLBI observations of sources that are one or two orders of magnitude fainter than available at present. Constructing such a sample is currently feasible with the present capabilities of the VLBI technique and with the advent of large redshift surveys of extragalactic objects.

Acknowledgements

This work has been done in collaboration with L.I. Gurvits and K.I. Kellermann, with financial support received from the Netherlands Organisation for Scientific Research (NWO) and the Hungarian Scientific Research Fund (OTKA, grant

no. N31721 and T031723). The author acknowledges a grant received from the Hungarian Soros Foundation.

References

Buchalter A., Helfand D.J., Becker R.H., White R.L. 1998, ApJ 494, 503

Dabrowsky Y., Lasenby A., Saunders R. 1995, MNRAS 277, 753

Frey S. 1999, New Astron. Rev. 43, 761

Frey S. 2000, PhD Thesis, Eötvös University, Budapest

Gurvits L.I. 1993, in: Davis R.J., Booth R.S. (eds.), Sub-arcsecond Radio Astronomy, Cambridge University Press, 380

Gurvits L.I. 1994, ApJ 425, 442

Gurvits L.I., Kellermann K.I., Frey S. 1999, A&A 342, 378

Hoyle F. 1959, in: Bracewell R.N. (ed.), Proc. IAU Symposium 9, Paris Symposium on Radio Astronomy, Stanford University Press, 529

Jackson J.C., Dodgson M. 1996, MNRAS 278, 603

Kayser R. 1995, A&A 294, L21

Kellermann K.I. 1993a, in: Davis R.J., Booth R.S. (eds.), Sub-arcsecond Radio Astronomy, Cambridge University Press, 386

Kellermann K.I. 1993b, Nature 361, 134

Krauss L.M., Schramm D.N. 1993, ApJ 405, L43

Nilsson K., Valtonen M.J., Kotilainen J., Jaakkola T. 1993, ApJ 413, 453

Singal A.K. 1988, MNRAS 233, 87

Stelmach J. 1994, ApJ 428, 61

Stepanas P.G., Saha P. 1995, MNRAS 272, L13

Wilkinson P.N., Browne I.W.A., Alcock D., et al. 1998, in: Bremer M.N., Jackson N., Pérez-Fournon I. (eds.), Observational Cosmology with New Radio Surveys, Kluwer, Dordrecht, 221

Microquasars and SS433

Zsolt Paragi*
FÖMI Satellite Geodetic Observatory, Penc
H-1363 Budapest, P.O.Box 546., Hungary
E-mail:paragi@sgo.fomi.hu

Abstract

I shortly introduce radio-jet X-ray binaries (microquasars), and review recent VLBI observational results on SS433.
KEYWORDS:*stars: individual: SS433 – ISM: jets and outflows – radio continuum: stars*

1. Introduction

Radio-jet X-ray binaries (RJXRB) consist of a normal star and a compact object (neutron star or black hole). The normal star loses mass to the compact object in the form of a dense stellar wind or Roche-lobe outflow. This process is believed to take place through an accretion disk (at least in the latter case). Part of the accreted matter leaves the system near the poles of the black hole in well collimated particle beams, jets. Relativistic electrons (and positrons?) moving in the magnetic field of the jet produce synchrotron radiation which can be observed in the radio regime. Many of the radio-jet systems was discovered in the last ten years. Some of these showed apparent superluminal motion within the jet, which was only detectable in the far away quasars before. The term *microquasar* (Mirabel & Rodríguez, 1999) became widely used in the recent years for these objects. It is believed that the similarity between quasars and microquasars is not only morphological, but there is a close physical analogy. Accretion processes and matter ejection events into the jets can be easier studied

*This work has been carried out in collaboration with I. Fejes, R.C. Vermeulen, R.T. Schilizzi, R.E. Spencer and A.M. Stirling. Financial support is acknowledged from the Hungarian Space Office (MŰI), the Netherlands Organization for Scientific Research (NWO) and the Hungarian Scientific Research Fund (OTKA, grant no. N31721 & T031723).

in the low-mass Galactic objets, because e.g. the relevant timescales are much shorter than in the central engine of active galaxies.

2. Jets and disks in microquasars

Only a small fraction of X-ray binaries are detected in the radio regime. These systems are capable of accelerating electrons to relativistic speeds, which produce synchrotron radio emission moving in magnetic field. Radio jets were detected in only a part of the radio–loud objects; about a dozen well established RJXRBs are known to date.

According to our present knowledge, the inner region of the accretion disk is responsible for the formation of radio jets (e.g. Fender (1999)). Because most of the RJXRBs are believed to be powered by black holes, the magnetic field for collimating the jets and accelerate the particles etc. must originate in the disk itself. These processes are probably similar in systems with different types of compact objects, and there is no reason to restrict the usage of term *microquasar* only to black hole candidate RJXRBs with superluminal jets. It is interesting to note that while systems with low magnetic field neutron stars may power radio jets (like Cir X-1), X-ray pulsars (containing neutron stars with $\sim 10^{12}$ G magnetic fields) are not detected in radio wavelengths. It seems that strong compact object magnetic fields prevent the formation of a stable inner accretion disk region, and thus the formation of radio jets (Fender et al., 1997).

3. SS433 as a microquasar

The first relativistic radio-jet source discovered in the Galaxy was SS433. On milliarcsecond (mas) scales the source shows a permanent core-wing morphology (unlike the compact, centre brightened quasar radio cores), as was shown in high resolution Very Long Baseline Interferometry (VLBI) experiments by Vermeulen et al. (1993). Bright knots (or plasmons, well defined jet components) emerge from time to time from this core-region and move away with $v = 0.26$c, according to the well established kinematic model of the precessing radio beams. The maximum brightness of these plasmons is reached at about 50 milliarcsecond to the centre, which became known as the brightening zone. On arcsecond scales the radio beams are corkscrew-shaped due to the 162.5 days precession of the source. Results of VLBI observations made in 1995 and 1998 are described below. Details of these experiments can be found in Paragi (2000).

3.1. Core region: compact jets and their environment

It was shown by Paragi et al. (1998, 1999a) that the core region of SS433 can be divided into three parts: eastern core-wing (E_{cw}), *Central Radio Gap* (see Fig. 2), and western core-wing (W_{cw}). The core-wings are the inner part of the approaching and receding radio beams, respectively[1]. Additional radio components were discovered orthogonally to the "normal" jets. As these cannot be directly related to the radio beams, which were ejected near the poles of the compact object, we will refer to this region as the Equatorial Emission Region (Fig. 1). Similar phenomenon has never been observed in microquasars before.

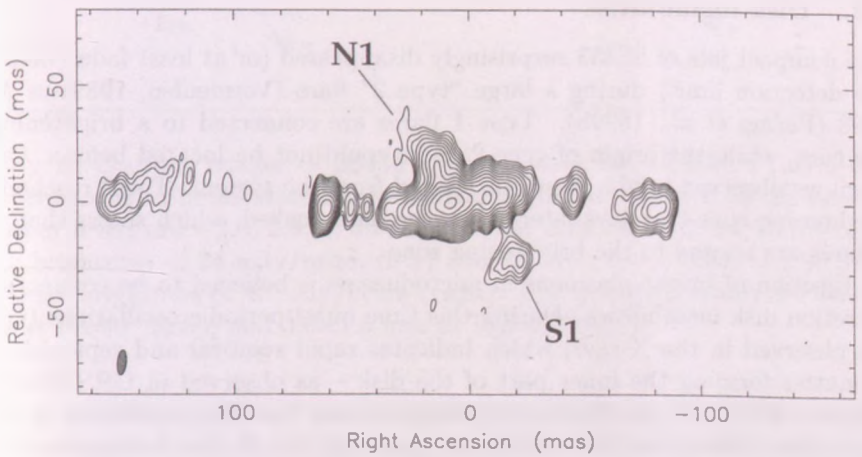

Figure 1: Contour image of SS433 on 6/7 June 1998 at 1.6 GHz, made from combined EVN and VLBA+Y1 data. Components in the Equatorial Emission Region are indicated by N1 and S1. Contour levels are −1, 1, 1.4, 2, 2.8, 4, 5.7, 8, 11.3, 16, 22.6, 32, 45.3, 64, 90.5% of the peak brightness of 39 mJy/beam. The restoring beam is 10.8×3.8 mas at PA=−6°

Two sided core-wing emission and central absorption gap is predicted by various conical jet models. It is because the absorption coefficient of synchrotron radiaton increase, while its emission coefficient decrease with the increasing magnetic field closer to the central engine. The peak brightness of a core-wing is reached at $\tau \sim 1$ optical depth. Because the optical depth is frequency

[1]In most of the time E_{cw} is the approaching jet side, and W_{cw} is the receding one. There is only a short timerange during the precession cycle when the opposite is true.

dependent, the separation of the E_{cw} and W_{cw} peaks is expected to depend on frequency as well. Kinematic modelling of jet components showed that the central engine of SS433 is located within the Central Radio Gap, and the position shift of the core-wings was also detected between 1.6 and 5 GHz observing frequencies, in accordance with the above compact jet model[2] predictions.

Conical jet models have already been invoked to explain the flat high frequency radio spectra of microquasar cores (e.g. Fender et al., 2000). But SS433 was the first Galactic source where the compact jet region was resolved, and some prediction of the jet models could be tested (Paragi et al., 1999a).

3.2. Disk instabilities

The compact jets of SS433 surprisingly disappeared (or at least faded below to the detection limit) during a large "type 2" flare (Vermeulen, 1989) in April 1998 (Paragi et al., 1999b). Type 1 flares are connected to a brightening of the core, while the origin of type 2 flares could not be located before. On 18 April we observed bright plasmons ejected from the system. These reached the brightening zone two days later, when the flare peaked, which shows that type 2 flares are related to the brightening zone.

Ejection of bright plasmons in microquasars is believed to be connected to accretion disk instabilities. During this time quasi-periodic oscillations (QPO) are observed in the X-rays, which indicates rapid removal and replenishment of matter forming the inner part of the disk – as observed in GRS 1915+105 (Belloni, 1997). It was already emphasized above that the presence of a stable inner disk is the prerequisite of forming a radio jet. If this is temporarily destroyed during a large flare, the supply of relativistic electrons stops, and the radio jets disappear as well. In SS433 we exclude the external absorption of the compact jet region, and suggest that the observed bright plasmons were ejected following the complete evacuation of the inner accretion disk, by analogy to GRS 1915+105.

3.3. Equatorial outflow

It was proposed by Stirling et al. (1997) that the ionized stellar wind would absorb the inner radio jets. It was shown by Paragi et al. (1999a) that free-free absorption really occurs; the inner 5–6 mas (~ 25 AU) is completely absorbed

[2]Conical jet models were first applied to the radio cores of quasars, which were interpreted as compact unresolved jets.

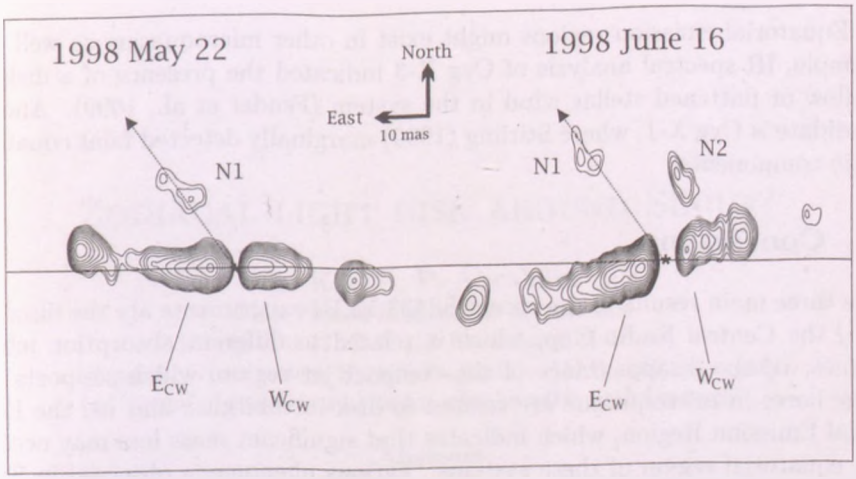

Figure 2: Contour images of SS433 observed with the VLBA+Y1 at 5 GHz at two epochs. The location of the central engine is indicated by an asterisk. Contour levels are -2.8, 2.8, 4, 5.7, 8, 11.3, 16, 22.6, 32, 45.3, 64, 90.5% of the peak brightness of 24 mJy/beam (left) and -1.41, 1.41, 2, 2.83, ..., 90.5% of the peak brightness of 48 mJy/beam (right). The restoring beams are 4.1×1.9 mas at PA=0° (left), and 3.6×1.5 mas at PA=0° (right)

even at 22 GHz, in spite of the fact that the free-free opacity is inversely proportional to the square of frequency. In case the ionized medium is from a spherically symmetric stellar wind, the required mass outflow rate to the Equatorial Emission Region is unexpectedly high ($10^{-5}\,M_\odot$/yr). The wind (or other type of matter outflow) must be confined into a disk-like geometry. This disk is well bounded and/or becomes largely neutral outside a radius of 2×10^{14} cm.

The position angle and radio structure of components located in the Equatorial Emission Region change with time. I stress that these components are quite dissimilar to the plasmons ejected into the radio beams. One of the equatorial components were detected at three epochs (N1, see Fig. 1 and Fig. 2). The determined proper motion of N1 is $\mu = 0.14$ mas/day, which translates to $1200/\sin(i)$ km/s (where i is the angle between the velocity vector and the line of sight). This is in agreement with typical stellar wind speeds observed in the system. Further observations are needed to confirm these results, because the position measurements are difficult due to the extended component structure and to the lack of a well established reference point.

Equatorial emission regions might exist in other microquasars as well. For example, IR spectral analyzis of Cyg X-3 indicated the presence of a disk-like outflow or flattened stellar wind in the system (Fender et al., 1999). Another candidate is Cyg X-1, where Stirling (1999) marginally detected faint equatorial radio components.

4. Conclusions

The three main results of the recent SS433 VLBI experiments are the discovery of *i)* the Central Radio Gap, which is related to different absorption mechanismes; *ii)* the disappearance of the compact jet region, which supports that large flares in microquasars are related to disk instabilities; and *iii)* the Equatorial Emission Region, which indicates that significant mass loss may occur in the equatorial region of these systems. Various phenomena observed in SS433 might be detected in other microquasars as well.

References

Belloni T., Méndez M., King A.R. et al. 1997, ApJ 479, L145
Fender R.P. 1999, astro-ph/9907050
Fender R.P., Bell Burnell S.J., Waltman E.B. 1997, Vistas Astron. 41, 3
Fender R.P., Hanson M.M., Pooley G.G. 1999, MNRAS 308, 473
Fender R.P., Pooley G.G., Durouchoux P. et al. 2000, MNRAS 312, 853
Mirabel I.F., Rodríguez L.F. 1999, ARA&A 37, 409
Paragi Z. 2000, Ph.D. Dissertation, Loránd Eötvös Univ., Budapest
Paragi Z., Vermeulen R.C., Fejes I. et al. 1998, New Astron. Rev. 42, 641
Paragi Z., Vermeulen R.C., Fejes I. et al. 1999a, A&A 348, 910
Paragi Z., Vermeulen R.C., Fejes I. et al. 1999b, New Astron. Rev. 43, 553
Stirling A.M. 1999, Ph.D. Dissertation, University of Manchester
Stirling A.M., Spencer R.E., Watson S.K. 1997, Vistas Astron. 41, 197
Vermeulen R.C. 1989, Ph.D. Dissertation, Leiden University
Vermeulen R.C., Schilizzi R.T., Spencer R.E. et al. 1993, A&A 270, 177

Zodiacal light disk around Sirius?

Cs. Kiss[1,2], P. Ábrahám[1,2]
[1]Max-Planck-Institut für Astronomie
Königstuhl 17, D-69117 Heidelberg, Germany
[2]Konkoly Observatory, H-1525 Budapest, P.O.Box 67., Hungary
E-mail:pkisscs@astro.elte.hu, abraham@mpia-hd.mpg.de

Abstract

We have detected a far-infrared excess in the ISOPHOT measurements of the brightest star of the night sky, Sirius. The most plausible explanation of this excess would be the presence of a dust disk in the Sirius system. Calculations have shown that the parameters of the possible dust disk are intermediate between that of the solar system's zodiacal light cloud and that of Vega-type stellar systems. This is lowest mass disk ever detected ($M_{disk} \approx 1/500 \times M_{Moon}$) and may be the first example of very low mass disks outside our solar system. If these kind of disks are common around A-type stars, the detection of planets by mid-infrared interferometry might be limited by the radiation of the disk as well.
Keywords: *circumstellar dust, VEGA-like stars, individual objects: α CMa*

1. Introduction

Sirius, the brightest star of the night sky has been a major celestial object for many cultures for thousands of years in man's history. Today it is an important calibrator star especially in the mid-infrared, after the discovery of the dust disk around Vega (Cohen et al. (1987)). As part of the calibration work on ISOPHOT (Lemke et al. (1996)) the photometer on-board the Infrared Space Observatory (Kessler et al. (1996)), we have checked the photometric accuracy of point source fluxes derived from small far-infrared maps. While most standard stars investigated we obtained flux densities closed to the model predicition, Sirius showed systematically too high flux densities at both 60 and 100 μm.

Systematic studies performed by the IRAS and ISO satellites revealed far-infrared access in a significant fraction of main-sequence stars. It is generally

believed that this far-infrared excess is originated from a circumstellar disk mainly build up of dust particles. The first example of such a disk around a star was α Lyr, Vega (therefore the name 'Vega-phenomenon', for a detailed description see e.g. Backman & Paresce (1993) and Habing et al. (1999)). Using the ISOPHOT instrument the spatial extension of the dust was detected in the case of two stars with nearly edge-on disks, Vega (Walker et al. (1999)) and β Pic (Heinrichsen et al. (1999)). The disk temperatures detected so far were between 60 and 120 K, and have about the mass of the Moon. In most cases the spectral energy distribution of the dust disk can be described by a modified blackbody, with β=–1 emissivity law ($F_\nu = \nu^\beta \cdot B_\nu(T)$). Direct imaging of HR 4796A at near- and mid-infrared wavelenghts (Telesco et al. (2000)) revealed that the bulk of the circumstellar disk resides in a sharply definied ring with a radius of $\sim$70 AU.

A similar picture may be valid for other Vega-type systems, too. In the case of the known systems the dust particles absorb 10^{-4} – 10^{-5} part of the stellar radiation which is reemitted in the infrared. The mass, size and fractional luminosity values are several orders of magnitudes higher than the corresponding parameters of the closest circumstellar disk, the Solar System Zodiacal Light cloud ($M \approx 1/500\,M_\odot$, $R = 2-3$ AU, $f \approx 2.1 \cdot 10^{-7}$). There are no circumstellar disk with parameters similar to that of the zodiacal light cloud detected so far. However, due to the low fractional luminosity, such systems would show only a small deviation from the flux density of the stellar photosphere, which is hard to detect. Therefore it is a question how much fraction of the stellar systems can harbour a faint disk. The best candidate for the detection of a faint disk would be a nearby star which is bright enough even in the far-infrared to have on excess over the detection limit. And Sirius is so...

2. Observations and data analysis

In the ISOPHOT archive we found Sirius observation at 3.3, 12, 25, 60, 100 and 170 μm, performed in various observing modes. Up to 25 μm the derived flux densities followed the model predicitions within the uncertainities. At 170 μm the derivation of the absolute flux is very uncertain due to the very strong cirrus field around the star. At 60 and 100 μm the extracted flux densities were significantly higher than the predicted flux of the photospere. In order to check if the excess is real, we have selected some stars (HR 617, HR 1657, HR 6705, HR 7557, HR 7980) having a brightness similar to that of Sirius and reduced their observations as well. We were using these observations to calibrate the

Sirius measurements independently from the standard calibration process. We used the Phot Interactive Analysis (PIA) software for the data reduction. In the case of minimaps we used the 'pairwise' [1] method for deglitching. Finally we derived an excess flux density of $\mathbf{E_{60} = 205 \pm 70\,mJy}$ at 60 μm and $\mathbf{E_{100} = 120 \pm 56\,mJy}$ at 100 μm. In the following we use these parameters to determine the properties of a possible dust disk in the Sirius system. In order to improve the calibration in the range of bright stars, a reprocessing of all the available data and an extension to measurements which were not in use before is still in progress, therefore the final excess values and all the derived properties may change considerably.

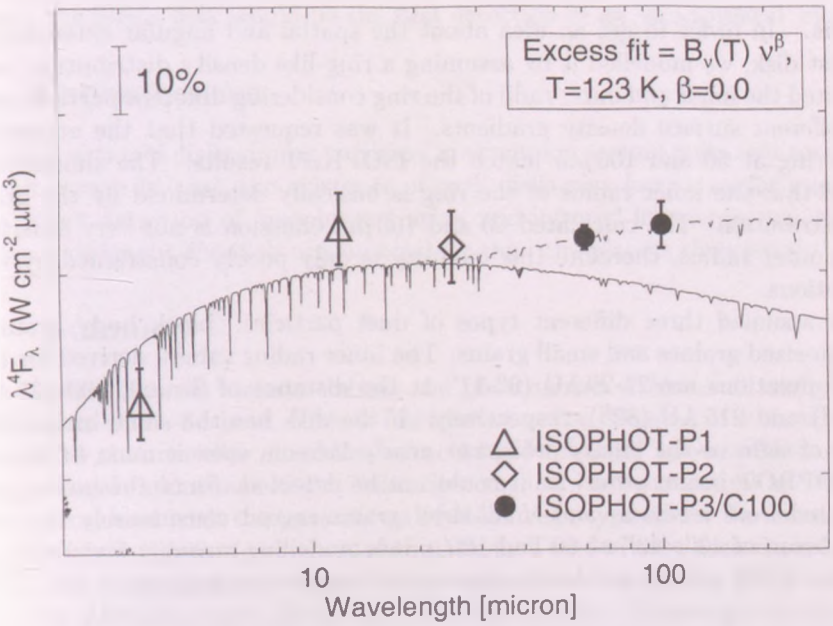

Figure 1: Spectral energy distribution of the Sirius model by M. Cohen (continous line), with ISOPHOT measurements overplotted

[1] by M. Stickel, MPIA, Heidelberg

3. A disk around Sirius?

Assuming that the observed far-infrared excess is real, we checked it the measured excess could originate from the with dwarf companion of Sirius A. Following the method by (Plets & Vynckier (1999)) we calculated the FIR flux density of Sirius B (B=8.41, V=8.44), and obtained 0.47 mJy at 60 μm, two orders of magnitudes below the measured value. We also calculated how bright a giant planet (like Jupiter) would be at 60 μm, but the calculated flux density is even lower than that of the white dwarf. Thus the most plausible explanation for the excess is a circumstellar dust disk.

Radius. In order to get an idea about the spatial and angular extension of the dust disk, we modelled it by assuming a ring-like density distribution, and calculated the inner and outer radii of the ring considering different particle sizes and different surface density gradients. It was requested that the emissions of the ring at 60 and 100 μm match the ISOPHOT results. The simulations showed that the inner radius of the ring is basically determined by the grain size distribution. The calculated 60 and 100 μm emission is not very sensitive to the outer radius, therefore this quantity is only poorly constrained by our calculations.

We assumed three different types of dust particles: black body graines, medium-sized graines and small grains. The inner radius values, derived for the dust populations are 24-29 AU (9″-11″ at the distance of Sirius), 100-125 AU (38-47″) and 215 AU (82″), respectively. If the disk has the same inclination to line-of-sight as the binary orbit, i.e. nearly face-on, then it must fit within the ISOPHOT beam, otherwise it could not be detected. Since the inner radii calculated from medium- and small-sized grains exceed considerably the size of the beam of 43″×43″ at 60 and 100 μ, our modelling strongly favours large particles which radiate as blackbodies even at longer wavelengths.

Temperature. The 60 and 100 μm excess values define a balckbody color temperature of 123 K. A comparison of this value with the literature demonstrates that temperature of the Sirius disk falls in the upper end of the range observed in other Vega-type disks (60 and 120 K).

Disk mass. The mass of circumstellar dust was calculated assuming an absorption coefficient $\kappa(60\mu\mathrm{m}) = \kappa(850\mu\mathrm{m}) = 1.7\,\mathrm{cm^2 g^{-1}}$. The result is $\sim 1/500$ of the mass of the Moon, showing that the Sirius disk may be the least massive

circumstellar disk ever detected. This value is very closed to that of the zodiacal light cloud of the Solar System.

The fractional luminosity. Fractional luminosity, f, is the ratio of the far-infrared excess to the star's bolometric luminosity. We calculated this value by using the formula of Backman et al. (1987). The result of $2.3 \cdot 10^{-7}$ is very closed to the typical fractional luminosity of the Solar System's zodiacal light cloud, but singificantly lower than that of Vega-type disks. This result (and the blackbody SED) may indicate that the circumstellar disk of Sirius is more similar to the zodiacal light cloud than to other Vega-type disks. As far as we know, the Sirius disk would be the first detection of an 'exo-zodiacal' cloud.

4. Consequences

It is a question if disks similar to Sirius' are common around main sequence stars. If the answer is 'yes', the existence of such disks may have a major impact on the direct detection of 'exoplanets' using mid-infrared interferometry, since at those wavelenght the disk can be brighter than the planets themselves.

5. Summary

We detected excess emission above the photosphere of Sirius at both 60 and 100 μm on the 2–3σ level. This is interpreted as the emission of a circumstellar disk. The circumstellar cloud has a fractional luminosity very similar to that of the zodiacal light cloud in the Solar System, but its temperature and size are most consistent with the parameters of other Vega-type disks. The mass of the Sirius disk is 1/500 of the mass of the Moon. The derived physical parameters place the Sirius disk between the Vega-type disks observed by IRAS and ISO and the Zodiacal Light Cloud in out Solar System. This might be the first example for a class of very faint disks which could be ubiquitious around main sequence stars.

References

Backman D.E., Gillett F.C., Low F.J., Neugebauer G., Witteborn F.C., Aumann H.H., 1987, BAAS 19, 830

Backman D.E., Paresce F., 1993, "Main-sequence stars with circumstellar solid material–The VEGA-phenomenon", In: Protostars and Planets III., p. 1253

Cohen M., Schwartz D.E., Chokshi A., Walker R.G., 1987, AJ 93, 1199

Habing H., Dominik C., Jourdain de Muizon M. et al., 1999, Nature 401, 456

Heinrichsen I., Walker H.J., Klaas U., Sylvester R.J., Lemke D., 1999, MNRAS 304, 589

Lemke D., Klaas U., Abolins J., 1996, A&A 315L, 64

Kessler M.F., Steinz J.A., Anderegg M.E. et al., 1996, A&A 315L, 27

Plets H., Vynckier C., 1999, A&A 343, 496

Telesco C.M., Fisher R.S., Piña R.K. et al., 2000, ApJ 530, 329

Walker H.J., Heinrichsen I., Klaas U., Sylvester R.J., 1999, "Infrared mapping of the dust around main sequence stars", In: The Universe as seen by ISO, eds. Cox P. and Kessler M.F., ESA SP-427, p. 425

Investigation of far infrared loops in the 2nd Galactic Quadrant

A. Moór[1], Cs. Kiss[2], V.L. Tóth[1,3]
[1]Department of Astronomy, Eötvös Loránd University,
H-1518 Budapest, P.O.Box 32., Hungary
[2]Konkoly Observatory, H-1525 Budapest, P.O.Box 67., Hungary
[3]Helsinki Univ. Obs., P.O.Box 14, 00014 University of Helsinki, Finland
E-mail:[1]moor@astro.elte.hu, [2]pkisscs@astro.elte.hu, [3]lvtoth@astro.elte.hu

Abstract

We have searched the IRAS 100 μm images for intensity enhancements, which may indicate an interaction of high pressure events with the interstellar medium. We have invented 135 far infrared loops, and analysed their essential statistical properties. Our results will have an impact on the better understanding of the large scale structure of the ISM in the galactic neighbourhood of our solar system.
KEYWORDS: *ISM, far infrared, galactic structure*

1. Introduction

Supernova explosions and stellar winds of massive stars heat up their environment and sweep out the gas and dust into a dense expanding shell. Arcs and loops are reported in many tracers of the ISM, including radio, infrared, optical, ultraviolet and X-ray wavelengths. Brand & Zealey (1975) catalogued a number of optical emission, absorption and radio continuum loops. Heiles (1979) investigated the $l = 10° - 250°$ and $-10° \leq b \leq 10°$ sky area in HI and found 63 shells. Using the same HI survey Hu (1981) invented 50 new shells at higher galactic latitudes. At $|b| \leq 65$ Heiles (1984) culminated 42 shells, supershells and worms.

Koo & Heiles (1991) studied the environment of 103 SNRs and detected 15 of them associated with high velocity HI gas, which were explained as rapidly expanding SNR shells, probably accelerated by the SN blast wave. Koo et al.

(1992) presented the parameters of 118 galactic worms based on infrared and HI data. Schwartz (1987) found 16 star-forming loops on IRAS images whose size and gas density are typical of molecular clouds. His work was restricted to $60° \leq l \leq 300°$ and $|b| \leq 7°$. A remarkable example of high velocity cloud – galactic disk interactions is the North Celestial Pole (NCP) loop (Meyerdierks et al. (1991)).

Our main aim was to search for density enhancements in the interstellar medium showing a structure similar to that generated by supernova explosions, stellar winds or other high pressure events.

In Sect. 2. we describe our input data and data reduction methods, in Sect. 3. we present our results and discuss the statistical results on the distribution of our objects.

2. Data analysis

2.1. Quest for loops on ISSA maps

We used the 60 and 100 μm ISSA plates (Wheelock et al. (1994)) in order to study the apparent structure of dust emission in the 2nd Galactic Quadrant. Our investigation required huge connected areas, much larger than the $12°.5 \times 12°.5$ sized ISSA maps. Therefore we created composite images of the individual ISSA plates using the "geom" and "mosaic" procedures of the IPAC-Skyview package. These images were built up typically from ~10-15 ISSA plates (with a final size of $\sim 40° \times 40°$, which limits the maximal characteristic size of our objects as well). On the other hand, due to the relatively large size of the investigated regions, structures with a size of $\leq 1°$ were not searched.

The quest for loop-like intensity enhancements were performed by eye on our mosaic maps. We have choosen this way of investigation because man's eye is the best pattern-recognition tool, especially in such cases when strict role can hardly be definied. Loops by our definition must show an excess FIR intensity in a curved shell, at least 60% of a complete ellipse-shaped ring. A loop may consist of a set of bright, more or less isolated, extended spots, or may be a diffuse ring or part of a ring.

2.2. Significancy of the loops

Pattern recognition by eye may introduce many subjective effects. In order to check if our loops really show the expected properties in the spatial distribution of their FIR emission, we calculated a "significancy" parameter for all of our

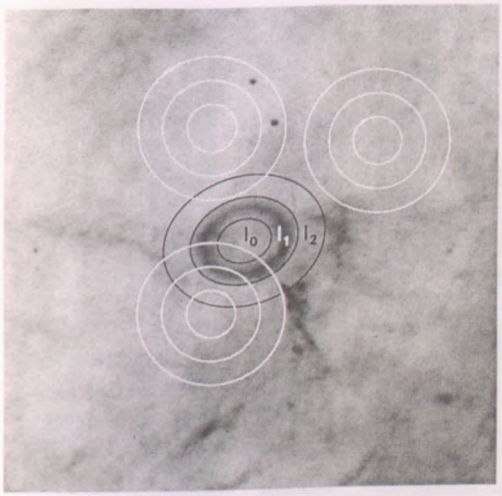

Figure 1: Visualization of the configuration to measure the significancy S of the fitted ellipse. The average surface brightnesses measured inside, in and outside the ellipse (black ellipses) are marked by I_0, I_1 and I_2, respectively. The radii of the reference rings (white circles, centered at random sky positions) are the geometrical mean of the half minor and major axis of the ellipse (only three reference rings are shown from 25). See the text for more details.

loops. We derived average intensity values for three areas, one inside, one around and one outside our fitted ellipse (see I_0, I_1 and I_2 in Fig. 1, respectively). Then we calculated a Q_{ell} value, defined as:

$$Q_{ell} = \frac{1}{2} \cdot (2 \cdot I_1 - (I_0 + I_2)) \tag{1}$$

The higher the value of Q_{ell} the higher the intensity excess of the loop over the background. It is needed to investigate if this certain Q_{ell} value is significantly higher than the ones that can be measured around an arbitrary position in the neighbourhood of the loop. Therefore we performed this calculation for 25 rings, with a center position randomly distributed around the investigated ellipse. The radii of these rings are the geometrical mean of the appropriate half minor and major axis of the ellipse. From these we derived the Q_{ring} value in a similar way as in the case of the ellipse, the mean $\overline{Q}_{ring}$ and the dispersion $\sigma(Q_{ring})$ of this data set. Then the 'significancy' S of the loop was calculated as:

$$S = \frac{Q_{ell} - \overline{Q}_{ring}}{\sigma(Q_{ring})} \tag{2}$$

According to our experiences, in the case of formerly known loops the significancy of the loops were $S \sim 3$. We used this S parameter as a quality indicator. Although the most prominent loops has a high S, we included the loops with

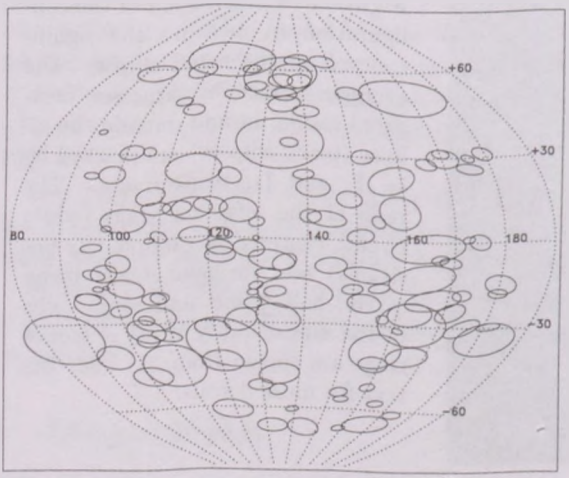

Figure 2: Distribution of our 135 far infrared loops found in the IInd Galactic Quadrant (galactic coordinate system)

S≤3 in our catalogue as well, since in certain cases bright fore- or background objects may appear in the inner or outer parts of the loops. These can notably affect the significancy parameter, however they belong neither to the loop nor to the more extended background.

3. Results

We have found 135 loops in the IInd Galactic Quadrant. The catalogue of the infrared loops in the IInd Galactic Quadrant is available at the WWW page: **http://astro.elte.hu/IRASLoops/IRASLoops.html**. The distribution of our 135 loops in the sky is presented in Fig. 2. In Fig. 3 we present the essential statistical diagrams.

We have tested the hypothesis, that on the Northern and on the Southern Hemisphere the centers of the loops are drawn from the same distribution. The Kolmogorov-Smirnov test has shown that our hypothesis could not be accepted at a 80% confidence level.

It is possible to define a characteristic size for our loops, derived from the half minor- and major axis of fitted ellipses as $\overline{R}_{\rm eff} = \langle\sqrt{a_i \times b_i}\rangle_i$. We obtained $\overline{R}_{\rm eff} = 2.8°$. We found no correlation between the galactic latitude of the loop centers and the effective radii of our loops, neither on the northern nor on the southern galactic hemisphere.

As it can be seen in Fig. 3, the number of the loops at high galactic latitude

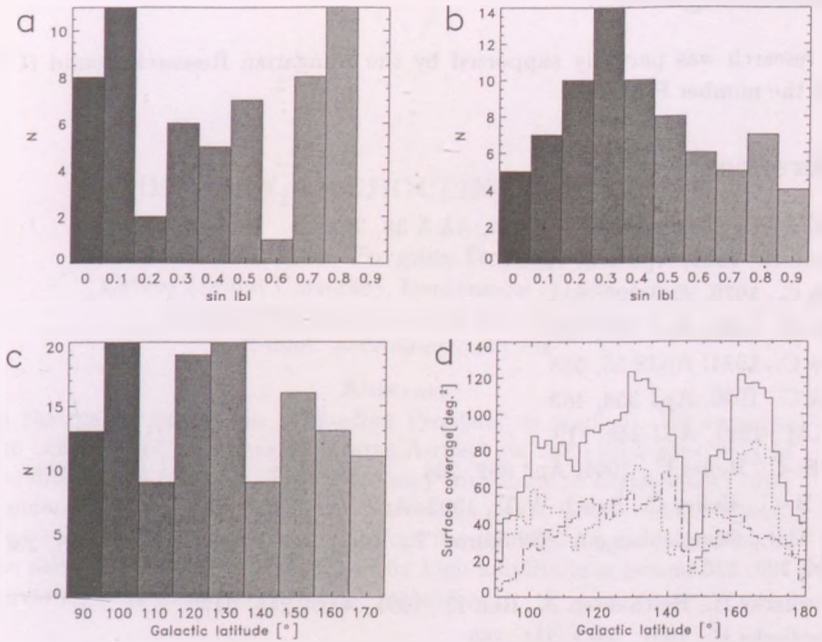

Figure 3: **a**–**d** Statistical diagrams **a** distribution of the latitudes of the loop centers on the Northern Galactic Hemisphere; **b** the same as **a** but for the Southern Galactic Hemisphere; **c** distribution of the longitudes of the loops centers; **d** surface coverage of the loop areas; histogram with dotted lines: southern hemisphere, dash-dotted line: northern hemisphere, solid line: sum of the two hemispheres

are relatively high, compared to the expected number derived by assuming the classical loop-generating processes (OB-stars, SN explosions, etc.) and their scale-height in the Milky Way. E.g. the distribution of our loops are very different from that of classical O stars. High latitude loops may be created by the infall of HVCs into the galactic disk (Meyerdierks et al. (1991)), results of Ia-type SN explosions or formed by the evolution of a superbubble in a turbulent, multi-phased and magnetized ISM (Korpi et al. (1999)).

Acknowledgments

This research was partially supported by the Hungarian Research Found (OTKA), under the number F-022566

References

Brand P.W.J.L., Zealey W.J., 1975, A&A 38, 363
Ferriere K., 1998, ApJ 503, 700
Heiles C., 1979, ApJ 229, 533
Heiles C., 1980, ApJ 235, 833
Heiles C., 1984, ApJS 55, 585
Heiles C., 1990, ApJ 354, 483
Hu E.M., 1981, ApJ 248, 119
Koo B.-C., Heiles C., 1991, ApJ 382, 204
Koo, B.-C., Heiles C., Reach W.T., 1992, ApJ 390, 108
Koo, M.J., Brandenburg A., Shukurov T., Tuominen I., 1999, A&A 350, 230 1976, ApJ 205, 226
Meyerdierks H., Heithausen A., Reif K., 1991, A&A 245, 247
Meyerdierks H., 1991, A&A 251, 269
Schwartz P.R., 1987, ApJ 320, 258
Wheelock S.L., 1994, (Pasadena:JPL94-11)

The Thin Tachocline Problem

Emese Forgács-Dajka
Eötvös Loránd University, Department of Astronomy
H-1518 Budapest, P.O.Box 32., Hungary
E-mail: andro@astro.elte.hu

Abstract

In this paper the "Thin Tachocline Problem" is studied. We examine the influence of an assumed inverse Λ-effect on the radial spreading of the differential rotation. This effect may contribute to horizontal angular momentum transport below the convection zone. Our results indicate that an inverse Λ-effect can only reduce the thickness of the tachocline to the observed value if an unrealistically high amplitude is assumed.
KEYWORDS: *Sun:interior; rotation; tachocline*

1. Introduction

Helioseismic measurements indicate the existence of a transition layer (the tachocline) between the differentially rotating convection zone and the rigidly rotating radiative interior. According to Schou et al. (1998) the depth of the tachocline is $0.70-0.71R_{\odot}$, and its thickness is $0.05-0.1R_{\odot}$ (see also Kosovichev 1996). Previous hydrodynamical models indicated that the differential rotation extends into the deep layers of the radiative interior, implying that the transition layer is thick. According to the semianalytical calculation of Spiegel & Zahn (1992), the meridional circulation increases the thickness of the tachocline in one solar age to $0.2625R_{\odot}$ even in the absence of any turbulence. However, these results are inconsistent with those obtained by helioseismic measurements. This inconsistency is called the "Thin Tachocline Problem". Two possible solutions to this problem have been suggested.

1.1. The possible solutions until now

As a way to resolve this problem, Spiegel & Zahn (1992) suggested the presence of a strongly anisotropic turbulence that could inhibit the spreading of

the tachocline into the radiative region of the Sun. In his numerical models, Elliott (1997) found that the thickness of the tachocline was reduced to approximately $0.1R_\odot$ with a horizontal turbulent viscosity of 5×10^4 cm^2/s and a ratio $\nu_H/\nu_V = 1000$. This explanation of the problem is, however, somewhat dubious, as such a strongly anisotropic turbulence has never been measured, either in laboratory or in nature.

Rüdiger & Kitchatinov (1997) suggested that an internal magnetic field is able to produce a thin tachocline. They argue that a weak poloidal field may well have survived in the radiative interior against the Ohmic dissipation. The differential rotation winds up this poloidal field to produce a toroidal field. Latitudinal angular momentum transport by the Maxwell stresses suppresses the differential rotation and restricts its penetration into the radiative interior to a short distance. The initial poloidal field amplitude, in their model $B_0 = 10^{-4}$ Gauss, determines the thickness of the tachocline and the amplitude of the toroidal field ($B \simeq 200$ Gauss) produced by the differential rotation.The magnetic field in the model of Rüdiger & Kitchatinov (1997) is capable of producing a thin tachocline; however, it is open to question whether the Sun does have an internal magnetic field.

1.2. The present model

In this paper we explore a third possibility for the explanation of the thin tachocline. It is known that the differential rotation in the convection zone is produced by the so-called Λ-effect which consists in the appearance of non-diagonal components in the Reynolds stress tensor as a result of the influence of rotation on turbulence. If turbulence penetrates into the stably stratified layers below the convection zone the possibility exists that a Λ-effect of the opposite sense may arise. (Cf. the formulae for Λ given by Kitchatinov & Rüdiger 1993.) Thus, in the present work we assumed that such an inverse Λ-effect contributes to the horizontal angular momentum transport below the convection zone, treating its amplitude as a free parameter. Section 2 presents the model and in Section 3 we describe and discuss the results.

2. Our model

2.1. Equations

The azimuthal component of the equation of motion in a frame rotating with an angular rate Ω, assuming axial symmetry, reads

$$\partial_t v_\phi = -C + \frac{\tau_{r\phi}}{r\rho} + \frac{\tau_{\theta\phi}\cot\theta}{r\rho} + \frac{1}{r\rho\sin\theta}\left[\frac{\sin\theta}{r}\partial_r(r^2\tau_{\phi r}) + \partial_\theta(\tau_{\phi\theta}\sin\theta)\right], \tag{1}$$

where ρ is the density, v_ϕ is the azimuthal component of the velocity and $\| \tau \|$ is the stress tensor (cf. Tassoul 1978). The terms on the r.h.s. represent three main effects: meridional circulation (Eddington-Sweet circulation) which is denoted by C, diffusion and Λ-effect.

Spiegel & Zahn (1992) showed, that in the limit of a thin tachocline the meridional circulation can be described by a fourth-order diffusion or "hyperdiffusion". We assume that this description remains approximately valid also in the case of a thicker tachocline. Thus, we substitute for the circulation term the following expression

$$C = \left\{\nabla \times \left[\nu^{(4)}\nabla \times (\Delta \mathbf{v})_\phi\right]\right\}_\phi, \qquad \nu^{(4)} = \frac{\chi}{\rho C_p}\left(\frac{2\Omega}{N}\right)^2\left(\frac{r_0}{\alpha}\right)^2, \tag{2}$$

where $\nu^{(4)}$ is called hyperviscosity and according to Spiegel & Zahn (1992), χ is the thermal conductivity, C_p is the specific heat at constant pressure, $N^2 = (g/H_P)(\nabla_{ad} - \nabla)$ (with the usual notation for the pressure scale-height at the base of the convection zone H_P, for the logarithmic temperature gradients $\nabla = \partial \ln T/\partial \ln P$ and for the acceleration due to gravity g), $r_0 = 0.7R_\odot$ and $\alpha = 3.5$. As we do not explicitly model meridional circulation we set $v_r = 0, v_\theta = 0$, while v_ϕ reads $v_\phi = \omega(r,\theta,t)r\sin\theta$, where $\omega(r,\theta,t)$ is the angular rotation rate in the rotating frame. The components of the stress tensor appearing in Eq.1 are

$$\tau_{\theta\phi} = \tau_{\phi\theta} = \rho\nu^{(2)}\frac{\sin\theta}{r}\partial_\theta\left(\frac{v_\phi}{\sin\theta}\right) + \Lambda_{\theta\phi} \tag{3}$$

$$\tau_{\phi r} = \tau_{r\phi} = \rho\nu^{(2)}r\partial_r\left(\frac{v_\phi}{r}\right), \tag{4}$$

where $\nu^{(2)}$ is the coefficient of kinematical viscosity. It is apparent that beside the standard expression for the viscous stress tensor (Tassoul, 1978) these expressions include the additional term $\Lambda_{\theta\phi}$, meant to describe the inverse Λ-effect

mentioned in Section 1.2. Following standard notation we write this term in the form

$$\Lambda_{\theta\phi} = H^{(1)} \sin^2\theta \cos\theta, \tag{5}$$

where $H^{(1)}$ is a function of r only.

2.2. Boundary conditions

We use the same boundary conditions as those in Elliott (1997). We suppose that the rotation rate at the base of convection zone can be described with the same expression as in the upper part of the convection zone. According to the observations of the GONG network (Thompson et al., 1998) the following expression is given for $\Omega_{\rm bcz}$:

$$\frac{\Omega_{\rm bcz}}{2\pi} = 456 - 72\cos^2\theta - 42\cos^4\theta \ \text{nHz}. \tag{6}$$

This is used to give the outer boundary condition on ω,

$$\Omega + \omega = \Omega_{\rm bcz} \quad at\ r = r_{\rm bcz}. \tag{7}$$

Ω is chosen as the rotation rate in the radiative interior below the tachocline. On the basis of helioseismic measurements, this value is equal to the rotation rate of the convection zone at a latitude of about 30°, corresponding to $\Omega/2\pi \approx 437$ nHz.
The second outer boundary condition is given as the observations indicate that the differential rotation varies little in the deep convection zone,

$$\frac{\partial\omega}{\partial r} = 0 \quad at\ r = r_{\rm bcz}. \tag{8}$$

The last two boundary conditions,

$$\omega = \frac{\partial\omega}{\partial r} = 0 \tag{9}$$

are imposed at the inner edge of our region.

2.3. Numerical method

We used a time relaxation method with a finite difference scheme first order accurate in time to solve the fourth-order partial differential equation.

In our model the dimensionless function $H^{(1)}$, playing part in the Λ-effect is chosen in this way: $H^{(1)} = \Lambda_0 f(r)\rho(r)v_{\text{turb}}^2$, where Λ_0 is a constant, v_{turb} is the root mean square turbulent velocity at the base of the convection zone ($v_{\text{turb}} = 5 \cdot 10^3 \text{cm/s}$). Finally, $f(r)$ is a Gaussian function that represents the gradual decay of turbulence caused by penetrating convection below the convectively unstable layer. The kinematical viscosity is similarly given as $\nu^{(2)} = H_P f(r) v_{\text{turb}}$.

The stability of this explicit time evolution scheme is determined by the condition

$$\Delta t_{\text{hypdiff}} < \frac{\Delta r^4}{2\nu_{\text{max}}^{(4)}} \qquad \Delta t_{\text{diff}} < \frac{\Delta r^2}{2\nu_{\text{max}}^{(2)}}, \tag{10}$$

where $\Delta t_{\text{hypdiff}}$ is the time step for the meridional circulation, Δt_{diff} is the time step for the diffusion, $\nu_{\text{max}}^{(2)}$ is the maximum value of the kinematical viscosity and $\nu_{\text{max}}^{(4)}$ is the maximum value of the hyperviscosity. A problem arises because the more rigorous of the conditions (10) imposes a very short timestep Δt_{diff}, making it impossible to follow the evolution for one solar age. To circumvent this difficulty we use a relaxation scheme with alternating diffusive and non-diffusive relaxation phases. In this manner, the evolution could be followed for one solar age, while still maintaining the effects of turbulent diffusion.
In our calculation we used the solar model of Guenther (1992).

3. Results and discussion

We examined the influence of the inverse Λ-effect on the radial spreading of the differential rotation. The results of the numerical calculation are shown in Fig.1 for different amplitudes of the inverse Λ-effect, Λ_0. In Fig.1(a) $\Lambda_0 = 1.0000$ and the numerical calculation shows that the differential rotation extends into the deep layers of the radiative interior, indicating a thick tachocline. In Fig.1(b) $\Lambda_0 = 60000.0$, clearly, the higher the amplitude of the inverse Λ-effect, the lower the depth of the penetration of the differential rotation into the transition layer. This illustrates that the only possibility to reduce the thickness of the tachocline is to assume a very effective horizontal angular momentum transport in the direction of the pole. Our results indicate that an inverse Λ-effect can only provide such transport with an unrealistically high amplitude. Thus, our results practically exclude the possibility that the thin tachocline is a consequence of a inverse Λ-effect.

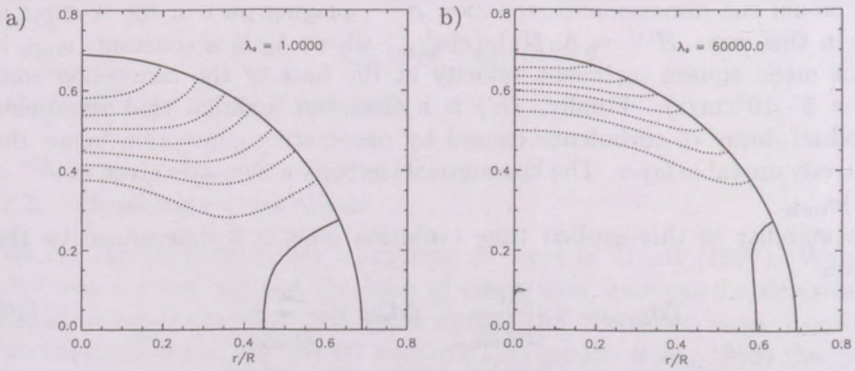

Figure 1: Spreading of the differential rotation into the radiative interior in one solar age. The lines show the contours of the angular rotation rate $\omega(r, \theta, t)$ allowing for the Λ-effect.The amplitude of inverse Λ-effect, in the case (a) Λ_0 is 1.0000 and in the case (b) Λ_0 is 60000.0.

Acknowledgments

We thank D.B. Guenther for making his solar model available. This work was funded by the FKFP project no. 0201/97, and the OTKA project no. T032462.

References

Elliott J.R., 1997, A&A 327, 1222

Guenther D.B., Demarque P., Kim Y.-C., Pinsonneault M.H. 1992, ApJ 387, 372

Kitchatinov L.L., Rüdiger G., 1993, A&A 276, 96

Kosovichev A.G., 1996, ApJ 469, L61

Rüdiger G., Kitchatinov L.L., 1997, Astron. Nachr. 318, 273

Schou J., Antia H.M., Basu S., et al., 1998, ApJ 505, 390

Spiegel E.A., Zahn J.-P., 1992, A&A 265, 106

Tassoul J.-L., 1978, Theory of rotating stars , Princeton Univ. Press

Thompson M.J., Toomre J., The Gong Dynamics Inversion Team, 1996, Sci 272, 1300

Numerical modell for the lower overshoot layer of the Sun

Dániel Marik
Eötvös Loránd University, Department of Astronomy
H-1518 Budapest, P.O.Box 32., Hungary
E-mail: dmarik@astro.elte.hu

Abstract

The lower overshooting layer, which plays an important role in the dynamo mechanism, is one of the least known regions of the Sun. The most promising way to model this region is the Reynolds-stress method. In this paper we determine the radial distribution of the turbulent kinetic energy k, the mean square relative temperature fluctuation q, the normalized energy flux J, and the energy dissipation rate ε. We present solutions using various $\Delta\nabla$ distributions (temperature stratifications). We use a diffusive approximation for the nonlocal fluxes ("Xiong's closure"), considering the cases of both strong and weak non-locality. The resulting profiles of k and ε are found to be approximately linear and the profiles of the turbulent length and time scales l and τ are also similar for different cases. The shapes of these profiles thus seem to be robust properties of the solution, with little sensitivity to the particular parameter values and background stratification assumed. In contrast, we find that the penetration depth depends rather sensitively on the slope of the $\Delta\nabla$ curve and on the strength of nonlocality assumed.
KEYWORDS: *Sun: interior, overshooting, turbulence*

1. Introduction

According to our ideas, the lower overshooting layer, situated under the convective zone of the Sun, plays an important role in the dynamo mechanism which maintains the general solar magnetic field. In spite of this fact this layer is one of the least known regions of the Sun; we have no reliable models for this layer until today. A few years ago it turned out that the models based

on non-local mixing length theories are in unambiguous contradiction with the helioseismological data. The numerical simulations are unable reproduce the detailed structure of the overshooting layer yet.

Under the given circumstances, the most promising way to model the overshooting layer is the Reynolds-stress method. It is based on the well known Reynolds-momentum hierarchy of the hydrodynamical equations for a turbulent medium. In the spherical stationary case this leads to a system of ordinary differential equations having various order moments of the fluctuations as dependent variables. To solve the equations we need a closure assumption that makes it possible to express the highest order moments with the lower order moments in this problem; futhermore we need some other assumptions that can simplify the structure of the equations.

The Reynolds-stress equations for k, q and J were solved for the lower overshoot layer by Unno, Kondo and Xiong (1985), and by Unno and Kondo (1989). However, in that calculation l was treated as a free parameter, arbitrarily set to be equal to the pressure scale height. The use of an equation for ε to get rid of the free parameter was suggested e.g. by Canuto (1993) and it has been applied in a simplified k–ε model by Petrovay (1998).

In this article we present for the first time a solution of the full coupled system of equations for the four variables mentioned above for an astrophysically relevant case. These results are preliminary: the arbitrary prescribed thermal stratification approximates the real solar stratification only crudely and no attempt is made to make the model self-consistent by assuring constancy of the energy flux. Our aim here is just a first exploration of the effect of including the ε equation. This equation considerably modifies the solution.

1.1. The equations and closures

We will use the following notations: P, T and ϱ denote pressure, temperature and density, $\nabla = d\ln P/d\ln T$, $\nabla_{ad} = (\partial \ln P/\partial \ln T)_S$, $\Delta\nabla = \nabla - \nabla_{ad}$ as usual. Any variable f is split into a mean and a fluctuating part as $f = \overline{f} + f'$. The velocity $\mathbf{v}$ has only a fluctuating part. We assume plane parallel geometry and the depth z is measured from $\Delta\nabla = 0$, so the gravity acceleration is positive, ($g = -g_z$ is negative). We also introduce the notations $q = \overline{(T'/T)^2}$, $J = \overline{w(T'/T)}$, $w = v_z$, $k = \overline{v^2}/2 = \overline{w^2}/f_a$ where f_a is an anisotropy parameter.

We make the following assumptions:

- $\varrho'/\varrho \ll 1$
- The Reynolds number $Re \gg 1$
- The extent of the overshoot layer $d \ll H_P$, where H_P is the pressure scale height at $z = 0$.

With these assumptions we can use the Boussinesq approximation $\varrho'/\varrho = -\delta_P(T'/T)$ where δ_P is an order of unity factor ($\delta_P = 1$ for full ionization). Following standard practice, we will also neglect the $\overline{\mathbf{v}\nabla P'}$ term in the equation for k.

The detailed derivation of the Reynolds momentum equations was given by many authors (Xiong 1978; Canuto 1992; Grossman 1996). With the assumptions and notations mentioned above they read

$$\partial_t k = -\partial_z F_k + \delta_p g J - \varepsilon \tag{1}$$

$$\partial_t J = -\partial_z F_J - C_{qJ}\delta_p g q + C_{kJ} f_a \frac{\Delta\nabla}{H_P} k - C_J \frac{\varepsilon}{k} J \tag{2}$$

$$\partial_t q = -\partial_z F_q + 2\frac{\Delta\nabla}{H_P} J - C_q \frac{\varepsilon}{k} q \tag{3}$$

$$\partial_t \varepsilon = -\partial_z F_\varepsilon + C_{J\varepsilon}\delta_p g \frac{\varepsilon}{k} J - C_\varepsilon \frac{\varepsilon^2}{k} \tag{4}$$

where the non-local fluxes are

$$\begin{aligned} F_k &= \overline{wv^2/2}, & F_q &= \overline{w(T'/T)^2} \\ F_J &= \overline{w^2 T'/T}, & F_\varepsilon &= \overline{w\varepsilon_l} \end{aligned} \tag{5}$$

where ε_l is the local dissipation rate. In order to close the system we need a closure that expresses the fluxes with k, q, j and ε. For this illustrative calculation we use the simplest closure known as Xiong's closures:

$$F_k = -C_{wk}\frac{k^2}{\varepsilon}\partial_z k \qquad F_q = -C_{wq}\frac{k^2}{\varepsilon}\partial_z q$$

$$F_J = -C_{wJ}\frac{k^2}{\varepsilon}\partial_z J \qquad F_\varepsilon = -C_{w\varepsilon}\frac{k^2}{\varepsilon}\partial_z \varepsilon.$$

In these equations C_{wk}, C_{wJ}, C_{wq}, $C_{w\varepsilon}$, C_{kJ}, C_{qJ}, $C_{J\varepsilon}$, C_ε, C_q, C_J, δ_p and f_a are constants of order unity. Their values can in principle be specified on the basis of turbulence theory.

1.2. Boundary conditions

For the solution of the system we need to specify the boundary conditions. The orders of magnitude of the turbulent velocity and the temperature fluctuations are well known at the bottom of the convective zone ($w \approx 5 \cdot 10^3$ cm/s, $T' \sim 1$ K). This sets the scale for the values of k and q at $z = 0$; their more precise values are set taking into account the requirement that in the total convective flux in the unstable layer must be equal to the solar flux (as the radiative flux is known to be negligible there). In addition, in the unstable region a good correlation of temperature and velocity fluctuations can be assumed: $J = (f_a kq)^{1/2}$. Finally, in the convectively unstable region the assumption $l = H_P$ is known to be safe, so from $\varepsilon = \overline{w^2}^{3/2}/l$ we can get the initial value of the energy dissipation (ε).

1.3. Results and discussion

We have used a time relaxation method to solve the nonlinear, coupled system of differential equations. We use various profiles for $\Delta\nabla$. In our reference model we set $\Delta\nabla = -0.1z/H_P$; this crudely represents the actual run of $\Delta\nabla$ below the convectively unstable layer in standard solar models with no overshoot. Beside the reference model (Fig. 1 a.) we computed several other cases.

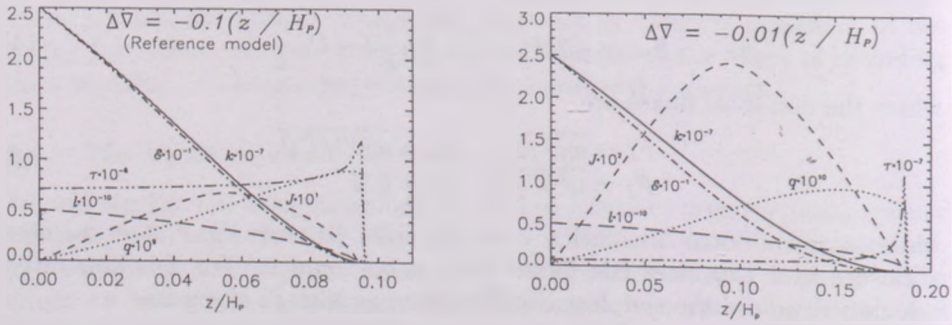

Figure 1: Distribution of the turbulent kinetic energy k (solid line), temperature fluctuation q (dotted line), correlation J (short dashes), energy dissipation rate ε (dot-dashed line), mixing length l (long dashes) and time scale τ (dotted-dashed) in case of linear models assuming strong non-locality ($C_{wi} = 1.0$).

In order to study the sensitivity of the results to the temperature stratification chosen, for comparison we also compute models with linear $\Delta\nabla$ profiles of

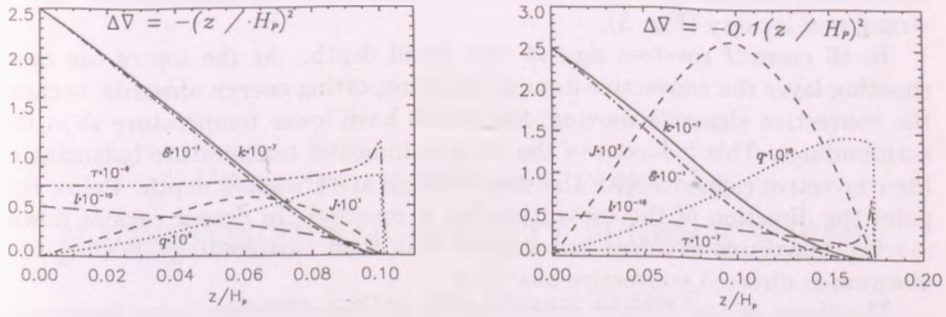

Figure 2: The same as Fig. 1 in case of the parabolic reference model.

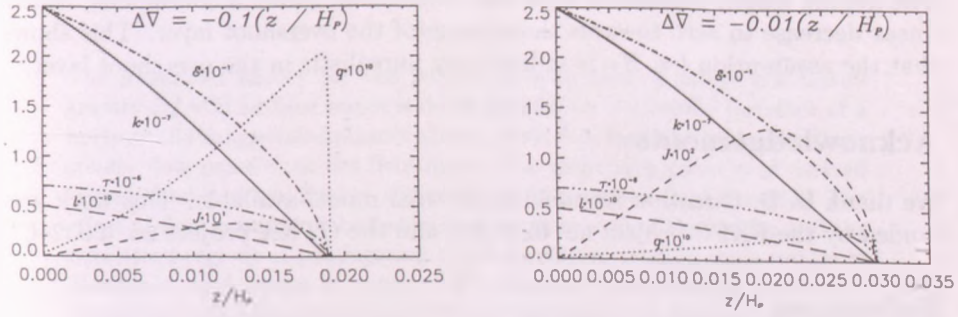

Figure 3: The same as Fig. 1 in case of weak non locality ($C_{wk} = 0.027, C_{wq} = 0.027, C_{wJ} = 0.027, C_{w\varepsilon} = 0.093$).

different steepness (Figs. 1 a.–1 b.), as well as a parabolic profile (Figs. 2 a.–2 b.).

It is apparent that the shapes of the k and ε curves are crudely linear in all cases and there is no considerable difference between the corresponding linear and parabolic solutions (Figs. 1 and 2). Furthermore, the shapes of the appropriate k, ε, l and τ curves are not essentially different for various amplitudes of $\Delta\nabla$ (Figs. 1 a. and b.). On the other hand, there are striking differences in the depth of the overshooting layer in the various cases. Not surprisingly, the penetration depth is decreasing with increasing $\Delta\nabla$ slope, and in case of weak

non-locality we find that the penetration depth is much smaller than in case of strong non-locality (Fig. 3).

In all cases J reverses sign at very small depth. At the top of the overshooting layer the convective flux (F_c) is transporting energy upwards, because the convective elements moving downwards have lower temperature than the surroundings. This behavior of the J-curve indicates temperature balancing of the convective elements with the surroundings at very small depth. Below this point the direction of the convective flux is reversed. In deeper regions downmoving convective elements are warmer than their surroundings, leading to a downwards directed convective heat flux.

The shape of the J-curve shows that in all cases the correlation between w and T'/T is strongest at the middle of the overshooting layer. It is evident that the turbulent time scale τ shows little variation in most of the overshoot layer but it has a (possibly spurious) sharp peak near its bottom (Figs. 1 and 2). The mixing length parameter l, on the other hand, shows a continuous, nearly linear decrease to zero towards the bottom of the overshoot layer. This shows that the assumption $l = H_P$ is indeed very unrealistic in the overshoot layer.

Acknowledgements

We thank D. B. Guenther for making his solar model available. This work was funded by the FKFP project no. 0201/97, and the OTKA project no. T032462.

References

Canuto V. M., 1992, ApJ, 392, 218

Canuto V. M., 1993, ApJ 416, 331

Grossman S. A., 1996, MNRAS 279, 306

Guenther D. B., Demarque P., Kim Y.-C., Pinsonneault M. H. 1992, ApJ, 387, 372

Petrovay K., 1998, in: New Eyes to See inside the Sun and Stars (Deubner F.-L., Christensen-Dalsgaard J., and Kurtz D. eds.), Proc. IAU Symp. 185, 121, Kluwer

Unno W., Kondo M., 1989, PASJ 41, 197

Unno W., Kondo M., Xiong D.-R., 1985, PASJ 37, 235

Xiong D.-R., 1978, Chinese Astron., 2, 118

Xiong D.-R., 1980, Chinese Astron., 4, 234

Effects of steady flow on magnetoacoustic-gravity surface waves

Emese Varga[1] and Róbert Erdélyi[2]
[1]Dept. of Astronomy, Eötvös L. University, H-1518 Budapest, P.O.Box 32., Hungary, E-mail: vemese@innin.elte.hu
[2]Dept. of Applied Mathematics, Univ. of Sheffield, S3 7RH, Sheffield, England (UK), E-mail: robertus@sheffield.ac.uk

Abstract

The linearized theory for the parallel propagation of magnetoacoustic-gravity (MAG) surface waves is developed for an isothermal interface of a horizontally magnetised plasma above a field-free medium with a constant steady flow parallel to the field lines. The dispersion relation is derived and studied in detail for two distributions of magnetic field strength. The effect of flow is found to be twofold: the frequencies of the modes and the permitted regions of propagation are both shifted causing some modes to disappear, and others to appear. The backward propagating slow mode changes its direction of propagation and couples to its forward propagating counterpart.
Keywords: *MHD (surface) waves; steady flow; convective zone; chromosphere*

1. Introduction

The high inhomogeneity of the solar atmosphere caused by the magnetic field and gravity can be modelled as a first approximation by regions separated by tangential surface discontinuities (with different plasma parameters on the two sides) along which MHD surface waves can propagate. In the solar atmosphere surface MHD waves can propagate e.g. along boundaries of sunspots, coronal holes, along the boundary of the photosphere and convection zone and in the canopy regions of the chromosphere. Properties of such waves on a magnetic interface have been intensively studied by Roberts (1981); Campbell & Roberts

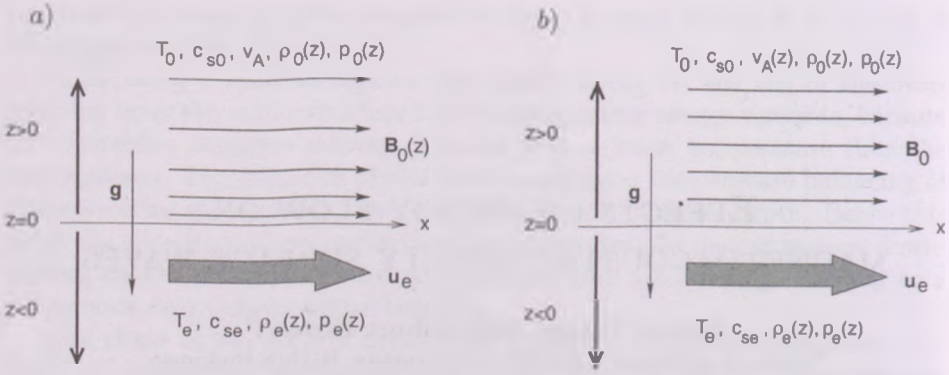

Figure 1: Equilibrium models of a single magnetic interface at $z = 0$ in a stratified atmosphere for *a*) constant Alfvén speed and *b*) constant magnetic field in $z > 0$.

(1989); Miles & Roberts (1992); Miles et al. (1992) etc. A possible application of surface wave theory is the 'running penumbral wave' sunspot phenomenon (Small & Roberts, 1984).

The Sun is also highly dynamical showing large scale equilibrium motions both in the interior (e.g. convective motion) and in the atmosphere (e.g. meridional flows). Large scale motions in the surface and subsurface region influence the MAG surface modes resulting in observable frequency shifts (Braun & Fan, 1998). In the present paper we extend the models of Miles & Roberts (1992) (the *const* v_A model hereafter) and Miles et al. (1992) (the *const* B model hereafter) and examine theoretically the influence of a steady equilibrium flow on MAG surface waves in these models.

2. Dispersion relations

We assume a single magnetic interface located at $z = 0$, in a stratified atmosphere. In the *const* v_A model (Fig. 1a) the upper isothermal (T_0) region ($z > 0$) is permeated by an exponentially decreasing magnetic field $B_0(z)$, resulting in a constant Alfvén speed v_A. The field-free lower region ($z < 0$) is also isothermal though with a different temperature, T_e, having a parallel constant steady flow u_e. Quantities above the interface (in $z > 0$) are denoted by a subscript '0', quantities below (in $z < 0$) by a subscript 'e'.

In compressible ideal MHD two-dimensional, linear, isentropic disturbances about the equilibrium of the form $\mathbf{u}_1(x, z, t) = (\hat{u}_{1x}(z), 0, \hat{u}_{1z}(z)) \exp[i(\omega t - k_x x)]$

are governed by a second order ODE in both regions. Solving these ODE-s with the requirement that the total energy density remains finite as $|z| \to \infty$, and coupling these solutions by the boundary conditions at the magnetic interface $z = 0$ results in the transcendental dispersion relation

$$\frac{\rho_0(c_{s0}^2 + v_A^2)(\omega^2 - k_x^2 c_T^2)}{\omega^2 - k_x^2 c_{s0}^2} \frac{1}{2H_B} \left(\sqrt{1 - 4H_B^2 A_B(\omega, k_x)} - 1 \right) + \frac{g k_x^2 \rho_0 c_{s0}^2}{\omega^2 - k_x^2 c_{s0}^2} =$$
$$= \frac{\rho_e c_{se}^2}{\Omega^2 - k_x^2 c_{se}^2} \left[g k_x^2 - \frac{1}{2H_e} \left(1 + \sqrt{1 - 4H_e^2 A_e(\omega, k_x, u_e)} \right) \Omega^2 \right], \quad (1)$$

where $\rho_0 = \rho_0(0_+)$, $\rho_e = \rho_e(0_-)$, and H_B, H_e are the density scale-heights above and below the interface. $\Omega = \omega - k_x u_e$ is the Doppler shifted frequency.

In the *const B* model (Fig. 1b) the upper isothermal (T_0) region ($z > 0$) is permeated by a uniform magnetic field B_0, resulting in an exponentially increasing Alfvén speed $v_A(z)$. Following the same steps as in the *const* v_A model we get the dispersion relation

$$\frac{\rho_0(c_{s0}^2 + v_A^2)(\omega^2 - k_x^2 c_T^2)}{\omega^2 - k_x^2 c_{s0}^2} \left[k_x + \frac{X_0}{H_0} \frac{pq}{r} \frac{F(p+1, q+1; r+1; X_0)}{F(p, q; r; X_0)} \right] + \quad (2)$$
$$+ \frac{g k_x^2 \rho_0 c_{s0}^2}{\omega^2 - k_x^2 c_{s0}^2} = \frac{\rho_e c_{se}^2}{\Omega^2 - k_x^2 c_{se}^2} \left[g k_x^2 - \frac{1}{2H_e} \left(1 + \sqrt{1 - 4H_e^2 A_e(\omega, k_x, u_e)} \right) \Omega^2 \right],$$

where $v_A = v_A(0_+)$ and H_0, H_e are the density scale-heights. $F(p, q; r; X)$ is the hypergeometric function.

3. Numerical results

The dispersion relations Eq. (1) and Eq. (2) are solved numerically subject to the requirement to get surface wave solutions (i.e. evanescent modes in the z direction). This gives rise to the constraints $(1 - 4A_B H_B^2) > 0$ and $(1 - 4A_e H_e^2) > 0$, and results in the cutoff curves $R_1 - R_6$ for the *const* v_A model. In the *const B* model the surface wave constraint is $(1 - 4A_e H_e^2) > 0$ yielding the cutoff curves $R_1 - R_4$.

In Fig. 2 solutions of the *const* v_A model are plotted. The permitted regions of propagation are shaded grey. Dark regions contain modes with exponentially increasing velocity amplitude as $z \to +\infty$. The limit $k_x H_e \to \infty$ is equivalent to $g \to 0$, therefore asymptotes of MAG surface modes can be obtained from the non-gravity dispersion relation. In the $g = 0$, $u_e = 0$ case one or two MA surface modes can propagate: whereas the slow mode is always present, the

fast mode appears only when both $v_A > c_{s0}$ and $c_{se} > c_{s0}$ (Roberts , 1981). Fig. 2a corresponds to $u_e = 0$ and asymptotically only the slow wave appears (elsewhere it is modified by gravity). The other mode in the dark region is the *f-mode* modified by the magnetic field. Modes with negative phase speeds correspond to waves propagating in the opposite direction. In the zero-flow case forward (positive phase speed) and backward (negative phase speed) propagating waves are equivalent. As the flow increases (Figs. 2b,c) the permitted regions and the modes are shifted upward. The *f-mode* disappears, meanwhile the two slow modes approach each other: the backward propagating slow mode shifts together with the flow, changes its direction of propagation (Fig. 2b) and finally reaches and couples to the other slow mode (on which the effect of flow is negligible). The coupled slow modes form two branches and the gap between them keeps expanding with growing flow (Fig. 2c).

Fig. 3 shows solutions for the *const B* model. The regions of propagation are shaded grey. With the given parameter set only the slow mode can propagate in the absence of flow (Fig. 3a). Like in the previous case as the flow increases (Figs. 3b,c) the two slow modes aproach and couple to each other but here the upper branch of the modes is missing (no asymptotic solutions exist any more) giving rise to an upper bound of the permitted wavenumber range for propagation (Fig. 3c). Note that as the cutoff curves shift upward a new permitted region with harmonic modes appears (Fig. 3b). These are trapped modes and their existence can be traced back to the refraction caused by the increasing Alfvén speed with height into the atmosphere.

Further studies concerning solar applications of the models are in progress.

Acknowledgements

This work was funded by the OTKA project no. T032462. EV is grateful to ELTE Peregrinatio II for their financial support when visiting SPARC, Dept. of Appl. Math., Univ. of Sheffield. EV wishes to express her thanks to M. Zétényi for technical help.

References

Braun, D. C. and Fan, Y.: 1998, ApJ. **508**, L105.

Campbell, W. R. and Roberts, B.: 1989, ApJ. **338**, 538.

Miles, A. J. and Roberts, B.: 1992, Solar Phys. **141**, 205.

Miles, A. J., Allen, H. R. and Roberts, B.: 1992, Solar Phys. **141**, 235.

Roberts, B.: 1981, Solar Phys. **69**, 27.

Small, L. M. and Roberts, B.: 1984, in *The Hydromagnetics of the Sun*, ESA SP-220

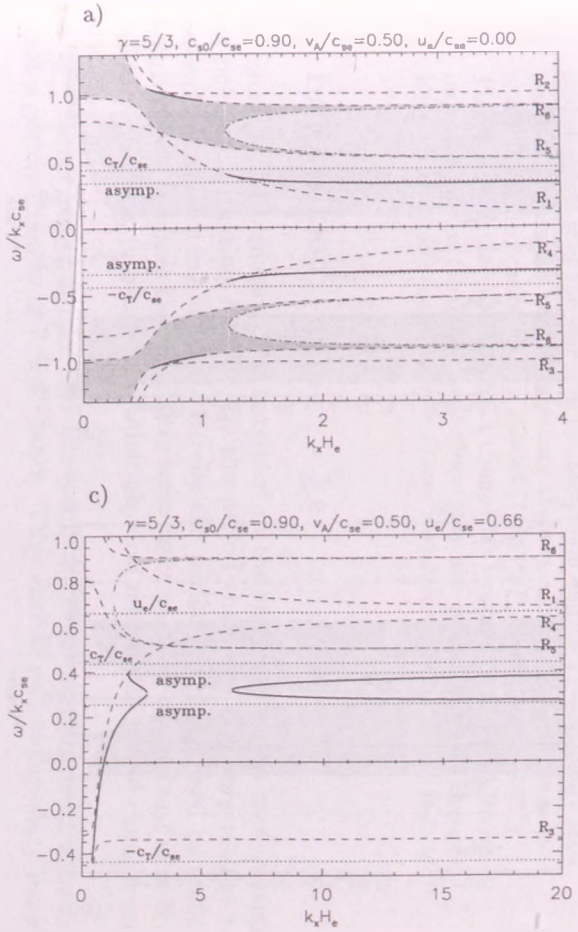

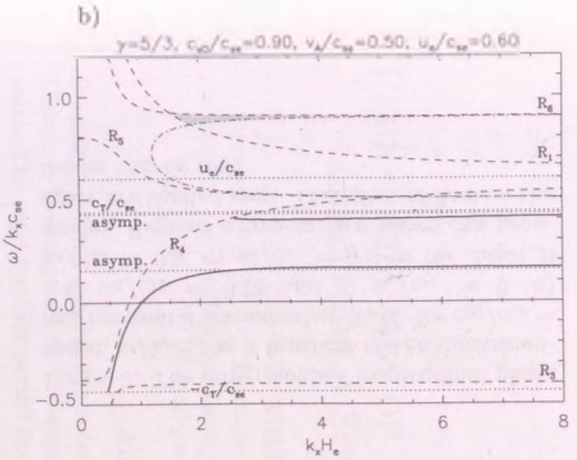

Figure 2: The dimensionless longitudinal phase speed, $\omega/k_x c_{se}$ as a function of the dimensionless horizontal wavenumber, $k_x H_e$ for $c_{s0}/c_{se} = 0.9$, $v_A/c_{se} = 0.5$ and a) $u_e/c_{se} = 0$, b) $u_e/c_{se} = 0.6$, c) $u_e/c_{se} = 0.66$ in the *const* v_A model. The permitted regions of propagation for surface modes are shaded grey. Dark regions contain modes with growing velocity amplitude as $z \to +\infty$. The effect of flow on the modes can be seen.

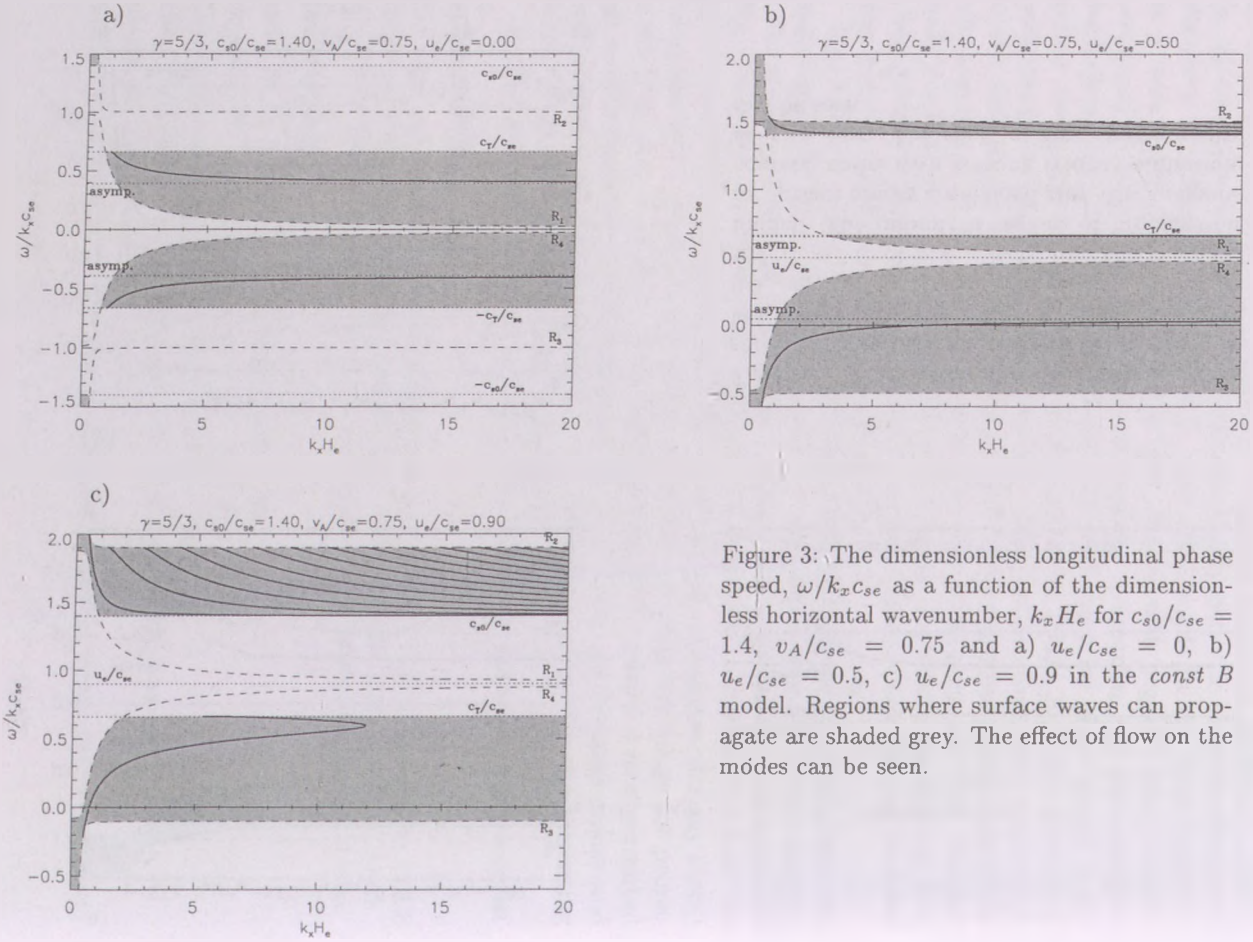

Figure 3: The dimensionless longitudinal phase speed, $\omega/k_x c_{se}$ as a function of the dimensionless horizontal wavenumber, $k_x H_e$ for $c_{s0}/c_{se} = 1.4$, $v_A/c_{se} = 0.75$ and a) $u_e/c_{se} = 0$, b) $u_e/c_{se} = 0.5$, c) $u_e/c_{se} = 0.9$ in the *const B* model. Regions where surface waves can propagate are shaded grey. The effect of flow on the modes can be seen.

Period changes of the double mode high amplitude δ Scuti star AE UMa

Miklós Pócs
Konkoly Observatory
H-1525 Budapest, P.O.Box 67., Hungary
E-mail:pocs@konkoly.hu

Abstract

Stability of both the fundamental and first overtone oscillations of AE UMa was investigated by different methods which led to concordant results. The reported fast period decrease (Hintz et al., 1997) proved to be incorrect, the fundamental period of AE UMa has been essentially constant in the past 60 years in accordance with the theoretical expectation (Breger and Pamyatnykh, 1998). The constancy of the fundamental period suggests that the star is in the post-main sequence evolutionary state in accordance with the evolutionary theories. The first overtone period is definitely decreasing with a rate of $(1/P_1)(\mathrm{d}P_1/\mathrm{d}t) = -7.3 \times 10^{-8}\mathrm{y}^{-1}$. The fact that the rate of period change for two modes is quite different indicates that non-evolutionary effects may also generate period changes.
Keywords: *Stars: oscillation – Stars: variables: δ Sct – Stars: individual: AE UMa*

1. Introduction

The period of a pulsating star is related to the structure of the star through the pulsation equation $P\sqrt{\varrho} = Q$, the period change is therefore related to the evolutionary radius change. Hereby the period changes caused by stellar evolution in and across the instability strip make an observational test of stellar evolution possible, provided that other physical reasons for period changes can be excluded.

In a recent paper Breger and Pamyatnykh (1998) investigated the evolutionary period changes of δ Scuti stars. They carried out evolutionary model

calculations both with and without convective core overshooting and compared the computed values of period changes with the observed ones. Although their results suggest that the observed changes in the periods cannot be fully explained by evolutionary effects, the very fast measured period change of AE UMa (-5×10^{-7} year^{-1}, Hintz et al. (1997)) proved to be a challenge. The rate of its period decrease fitted into Breger and Pamyatnykh's (1998) pre-MS models, they however, rejected this assumption in lack of evidence (but its possibility could not be precluded).

Since the accurate photoelectric and CCD maxima of the light variation of AE UMa were scarce and large gaps occurred between the groups of published maxima, we suspected that the epoch numbers might be miscounted in calculating the rate of its period change. Therefore we decided to reanalyze all the available observations.

The investigation of period changes of AE UMa may result in an interesting inference about the evolutionary effects. The star is a well-known double-mode pulsator, it oscillates radially both in the fundamental and the first overtone modes. If the changes in the frequencies are constant or parallel and slowly decreasing, we have good reason to assume that they are essentially of evolutionary origin. On the other hand, if the changes in the periods of the two radial modes have different signs, then certainly non-evolutionary physical effects should play an important part in the frequency variations.

2. AE UMa and its observations

The variability of AE UMa (BV92, HIP047181, $\alpha_{2000} = 09^{\mathrm{h}}36^{\mathrm{m}}53^{\mathrm{s}}, \delta_{2000} = +44°04'.0$) was discovered by Geyer et al. (1955) on Bamberg plates. Tsesevich (1973) and Filatov (1960) observed the star, but could not determine the type of variability. (Tsesevich suggested an RR Lyrae type while Filatov a Cepheid type variability).

Tsesevich observed the star again visually and measured the star's brightness on old Moscow and Odessa archive photographic plates (Tsesevich, 1973) and determined the period of the light variation and the type of the variability as dwarf Cepheid. Tsesevich (1973) also showed that the star had significant light-curve variation. This fact aroused Broglia and Conconi's (1975) and my interest and the star was then extensively observed at both the Merate and Konkoly observatories.

Later Rodríguez et al. (1992) observed the star in the Strömgren photometric system. AE UMa was also a program star of the Hipparcos project (ESA, 1997)

and 112 photometric observations were published.

Recently Hintz et al. (1997) investigated the star in more details and published ten new accurate times of maximum light from CCD photometry. Several times of maximum light were reported by the BAV group: Braune et al. (1979), Braune and Mundry (1982); Huebscher et al. (1985), Huebscher et al. (1992); Agerer et al. (1999).

The published data are well-supplemented by the times of maximum light obtained from the Konkoly photometry, and 69 new times of maximum light are added to the 59 epochs of maximum light published up to the present. The whole list of the times of maximum light is published in the paper of Pócs and Szeidl (2001).

3. The Analysis

3.1. The Fourier Analysis

The investigation of the stability of the pulsation of a star can be approached in different ways. One of the methods most commonly used is the Fourier analysis of the observations obtained at different seasons and the study of the variations in the frequencies and the Fourier parameters may provide useful information.

The distribution of the observations of AE UMa was uneven, therefore we divided the data into five separated sets and each set contained observations of several years.

The multifrequency analysis was performed with the *MUFRAN* (*MUltiFRequency ANalysis*) program package (Kolláth, 1990). *MUFRAN* is a collection of methods for period determination, sine fitting for observational data and graphics routines for visualization of the results.

The first step in the analysis was to find the frequencies of the fundamental (f_0) and first overtone (f_1) pulsation for each data set. The results are presented in Table 1. The frequencies (except for the fourth set) are the mean values obtained from the yellow and blue observations. It is interesting to note that the Hipparcos data have not provided a definite value of the overtone frequency. The errors have been estimated using the criterion that one standard error in the frequency should give a difference of not more than 0.02 in phase for the extreme time intervals.

The results clearly show that the frequencies were subject only to small changes during a time base of 25 years.

Table 1: Frequencies for different segments of observations

Years	f_0	f_1
1974–1977	11.62558	15.03120
(B,V)	2	2
1981–1983	11.62560	15.03123
(B,V)	2	2
1986–1987	11.62556	15.03121
$(B,V\&\ b,v)$	3	3
1989–1993	11.62560	—
(HIP)	2	
1996–1998	11.62560	15.03125
(B,V)	2	2

3.2. The $O-C$ Diagram

The Fourier analysis has the definite advantage that all the photometric observations are included into the frequency analysis. However, it often happens that the observations are not available, only the times of observed maxima are published. In this case the construction of the $O-C$ diagram may furnish the dominant frequency with better accuracy.

The $O-C$ values obtained from the photoelectric and CCD observation were fitted by a quadratic polynomial and the least squares solution resulted in the following formula (n=112 maxima, time interval 24 years):

$$O-C = (-2.5 \pm 3.0) \times 10^{-4} + (0.62 \pm 1.90) \times 10^{-8} \times E -$$
$$-(0.15 \pm 0.19) \times 10^{-12} \times E^2$$

which indicated that the period of the star was essentially constant in the last quarter of the century. The corrected period is

$$P_0 = 0^{\mathrm{d}}.086017076 \pm (19 \times 10^{-9})$$

, in accord with the results of the Fourier analysis.

If we take into account all the $O-C$ values with the exception of Filatov's data (124 maxima, time interval 61 years) we arrive at the quadratic polynomial fit:

$$O - C = (2.2 \pm 2.6) \times 10^{-4} - (1.71 \pm 0.53) \times 10^{-8} \times E$$
$$+(0.053 \pm 0.053) \times 10^{-12} \times E^2$$

which also favours a constant period over a time interval of more than half a century.

If the distribution of the times of maxima in the modulation cycles is not uniform, it may falsify the value of both the linear and quadratic term (e.g. most of the maxima observed in 1997 and 1998 happened to be in the phase interval of the modulation cycle where the maxima came earlier than the mean epoch or the deviation of Tsesevich's early epoch from the mean value may have a strong influence over the parameters of the fit).

3.3. The Fourier Phase Diagram

The Fourier phase method renders the most reliable determination of the frequencies of a double mode pulsating star possibly. The idea of the method is that if we fix the amplitudes and frequencies in the Fourier decomposition, then the variations in the $\varphi_{1,0}$ and $\varphi_{0,1}$ phases reflect the changes in the fundamental and first overtone frequencies. The advantage of the method is that the reduced number of free parameters makes the use of short segments of observations also possible. Test runs showed that small changes in the amplitudes did not affect the determination of the phases significantly and the zero point differences could easily be taken into account by leaving a_0 as free parameter as well.

The Fourier phase diagram method gives for both frequencies of AE UMa the following periods:

$$P_0 = (0.086017058 \pm 15 \times 10^{-9}) + (3 \pm 3) \times 10^{-12}(t - T_0),$$

$$P_1 = (0.066528358 \pm 35 \times 10^{-9}) - (1.3 \pm 0.9) \times 10^{-11}(t - T_0).$$

Hence the fundamental mode period is basically constant and the first overtone period is definitely decreasing.

4. Discussion

The stability of the fundamental and first overtone frequencies have been investigated by different methods in the previous section which led inevitably to the conclusion that the fundamental oscillation is very stable and the rate

of its change is less than the error of its determination. The essentially constant fundamental period suggests that AE UMa is in the post-main sequence evolutionary state.

On the other hand the investigations show that the first overtone period is definitely decreasing with a rate of $(1/P_1)(\mathrm{d}P_1/\mathrm{d}t) = -2.0 \times 10^{-10}\mathrm{d}^{-1} = -7.3 \times 10^{-8}\mathrm{y}^{-1}$. Although the constant fundamental period is in accordance with evolutionary theories (Breger and Pamyatnykh, 1998), the changes in the first overtone period cannot be explained by evolution at the same time.

References

Agerer, F., Dahm, M. Huebscher, J., 1999, IBVS No. 4712

Braune, W., Huebscher, J., Mundry, E., 1979, Astron. Nachr. 300, 165

Braune, W., Mundry, E., 1982, BAV Mitt. Nr. 34

Breger, M., Pamyatnykh, A. A., 1998, A&A 332, 958

Broglia, P. Conconi, P., 1975, A&AS 22, 243

ESA, 1997, The Hipparchos and Tycho Catalog, ESA SP-1200

Filatov, G. S., 1960, Astron. Tsirk. No. 215

Geyer, E., Kippenhahn, R., Strohmeier, W., 1955, Kl. Veröff. Bamberg No. 11

Hintz, E. G., Hintz, M. L., Jones, M. D., 1997, PASP 109, 1073

Huebscher, J., Agerer, F., Mundry, E., 1992, BAV Mitt. Nr. 60

Huebscher, J., Lichtenknecker, D., Mundry, E., 1985, BAV Mitt. Nr. 39

Kolláth, Z., 1990, Occasional Technical Notes, Konkoly Obs. No. 1

Pócs, M., Szeidl, B., 2001, A&A accepted

Rodríguez, E., Rolland, A., López de Coca, P., Garcí-Lobo, E., Sedano, J. L., 1992, A&AS 93, 189

Tsesevich, V. P., 1956, Astron. Tsirk. No. 170

Tsesevich, V. P., 1973, Astron. Tsirk. No. 775

Numerical Modelling of SN Type II

Zsolt Regály
Institute for Theoretical Physics, Eötvös Loránd University
H-1117 Budapest, Pázmány Péter s. 1, Hungary
E-mail: regaly@matrix.elte.hu

Abstract

The supernova explosion of type II is a collapse of a massive $M_* > 8M_\odot$ star which becomes hydrodynamically unstable by the exhaustion of its nuclear fuel. According the studies has been developed today, there are some unresolved problems in this phenomena. One of them is that, what kind of nuclear equation of state characterises well the matter of the collapsing core. In SN II numerical simulations we try to solve the classical hydrodynamical differential equations of a perfect fluid among very cruel conditions (shock waves appears etc.). In this paper I would like to show a development of a very simple model of the collapse of a massive star in one and two dimensional spherical geometry established to examine the raise of the core bounce and the growth of perturbation in two dimension before the bounce occurs.
Keywords: *supernovae: general — hydrodynamics*

1. Introduction

The stars receive the essential energy to stay thermodynamical and hydrodynamical stability by burning their nuclear fuels. The energy producing nuclear reaction leads to the production of the heavy elements. When the liberation of energy is cancelled, the hydrodynamical stability of the star will over turn, and the star will finish its life in a different way depending on its initial mass.

At the end of its life the massive ($M_* > 8M_\odot$) stars will perish by a supernova explosion of type II (SN II hereafter). Even the degenerate matter of the Fe-core of a massive star can not produce enough pressure to avoid the collapse, while degenerate carbon-oxygen core of the lighter star can maintain hydrodynamically stable configuration, a so-called white dwarf star.

The collapse of the progenitor of a SN II is governed by the pressure of relativistic degenerate electron gas at the beginning, and by the nuclear matter later. It is a very interesting question, what kind of the nature has the nuclear forces above nuclear density. The equation of state (EOS hereafter) of the nuclear matter determines the explosion energy, via the mass of the proto-neutron star , which can be studied by a simple one dimensional model. The recent numerical SN II models showed that, the neutrino-heating process is not enough, and an additional, energy transporting convection process needs to get successful explosion. In two dimensional simulations we can explore the evolution of initial perturbations before the bounce occurs, which asymmetry in infall caused by this perturbation is indispensable for the formation of convection flows.

In §2, I give a short phenomenological description of the major process which occurs in SN II explosion. In §3, I show a simple hydrodynamical model for the early time evolution of an SN II explosion. Finally in §4 and \$5 the results of one dimensional numerical calculation, and a development of a two dimensional calculation will be shown.

2. SN II Explosion in a Nutshell

The chemical composition, and structure of a star changes continously by the nuclear reactions, which finally leads high abundance of heavy elements in the direction to the centre of the star.

The star will get out of the hydrodynamically stable state by the lack of energy producing nuclear rection. By this time the progenitor of SN II has an onion-shell like structure. All elements produced by fusion reactions (He, C, O, Ne, Mg, Si, S, Fe) has own high abundance shells, and the progenitor has a huge H-mantle.

The matter of the progenitor core is in degenerate state like in white dwarf stars. The $\simeq 1M_{\odot}$ Fe-core with the relativistic degenerate electron gas cannot produce enough pressure to maintain hydrodynamic stability, thus the progenitor begins to collapse.

The pressure of the collapsing core will be determined by the number and the energy of electrons. The temperature is rising by the collapse of core, small fraction of iron nuclei is dissociating, and the particle number of matter of collapsing star is also rising, which should have been caused by the higher pressure. But the dissociation of iron nuclei digests energy, so the energy per one nucleon will be decreasing. Neutrons rise from protons absorbing electrons in process

of $p^+ + e^- \rightarrow n^0 + \nu_e$, which causes the decrease of the number of relativistic electrons, and the pressure of relativistic degenerate electron gas too. In consequence of it the collapse of the progenitor core gathers speed (Bethe, 1990).

The progenitor core is collapsing homogeny, which means that, the shape of density- and velocity-profile stays the same, it is the so-called homolog collapse (Bethe, 1990); (Cooperstein & Baron, 1990).

The collapse will continue until the central density of the star reaches the so called nuclear matter density, $2.7 \cdot 10^{14}\, g/cm^3$. At this point the iron nuclei melt and form symmetric nuclear matter configuration. As soon as the density surpasses a couple of times of this nuclear density, the EOS of nuclear matter become stiff causing the stall of the collapse suddenly. Then pressure waves start outward by the bounce of the core. At the surface of the core the matter will be adiabatically compressed, while in the density- and pressure-profile of the infalling matter will have a tear, namely arise a shock wave (Bethe, 1990).

This prompt shock can propagate outward, while losing its energy. This is because of the shock wave dissociates the iron nuclei, whilst the temperature and the pressure of medium also decreases (Bethe, 1990). According to one dimensional simulations the prompt shock stalls at a distance of $100 - 300Km$ from the centre of the star, depending on the initial mass of the iron core $1.1 - 1.25M_\odot$ (Herant et al., 1994).

The remaining core becomes a hot proto-neutron star, and its pressure is governed by the degenerate leptons fell into a trap. The $\simeq 1M_\odot$ hot proto-neutron star is in a stable configuration and it has $0.15 \cdot 10^{53}\, ergs$ gravitational bounding energy. The proto-neutron star is cooling by neutrino emission, while it is shrinking, until Y_l reaches 0.37. Finally, evolves a cold neutron star having a mass of $\simeq 1.4M_\odot$. The cold neutron star has gravitational bounding energy of $10^{53}\, ergs$ (Colgate & Fryer, 1995).

A delayed shock started by the very weak interaction between the matter of stalled shock and neutrinos raising from the lepton-trapped neutron star. This process is called neutrino-heating. We can say that the energy difference in gravitational bounding energy of the hot lepton trapped and the cold deleptonized neutron star, in form of neutrinos, will reignite the explosion (Cooperstein & Baron, 1990); (Colgate & Fryer, 1995).

Note that, in one dimensional simulations have been carried yet, this neutrino-heating not always have caused a successful explosion. It is possible that some kind of convection process can help the successful explosion (Bethe, 1990); (Herant et al., 1994).

The neutrinos heat up and increase the entropy of matter next to the neutron star, while the entropy of the infalling matter is low, therefore the entropy

gradient will satisfy the convection criteria. The convection cells form so that the infalling low entropy matter reaches the surface of neutron star through the high entropy bubbles of flowing out matter. The hot bubbles reach the accretion shock passes energy to it, which can reignites the explosion (Colgate & Fryer, 1995); (Herant et al., 1994).

3. Hydrodynamical Model of the SN II Explosion

The essential behaviour of the collapsing core of SN II is ruled by the relativistic degenerate electron gas and the nuclear matter. The linear approaching of *Boltzmann* equation of nuclear matter – the unchanging of full time derivative of classical distribution function, namely, the unchanging of the number of particles in the unit volume at phase space – conduces to the classical hydrodynamical differential equations, the mass-, momentum-, and energy-conservation (Ring & Schuck, 1980). It is valid for the relativistic degenerate electron gas as well, because of its *Fermi*-distribution function.

In our model of the SN II progenitor collapse practically we have to solve the classical, coupled, spherically symmetric, hydrodynamical differential equations of a perfect fluid in *Newtonian* gravitational potential.

We suppose that the matter of SN II can be modelled by an artificial fluid, which has density ρ putting together from two components – the ground state symmetric nuclear matter (ρ_{nm}), and the relativistic degenerate electron gas (ρ_e) – densities, while the pressure of the fluid is the sum of two partial pressure, the nuclear matter pressure $P_{nm}(\rho_{nm})$, and the electron gas pressure $P_e(\rho_e)$, namely

$$P(\rho) = P_{nm}(\rho_{nm}) + P_e(\rho_e), \qquad \rho = \frac{N_{nm}}{V} m_{nm} + \frac{N_e}{V} m_e, \tag{1}$$

where m_{nm}, and m_e is the mass of the typical nucleon of nuclear matter ($m_{nm} \simeq m_{p^+}$), and the mass of electron, the N_{nm} and N_e is the nucleon and electron number in the unit volume V.

On the basis of thermodynamic the EOS of nuclear matter can be deduced from the energy per nucleon E_A calculated from *Fermi*-gas model of ground state symmetric nuclear matter. Thus for the EOS we obtain

$$P(\rho_{nm}) = \frac{2}{3}\alpha\rho_{nm}^{\frac{5}{3}} - \beta\rho_{nm}^2 + \gamma(\sigma+1)\rho_{nm}^{(\sigma+1)}, \ \rho_{nm} = \rho\frac{1}{1+Y_e\frac{m_e}{m_{nm}}}, \tag{2}$$

where ρ_{nm} can be calculated from the artificial fluid density ρ, with the electron/nucleon ratio Y_e, $\alpha = 23MeV$, and the parameters σ, β, γ can be determined by heavy ion experiments. According to this experiments the nuclear

matter could be characterised by soft $\sigma = 1$, $\beta = 62.6MeV$, $\gamma = 23.6MeV$, or stiff $\sigma = \frac{1}{6}$, $\beta = 181MeV$, $\gamma = 142MeV$ EOS. Note that the numerical simulations have accomplished yet by many groups have showed that a successful SN II explosion occurred only in the case of using soft EOS.

The pressure of relativistic degenerate electron is the well known

$$P_e(\rho_e) = \frac{(3\pi^2)^{\frac{1}{3}}}{4}\hbar c\left(\frac{\rho_e}{m_e}\right)^{\frac{4}{3}}, \quad \rho_e = \rho\frac{1}{1+\frac{1}{Y_e}\frac{m_{nuc}}{m_e}}, \tag{3}$$

where ρ_e also can be calculated from the artificial fluid density ρ, with same electron/nucleon ratio Y_e like in eq. (2).

4. Simulation in 1 Dimension

In one dimensional simulation we try to examine just the behaviour of the symmetric nuclear matter, in respect what kind of an influence has the stiffness of the nuclear EOS on the raising distance of the bounce from centre. Becose of the weak temperature dependency of the energy per nucleon of the symmetric nuclear matter, at saturation density, we neglect the temperature, which means that we use a ground state nuclear matter (Bethe, 1990). In this conditions ($T = 0$) the differential equation of the energy-conservation has no additional physics in it, therefore we did not compute it. Thus in one dimension we have to solve the spherical symmetric continuity equation, and the *Eulerian* equation in *Newtonian* gravity.

The simulation was accomplished for various progenitor Fe-core mass, in range of $1-1.4M_{\odot}$, with the radius of $100Km$ sphere. The boundary conditions were the followings: perfect wall at the centre, and continuous, constant velocity infall at the surface of the core. The initial condition was a homolog state of the Fe-core ($\rho(r,\, t=0) \sim r^{-1/3}$, $v(r,\, t=0) \sim r^{1/2}$), which was set by the central density and infall velocity.

According to our simulations the homology of collapse breaks down after a couple of ms, in spite of the fact that we neglect the lepton physic ($T = 0$). Probably, this is because of the saturation part of the nuclear EOS, where the pressure of the fluid is growing very slowly while the density is increasing.

In both case soft or stiff nuclear EOS the central density always have maximal values of roughly $1-3\cdot 2.7\cdot 10^{14}\, g/cm^3$. In case of soft nuclear EOS the maximal central density was slightly higher than in case of stiff nuclear EOS. The bounce always occurred earlier in case if stiff nuclear EOS. But, surprisingly the bounce was born at a distance of $25Km$ from the centre of the star in both cases.

5. Simulation in 2 Dimension

The goal of this simulation is to understand the evolution of primordial perturbation at the appearance of the bounce. This is a very important question, because in the simulations looking forward to the evolution of prompt, or delayed shock, in respect weather what kind of an initial perturbation needs to get low mode number, high energy transporting convection flows, the initial condition have always chosen arbitrary (Kifondis et al., 1999). So, the main question is the correlation of the size of perturbation and its growth at the beginning of homolog collapse, before the bounce.

In this calculation we try to solve the two dimensional, spherical symmetric continuity, and the *Eulerian* equations of the two perpendicular momentum, in *Newtonian* gravity, neglecting the energy-conservation, because of the nuclear matter is supposed to be in ground state (T=0).

The simulated region and boundary conditions of simulation are the same as in one dimensional calculation, but there are two kind of questionable cases on initial condition: 1. symmetric inflow started with the unperturbed homolog core, 2. unsymmetrical inflow started with the perturbed homolog inflow. With this initial conditions I would like to find out whether the initial perturbation set at the beginning of the collapse will stay or dissappear causing problems for late time evolution of prompt shock simulations.

Acknowledgements

I would like to thank J. Németh for constructive remarks and useful suggestions during the writing of this paper.

References

Bethe, H. A., Rev. Mod. Phys., Vol 62 No.4, October 1990.

Cooperstein J., E. A. Baron, Supernovae: The Direct Mechanism and the Equation of State, edited by A. G. Petschek, Springer, New York, 1990.

Colgate A., C. Fryer, 1995, Phys. Rep., 256.

Herant, M., W. Benz, W. R. Hix, C. L. Fryer and S. A. Colgate, 1994, Astrophys. J. 435, 339.

Ring, P.,P. Schuck, The Nuclear Many-Body Problem, Semiclassical Methods in Nuclear Physics, Springer-Verlag, 1980, New York.

Kifondis, K., T. Plewa, H.-TH. Janka, E. Mller, astro-ph/9911407

Modelling of RR Lyrae instability strips

Róbert Szabó and Zoltán Csubry
Konkoly Observatory
H-1525 Budapest, P.O.Box 67., Hungary
E-mail: rszabo@konkoly.hu

Abstract

Recent studies indicates that the slope of the empirical blue edge of the RR Lyrae fundamental mode instability strip is irreconcilable with the theoretical blue edges. Nonlinear hydrodynamical pulsational code involving turbulent convection was used to follow fundamental/first overtone mode selection mechanism. This method combined with the results of horizontal branch evolutionary computations was applied to rethink the problem.

Keywords: variable stars, RR Lyrae, evolution, turbulent convection, hydrodynamics*PhD konferencia: csillagaszat, asztrofizika*

1. Introduction

The main motivation to model the behaviour of RR Lyrae stars numerically is at least twofold. These population II. radial pulsators are fundamental milestones of establishing distance scales, as well as cosmological timescales and excellent test objects for evolutionary calculations. The second point is that we would like to be sure about the physics governing the stars. For example we aim to improve our knowledge of convective turbulence and apply more sophisticated convection recipes than the present ones. Pulsation theory also benefits from these results.

2. Blue edge of the fundamental instability strip - the problem

Recent works provided homogeneous data sets of physical parameters of RR Lyrae stars (Kovács & Jurcsik, 1996), (Kovács & Jurcsik, 1997), (Jurcsik, 1998). The method they developed is based on the extraction of the absolute magnitudes, colors, effective temperatures and metallicities directly from the observed RRab periods and light curves. Unfortunately such relations are not available for RRc stars. These works also revealed empirical relations between luminosity L, stellar mass M and metallicity Z. Theory takes part only in transforming M_V and $B-V$ to L and T_{eff} via Kurucz's static model atmospheres.

The resulted empirical HRD was compared to linear pulsational models (Kolláth et al., 2000a). Both radiative and convective models failed to explain the steep slope of the blue edges of the fundamental mode (FM)and first overtone (1o) instability strips (Fig. 1). Applying turbulent convection resulted only in a slight overall shift in the position of the line that separates 1o and FM pulsators. The authors investigated many physical effects and assumptions that might change the slopes (rotation, exotic chemical abundances, radiative transport), but they found no hints for *differential* variation of the slope.

3. A possible explanation: modal selection and evolution

After exhausting all physical possibilities concerning linear pulsational models (Kolláth et al., 2000a), a detailed, nonlinear, hydrodynamical survey combined with the latest horizontal-branch (HB) evolutionary sequences was carried out to investigate further this problem. Why do we think that this could help? The answer is modal selection: it's well known (Buchler & Kovács, 1986) that in the cases of both Cepheids and RR Lyrae stars amplitude equations predict either-or-regions (EoRs) on the HRD verified by state-of-the-art numerical hydrodynamical calculations (Kolláth & Buchler, 2000). This means that if the star evolves from low temperatures to high temperatures (blueward) in this region it is seen as a FM pulsator (RRab), while evolving to the opposite direction results in a 1o pulsator (RRc) with the same stellar parameters (mass, luminosity, etc.) (Fig. 2a). As stars with different metallicities evolve through this region at different luminosities a mixed area containing both RRab and RRc stars is formed (EoR), and the mode selection can change the *average slope*.

In order to explore the mode selection characteristics in numerical RR Lyrae models, we used the so-called Florida-Budapest code, which is a sophisticated,

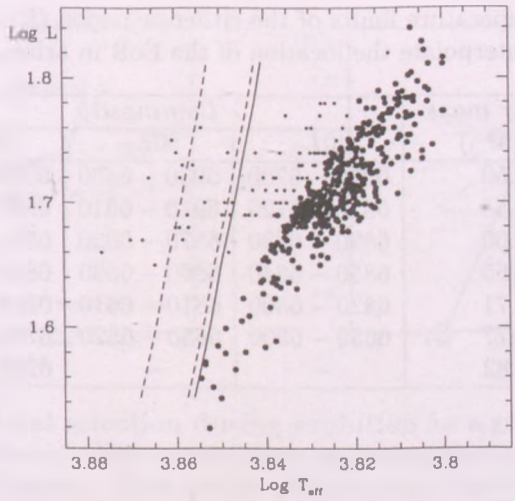

Figure 1: Empirical *Log L – Log* T_{eff} plot: RRab (large dots) and RRc (small dots) stars. Theoretical FM radiative blue edge (***solid line***), and the shift of the convective FM blue edge (***dashed lines***) corresponding to different turbulent parameter sets are indicated.

Table 1: Standard model parameter set

	Convective turbulence							*Composition*	
Parameter	α_l	α_{cc}	α_n	α_s	α_p	α_t	α_d	X	Z
Value	0.41	0.75	1.0	0.75	2/3	1.0	4.0	0.75	10^{-4}

nonlinear hydrocode including turbulent convection and tailored to follow stellar pulsation (Kolláth et al., 2000b). Turbulent convection parameters were chosen to match to the observed amplitudes and periods (Table 1). A constant representative metallicity was used ($Z = 0.0001$), because earlier investigations (Szabó et al., 2000) revealed that the shape and the location of the double-mode region and EoR are almost independent of metallicity.

First the width of the EoR for a given luminosity and mass was determined as

Table 2: The temperature limits of the either-or-region (K). These grid points were applied to interpolate the location of the EoR in arbitrary points.

Stellar mass $M(M_\odot)$	*Luminosity*		
	$40L_\odot$	$50L_\odot$	$60L_\odot$
0.50	6950 – 6700	6930 – 6430	6950 – 6420
0.55	6920 – 6720	6910 – 6610	6930 – 6520
0.60	6890 – 6680	6870 – 6620	6880 – 6550
0.65	6850 – 6640	6860 – 6630	6840 – 6550
0.71	6820 – 6500	6810 – 6610	6810 – 6590
0.77	6650 – 6300	6650 – 6520	6780 – 6570
0.82	–	–	6700 – 6520

follows: After building a static model, hydrodynmical calculations were initiated with perturbation of different linear combinations of the FM/1o eigenvectors. Modal behaviour was determined using the amplitude-amplitude diagram ($A_0 - A_1$, FM-1o amplitude diagram). In each sequence for a given stellar mass we made a successive approximation to find the limits of the EoRs to an acceptable accuracy ($5 - 10K$). Table 2. contains the computed grid points we used to cubic spline interpolate the width of EoR.

Then recent theoretical horizontal branch evolutionary tracks (Demarque et al., 2000) (http://achee.srl.caltech.edu/star.html) were chosen and re-interpolated in time. The pulsational state corresponding to every evolutionary track points was determined by taking into account the EoR widths and the direction of evolution. Outside the EoR every point was considered as FM or 1o pulsator depending on its effective temperature. The luminosity and mass range were $1.60 < LogL < 1.78$, and $0.445M_\odot < M < 0.90M_\odot$, respectively. The compositions of the relevant tracks are $Y = 0.24$ and $Z = 0.0004, 0.001, 0.004$. Combining these pieces of information *synthetic HRD* was constructed. Uniform mass and age distribution were applied, because (1) we have very sparse information about these distributions of the observed stars, (2) age and mass distributions have nothing to do with the instability strip boundaries, given the mixed nature of the observed sample; only a more realistic star density could be reproduced on the diagram.

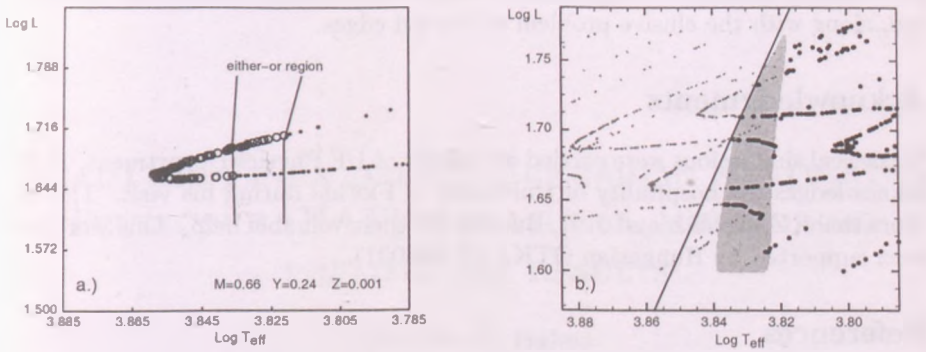

Figure 2: **a.) Modal selection during evolution** for a given model between 23.3-92.0 Myrs (from ZAHB): small points show fundamental; large circles denote overtone pulsation. Track points are uniformly distributed in time. **b.) Combined effect of modal selection and evolution.** The slope of the empirical fundamental blue edge is indicated by straight line. The shaded area shows the extent of the either-or-region. Representative evolutionary tracks are plotted. Small dots represent 1o pulsators, big points show FM RR Lyrae.

4. Results

The final graph is shown in Fig. 2b. One can see a better agreement between empirical and theoretical slopes than before. Theoretically no distinct blue edge is expected when stars with different metallicities and ages are included. A well defined either-or-region is seen instead. In other words the slopes depend on metal contents. The slope of the observable blue edge also depends slightly on the completeness of the diagram (number of plotted or observed stars), practically it is equivalent to the envelope of the RRab stars.

There is still a small discrepancy at the lower luminosity regime. This can be due to the smaller sample of low-luminosity stars (observational bias) and higher uncertainties of the models and the empirical transformations. The almost exact fit of the boundary of the shaded area in a fairly large luminosity interval is indeed a coincidence, because adjustment of the convective parameters causes horizontal shift.

First overtone blue edges are not considered here. From observational point of view there are too few observed stars there with rather large error-bars. This

prevents any conclusive comparisons. Future works should address this question, too, along with the elusive problem of the red edges.

Acknowledgments

Numerical simulations were carried out partly at UF Physics Department. R.Sz. acknowledges the hospitality of University of Florida during his visit. The authors thank Z. Kolláth and J. R. Buchler for their valuable help. This work has been supported by Hungarian OTKA (T-026031).

References

Buchler J.R & Kovács G. 1986, ApJ 308, 661

Buchler J.R. 2000, Nonlinear Pulsations of Convective Stellar Models in The Impact of Large-Scale Surveys on Pulsating Star Research, Eds. L. Szabados & D. Kurtz, ASP Conference Series, 203, 374-375

Demarque, Zinn, Lee, & Yi 2000, AJ, 119, 1398

Kovács G. & Jurcsik J. 1996, ApJLett 466, L17

Kovács G. & Jurcsik J. 1997, A&A 322, 218

Jurcsik J. 1998, A&A 333, 571

Kolláth Z., Buchler J.R. & Feuchtinger M. 2000a, ApJ 540, 468

Kolláth Z., Buchler J.R., Szabó R. & Csubry Z. 2000b, Nonlinear Beat Cepheid and RR Lyrae Models, ApJ to be submitted

Kolláth Z. & Buchler J.R. 2000c, Double Mode Stellar Pulsations in Nonlinear Studies of Stellar Pulsations, Eds. M. Takeuti & D.D. Sasselov, Astrophysics and Space Science Library Series, Kluwer (in press)

Szabó R., Csubry Z., Kolláth Z. & Buchler J.R. 2000, Nonlinear Survey of RRd Models, in The Impact of Large-Scale Surveys on Pulsating Star Research, Eds. L. Szabados & D. Kurtz, ASP Conference Series, 203, 374-375.

RealTime Linux driven Hungarian Automated Telescope (HAT) for all sky monitoring: preliminary results

Gáspár Á. Bakos
Konkoly Observatory
H-1525 Budapest, P.O.Box 67., Hungary
E-mail:bakos@konkoly.hu

Abstract

As projects employing many small telescopes instead of a single big instrument are flourishing, it is vital to develop cheap, general purpose, fast response, Internet-accessible, optionally networked robotic telescopes. The Hungarian Automated Telescope (HAT) fulfills all the aforementioned criteria, mainly by the use of freeware Realtime Linux OS, SQL relational database and flexible Tcl language. HAT is used to monitor the sky, mainly concentrating on variable stars. The present summary discusses some features of the system and preliminary results.
Keywords: *Catalogs - Stars:variables - Surveys*

1. Introduction

Only few percent of the stars are variable, yet a great fraction of variables brighter than $I \approx 13$ are to be discovered. Charge Coupled Devices (CCDs) attached to *very small* telescopes can be capable of this, provided the observation and data reduction is fully automated (Paczyński 2000).

The byproduct of current surveys focusing on alerts (such as ROTSE, SuperLotis, etc.) is already a list of couple of thousand new variable stars. The All-Sky Survey (ASAS, Pojmański 1997, 1998, 2000) discovered 3900 new variables with a 135mm telephoto lens and an amateur CCD.

2. Overview of HAT

The main philosophy of construction is to substitute hardware tasks with quality software. A single, noname PC in itself acts as the clock-drive, it is responsible for positioning the mount, controlling the CCD and dome (via RTLinux kernel-drivers), scheduling projects using a local or remote database (SQL), carrying out data reduction, loading results on the Web, or retrieving alerts from other sites.

The instrument consists of a friction-drive horseshoe mount similar to the ASAS mount (Pojmański 1997), which is able to host telescopes up to $\sim 25cm$. The mount contains two five-phase stepper motors for the right ascension and declination axes (for high precision tracking, and gotoing), A simple signal converter electronics is responsible for driving the motors via converting the signals emitted through the PC's parallel port.

We use a Nikon 180mm, f/2.8 lens ("0.06m telescope"), which has perfect image, though vignetting is noticeable. The CCD is the cheapest possible medium-sized amateur camera: Meade Pictor 416xt, with 512×768 px. dimension. Other computer controlled accessories include lens heating, rain-detector, domeflat light and switchboard (for turning off the power with computer control). All devices are controlled via parallel or serial port.

The use of SQL database and TCP/IP allows centralized information sharing between HAT or other sites, which can be built up in any preferred topology. Virtually any kind of observing program can be formulated (in Tcl script language) and executed after a priority based scheduling, making the mount suitable for a wide range of automated projects such as all-sky monitoring or GRB follow-up.

3. Preliminary results

In addition to the technical details, we present early results of monitoring variable stars from Hungary. The observing site was the roof of Konkoly Observatory at the increasingly light-polluted Budapest. Roughly three months were devoted to testing, and a dozen of clear nights for real observations.

Limiting magnitude under grey sky, with 4 minute exposure was $I \sim 13.5^m$. A list of bright variables was monitored so as to find out the capabilities of the system.

Table 1: Observed variables with HAT from Budapest. Columns give the variable name, maximum and minimum brightness, period, type, exposure time, and number of frames, respectively.

Name	V_{max}	V_{min}	P (day)	Type	T_{exp} (sec)	N
VWCEP	7.8	8.2	0.278300	EW	60	73
DQCEP	7.4	7.5	0.078880	dSct	60	69
GKCEP	6.9	7.5	0.936170	EB	40	52
CMLAC	8.5	9.6	1.604691	EA	120	56
YLAC	8.7	9.5	4.323788	CEP	120	41
ABAND	10.4	11.3	0.333000	EW	180	119
ACAND	10.6	11.6	0.525120	RRab:	270	137
SWAND	9.3	10.8	0.442279	RRab	240	77
CCAND	9.4	9.8	0.124907	dSct	240	107
SUCAS	6.3	7.0	1.949200	CEP	30	54
XARI	9.2	10.6	0.651139	RRab	180	44
RXCAM	8.3	9.6	7.912000	CEP	120	12
ARPER	9.9	10.8	0.425549	RRab	180	84
RTAUR	5.5	6.7	3.728000	CEP	30	12
ADGEM	9.5	10.2	3.788000	CEP	210	7
SZLYN	9.1	9.6	0.120500	dSct	180	17
TTLYN	9.9	10.0	0.597400	RRab	210	12

We feature variable CC And, so as to demonstrate the capacity of such a small instrument. The light curve (versus phase) without deselecting *any* data point is presented on Fig. 1. After fitting a double sine of the form

$$I(t) = A_0 + A_1 \sin(f_1 t + \phi_1) + A_2 \sin(f_2 t + \phi_2), \qquad (1)$$

the residuals were less than 0.02^m. Further Fourier analysis of the light curve revealed further frequencies besides the main frequency $f_1 = 8.0005$cyc/day: $f_3 = 7.8189544$ and $f_4 = 6.5938568$. Frequency f_3 is first mentioned by Fitch

(1960), and based on observations with a 0.5m–1m telescopes plus photometers. The other frequency, f_4 is neither mentioned in Fitch (1967), nor in Fu & Jiang (1995).

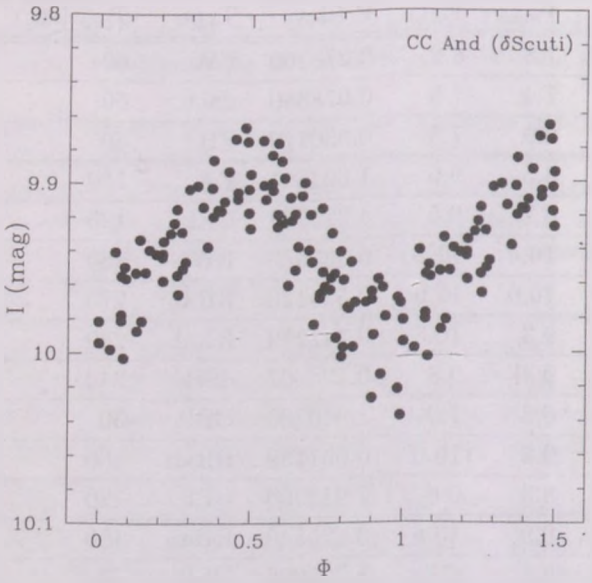

Figure 1: Light curve of CC And. Note the small amplitude, and the natural width of the curve due to the multiperiodic behavior of the variable.

4. Budget

The costs of such a project is crucial when the goal is to install as much automated stations as possible. Our aim was to demonstrate that valuable scientific work can be done with small budget, effective group and good quality software substituting enhanced hardware requirements. The total costs in US Dollars are as follows: camera (1600), lens (500), PC (800), mount (5000), dome (1000). It is the manpower and software that hides the most costly part: one year's work of four people.

Acknowledgments

This project is done in collaboration with Prof. Bohdan Paczyński from Princeton University and Dr. Grzegorz Pojmański from Warsaw University Astronomical Observatory by a small group. Partial funding for this project is provided by Mr. William Golden. Group members are: József Lázár (software engineer), István Papp (electric engineer), Pál Sári (structural design) and the author.

It is my pleasure to return thanks for the hospitality of Konkoly Observatory, Dr. Lajos Balázs (director), Dr. Géza Kovács (phd advisor of the author), Dr. Johanna Jurcsik and András Holl (system manager). Further acknowledgements are due to Gábor Fűrész (JATE) for his committed help in the beginning of this project.

References

Pojmański, G. 1997, Acta Astronomica 47, 467

Pojmański, G. 1998, Acta Astronomica 48, 35

Pojmański, G. 2000, Acta Astronomica 50, 177

Paczyńkis, B. 2000, PASP, 112, 1281

Fitch, W. S. 1960, ApJ, 132, 701

Fu, J.-N. and Jiang, S. Y. 1995, A&AS, 110, 303

Archaeoastronomy in Transylvania

Iharka Csillik[1], Oproiu Tiberiu[1], Chiş Dorin[1]
Maxim Zoie[2], Lazarovici Gheorghe[2]
[1] "Babeş–Bolyai" University, Astronomical Observatory
[1]3400 Cluj-Napoca, str. Cireşilor, nr. 19, Romania
[2]The National Historical Museum of Transylvania
[2]3400 Cluj-Napoca, str. C. Daicoviciu, nr. 2, Romania
E-mail:[1]iharka@math.ubbcluj.ro

Abstract

The paper presents some astronomical considerations on the orientation of graves and other ancient vestiges on the Transylvanian territory, which – we prove – are mainly aligned with respect to the solar phenomena.
KEYWORDS: *archaeoastronomy*

1. Introduction

Archaeoastronomy compelled recognition especially by determining the orientation of some alignments of ancient vestiges, connecting them with astronomical events at the horizon of the respective site, and then deducing certain customs, rituals and beliefs of the people that had built them, or at least some information on their astronomical knowledge.

The paper presents our research concerning the orientation of graves and other vestiges on the Transylvanian territory, which are mainly aligned with respect to solar phenomena.

1.1. The Neolithic burial site Iclod

We start with the presentation of the graves in the Neolithic burial site Iclod near Cluj-Napoca dated 4200 BC.

The Neolithic burial site Iclod was discovered by Márton Roska at the beginning of the 20th century. The dead person was buried on his back facing the

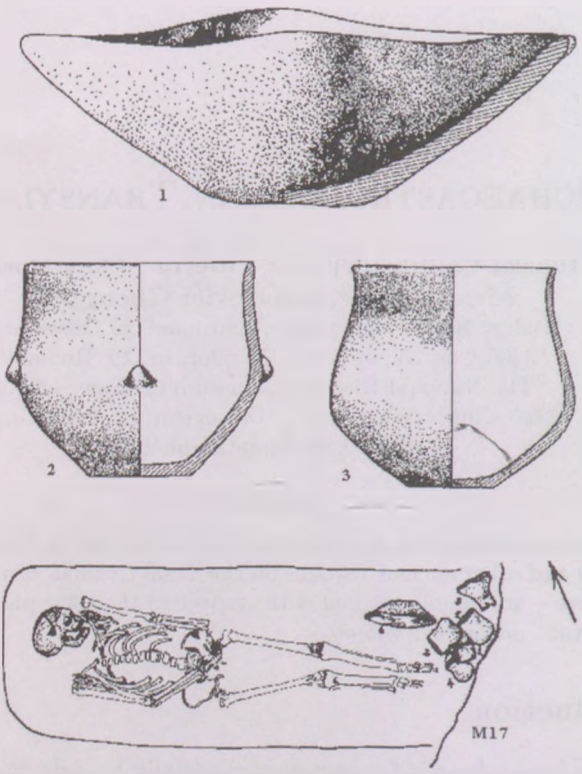

Figure 1: The M17 grave with the typical earthen pot

sunrise direction. Inside the graves, from the later stage of Iclod culture, near the skeleton there were found tools made of stone, bone and obsidian.

The astronomical problem of graves orientation was similar to those for the Tiszapolgár–Bodrogkeresztúr (Hungary), Gomolova and Mokrin (Yugoslavia), Cernica (Romania) necropolises.

First, we determined the Sun azimuth for Iclod, corresponding to summer and winter solstices. Considering the geographical latitude of Iclod (φ=46°59'.8), we found an accuracy of 1 degree that the Sun azimuth measured from the North is $A_1 = 53°$ for the summer solstice and $A_2 = 126°$ for the winter solstice.

We prove that 72% of the graves found here are oriented within the rigorous

limits of the annual oscillation of sunrise azimuth.

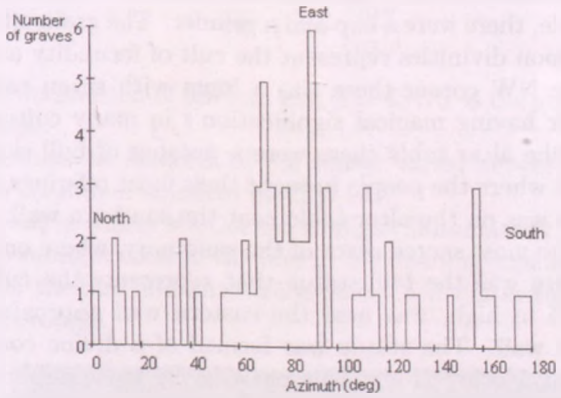

Figure 2: The distribution of graves orientation

The graves, whose orientation is out of the annual oscillation of sunrise azimuth belong to the last stage of Iclod culture, when the eastern orientation was replaced with a northern one.

1.2. The Neolithic sanctuary of Parţa

We continue with the presentation of the orientation of the Neolithic sanctuary Parţa, near Timişoara.

The excavations were started by Joachim Miloja in 1931 and were continued by other archaeologists. The sanctuary of Parţa belongs to the Banat culture from the period 4600–4200 BC. Now, the sanctuary of Parţa is reconstructed in the Banat Museum in Timişoara.

The size of the sanctuary was $11.6 \times 6 \times 1.75$ m and its longest axis was oriented in the East–West direction. The sanctuary was divided in two rooms by a wall. Room A in the Eastern part of the sanctuary was 5 m in length and room B from the West part was 5.6 m long. On this dividing-wall it was a round window-like opening approximately 35 cm in diameter at 1 m from the floor and 2.25 m from the northern wall. In the center of the sanctuary there was found a big altar table that was 25 cm thick and it extended 2.5 m in length in both rooms. The sanctuary had a circular opening on western wall – probably representing the Sun – approximately 30 cm in diameter, at 1.35 m from the floor and 1.5 m from the northern wall. Surrounding this circular opening where

the light entered in the sanctuary, in the exterior part of the wall, an earthen Moon-shaped adornment about 8 cm thick was fastened. Fixed against the same wall, under the hole, there were a cup and a grinder. The grain offerings brought to the Sun and Moon divinities represent the cult of fecundity and fertility.

In room A the NW corner there was a loom with seven earthen weights. Seven is a number having magical signification's in many cultures. Near the northern wall on the altar table there were a number of bull skull ornaments. This was the place where the people brought their meat offerings. The place for the grain offerings was on the altar table near the southern wall.

Room B was the most sacred place of the sanctuary, where only the shaman was allowed. There was the bull-statue that represents the cult of the bull. The bull-idol, 1.75 m high, was near the eastern wall approximately 3.05 m from the northern wall. The statue was formed of a divine couple: the Bull God and the Great Mother God. This piece is the most important object in the sanctuary. The bull statue was facing East and it was on the 0.9 m high socle. The archaeologists suppose that on the socle there was also an amphora containing sacred liquid or food devoted to the deities. In room B, on the altar table a fish-tray was found.

From the astronomical viewpoint, we prove that the light of sunset entered the sanctuary on the western wall through the Sun-Moon circular opening and through the hole in the dividing wall and illuminated the NW corner of the socle or the amphora on the socle.

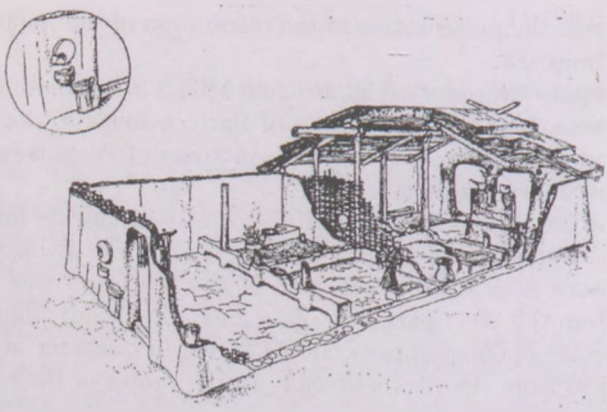

Figure 3: The sanctuary of Parţa. Southern view

The azimuth A of sunset is given by:

$$\cos A = -\frac{\sin \delta}{\cos \varphi}$$

where, δ is the declination of the Sun and $\varphi = 45°75'$ is the geographical latitude of the site Parţa.

We obtain that the azimuth of the sunset varied between 234° (winter solstice) and 305° (summer solstice) in 4200 BC.

We prove that in winter solstice the sunlight illuminated the loom, in autumn and spring the sunlight entered the hole in the dividing wall and fell on the socle. During summer the Sun illuminated the place on the altar table where the grain offerings were brought.

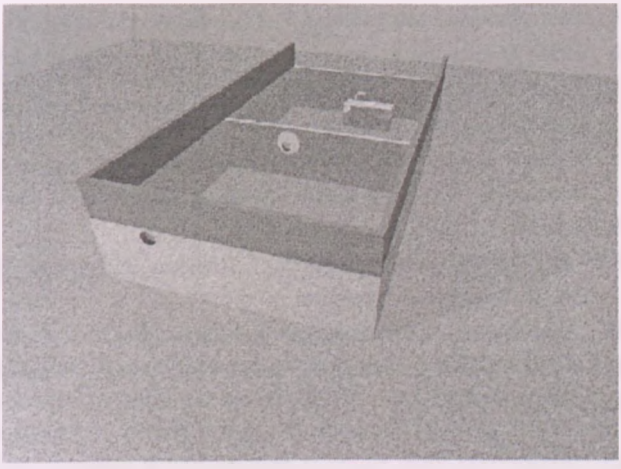

Figure 4: The illuminated socle

Interesting is the fact that the vernal point was in the constellation of Taurus, while in spring the Sun illuminated the socle of the bull-statue. From these facts one can infer that the people from the sanctuary of Parţa had a very good astronomical knowledge.

The general conclusion is that the Sun is the celestial object that stimulated cultic actions in nearly ancient cultures – pyramids, temples, megalithic sites, Neolithic graves, etc. are aligned with respect to solar phenomena.

Acknowledgments

Thanks to Dr. Barlai Katalin and to our colleague Radu Zapotinschi for their help and advice.

References

Barlai K., 1980, Archaeoastronomy VIII, 29

Barlai K., Bognár-Kutzián I., 1995, Current Problems and Future of Archaeoastronomy 2, 25

Cantacuzino Gh., Morintz S., 1963, Dacia VII, 27

Cantacuzino Gh., Morintz S., 1969, Dacia XIII, 45

Comşa E., 1995, Acta Musei Napocensis 32(I), 257

Lazarovici Gh., 1985, Revista Muzeelor si Monumentelor XXI(8), 36

Lazarovici Gh., 1986, Document recent descoperit şi informaţii arheologice, 12

Lazarovici Gh., Kalmar Z., 1986, Apulum XXIII, 25

Lazarovici Gh., Kalmar Z., 1987, Apulum XXIV, 9

Lazarovici Gh., Kalmar Z., 1988, Apulum XXV, 9

Lazarovici Gh., Kalmar Z., 1993, Apulum XXVII-XXX, 23

Lazarovici Gh., Maxim Z., 1993, Ibiscum VIII, 41

Roska, M., 1942, Erdély régészeti repertóriuma I, Őskor, Kolozsvár

Schlosser W., 1989, Publ. Astron. Strasbourg 3, 79

Vince A., 1998, Publ. Astron. Obs. Belgrade 60, 230

Vince A., Jovanović B., Vince I., Vince O., 1996, Publ. Astron. Obs. Belgrade 54, 199

Wittmann A., 1979, A&A 73, 129

CCD PHOTOMETRIC INVESTIGATIONS OF SMALL BODIES IN THE SOLAR SYSTEM

Gyula Szabó and László L. Kiss
Department of Experimental Physics, University of Szeged
H-6720 Szeged, Dóm tér 9., Hungary
E-mail: szgy@neptun.physx.u-szeged.hu

Abstract

We present photometric analyses of two high-amplitude minor planets (1627 and 1865) resulting in approximate models of shape and rotation. Three distant (R=5.5–7.2 A.U.) comets are discussed concerning their major morphological parameters*.
KEYWORDS: *solar system: comets, asteroids*

1. Introduction

The new observing strategies using fully automatic telescopes and dedicated large instruments led to regular discoveries of a wealth of relatively bright asteroids, moderately faint comets and other interesting small bodies in the solar system with ambiguous characteristics. With the advent of the CCD era it has become possible to study much fainter objects than previously. The photometric methods of asteroid modelling are based on multi-opposition lightcurves of full phase coverage obtained at very different longitudes (De Angelis (1993), Detal et al. (1994)). We started a long-term observational project in 1998 with the primary purpose of obtaining accurate CCD lightcurves of poorly studied minor planets. The main programme is dedicated to asteroids with available two-opposition lightcurves, where a third lightcurve enables the complex analyis. Additional targets are those asteroids with no previous photometric measurements. The first results have already appeared in Sárneczky et al. (1999) and

*Based on observations taken at the German-Spanish Astronomical Centre, Calar Alto, operated by the Max-Planck-Instiute for Astronomy, Heidelberg, jointly with the Spanish National Commission for Astronomy

Kiss et al. (1999). In the first part of this paper we present photometric analyses of two high-amplitude minor planets resulting in their models of shape and rotation.

The overwhelming majority of cometary studies is based on ground-based or space observations of bright comets around or near to their perihelion. Direct imaging reveals the inner structures of the coma, which usually hides the nucleus itself. There has been a small number of papers dealing with distant ($R \geq 5$ AU) comets (e.g. O'Ceallaigh et al. (1995), Lowry et al. (1999)), and consequently, there is a serious lack of information on the behaviour of these objects. On the other hand, time-series observations may give constraints on the period of rotation and related effects - Jewitt (1992). The main aim of our work is to contribute this topic with new CCD observations of three comets located between 5.5–7.2 AU – C/1999 J2 (Skiff), C/1999 N4 (LINEAR) and C/2000 K1 (LINEAR).

2. Observations

Observations have been made on two different observing sites. Johnson V and R_C filtered CCD observations were carried out at Calar Alto Observatory (Spain) on 10 nights in June–July, 2000. The instrument used was the 123/981 cm Cassegrain-telescope equipped with the SITe#2b CCD camera (2048x2048 pixels giving an angular unbinned resolution of 0.49″/pixel). The projected sky area is $16' \times 16'$, $10' \times 10'$ unvignetted.

Continuous R_C filtered CCD observations were carried out at the Piszkéstető Station of Konkoly Observatory during 1998-2000. The data were obtained using the 60/90/180 cm Schmidt-telescope equipped with a Photometrics AT200 CCD camera (1536x1024 KAF 1600 MCII coated CCD chip). The projected sky area is $29' \times 18'$ which corresponds to an angular resolution of 1.1″/pixel.

3. Minor planet photometry

3.1. 1627 Ivar

This Earth-approaching asteroid was discovered by E. Hertzsprung in Johannesburg, on September 25, 1929. Beside a few photometric data series (see references in Kiss et al. (1999)) there is a radar measurement by Ostro et al. (1990). Our observations were made at Piszkéstető only. We have determined a sinodic period of 4.80±0.01 h being in perfect agreement with earlier results.

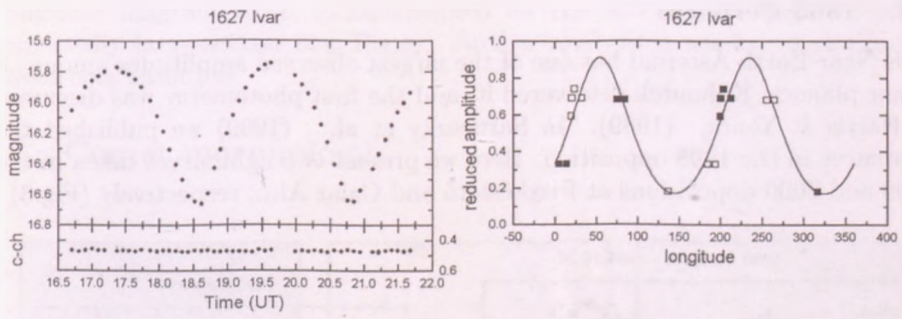

Figure 1: Left: the R lightcurve on Jan. 22, 1999; right: the reduced amplitudes vs. longitudes with the determined fit for 1627 Ivar

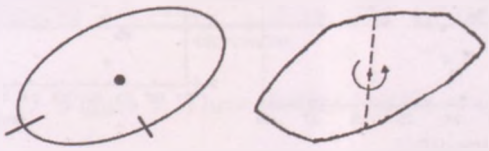

Figure 2: A pole-on view of the photometric model (left) and radar profile (right) of 1627 Ivar.

The amplitude varied between 0.8 and 1.0 mag during the different observing runs (1998 and 1999). A sample lightcurve is plotted in the left panel of Fig.1.

The shape of 1627 was modelled with an AM-method developed by Michałowski (1993). After collecting all available data, the observed amplitudes were reduced to zero solar phase. We have fitted the amplitude variations along the longitude. The resulting parameters of the model triaxial ellipsoid are: a/b=2.0±0.1, b/c=1.09±0.05. The ecliptic coordinates of the spin vector are: $\lambda_p = 145/325 \pm 8°$, $\beta_p = 34 \pm 6°$. The reduced amplitudes with the determined fit is presented in the right panel of Fig.1. The reliability of this model was tested by a direct comparison with radar images of Ostro et al. (1990). The similarity is evident (Fig.2). Therefore, we can rely on this (and similar) simple photometric methods when studying farther minor planets, which are beyond the capabilities of radar measurements.

3.2. 1865 Cerberus

This Near-Earth Asteroid has one of the largest observed amplitudes among all minor planets. Kohoutek discovered it, and the first photometry was discussed in Harris & Young (1989). In Sárneczky et al. (1999) we published the lightcurve in the 1998 opposition. Here we present two lightcurves taken in the 1999 and 2000 oppositions at Piszkéstető and Calar Alto, respectively (Fig.3).

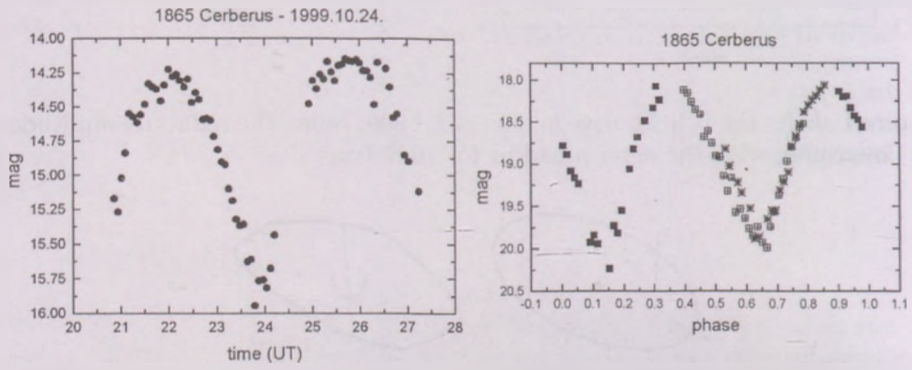

Figure 3: Two lightcurves of 1865 Cerberus: a single-night observation during the 1999 opposition (left) and the composite phase diagram obtained in 2000 (right). Note the 4 mag difference in the mean brightness.

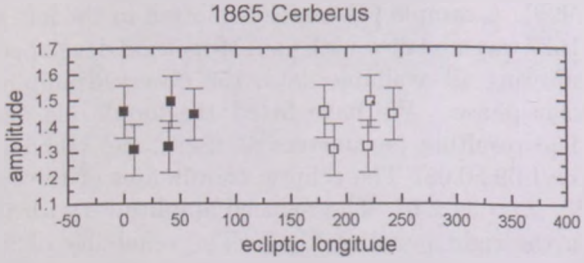

Figure 4: The amplitude-longitude diagram of 1865 Cerberus.

A preliminary analysis is being undertaken addressing the shape and rotation. Unfortunately, the first impressions are confusing, because the amplitude-

longitude diagram seems to be unsuited for the AM-method due to the unexpectedly large scatter (see Fig.4). Further analysis is needed to clarify this disturbing situation.

4. Comet morphology

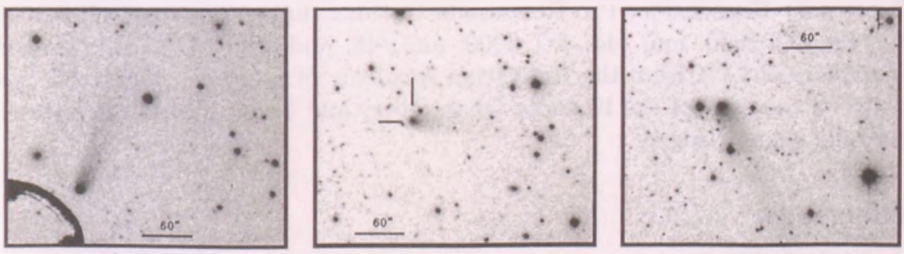

Figure 5: Three distant comets

Three comets located between 5.5–7.2 AU – C/1999 J2 (Skiff), C/1999 N4 (LINEAR) and C/2000 K1 (LINEAR) were observed in July, 2000 at Calar Alto Observatory. Beside the absolute VR_C photometry we took time-series observations in order to detect rotational effects. As can be seen in Fig.5, despite the large solar distances, the observed comets are fairly active. The general appearance is dominated by a small circular coma and a faint, considerably long tail. The presented images were enhanced to emphasize the faint tail extensions. The apparent tails are as long as 2.4′ (C/1999 J2), 1.0′ (C/1999 N4) and 3.6′ (C/2000 K1), though it was impossible to determine the faint ends accurately. The measured position angles (PA) are the following (antisolar directions in parentheses): C/1999 J2 – PA 18° (PA 80°); C/1999 N4 – PA 97° (PA 111°); C/2000 K1 – PA 150° (PA 102°). One can find large difference in C/1999 J2 and a smaller one in C/2000 K1 implying a significant amount of tail curvature in these comets. Neglecting this curvature we calculated the corresponding linear lengths taking into account the projection effect. The results are $7.5 \cdot 10^5$ km (C/1999 J2), $3.2 \cdot 10^5$ km (C/1999 N4) and $12 \cdot 10^5$ km (C/2000 K1), which are far from being typical at such large distances. We note that these values are only order of magnitude estimates because the curvature may alter the real lengths quite seriously at such large distances.

Time-series data revealed only small-amplitude, ambiguous variations, therefore, no firm conclusion could be drawn on the rotation of the nuclei. More results will appear in Szabó et al. (2001).

Acknowledgments

This research was supported by the Hungarian OTKA Grant #T032258, Szeged Observatory Foundation, Pro Renovanda Cultura Hungariae Grants DT 2000. máj./43., DT 2000. máj./44., DT 2000. máj./48. and "Bolyai János" Research Scholarship of LLK from the Hungarian Academy of Sciences. The warm hospitality of the staff of the Konkoly Observatory and Calar Alto Observatory is gratefully acknowledged.

References

De Angelis G., 1993, P&SS 41, 285

Detal A., Hainaut O., Pospieszalska-Surdej A., Schils P., Schoeber H.J., Surdej J., 1994, A&A 281, 269

Harris A.W., Young J.W., 1989, Icarus 81, 314

Jewitt D., 1992, in: Observations and Physical Properties of Small Solar System Bodies, ed. A. Brahic, J. Gerard & J. Surdej, Liége: Inst. Astrophys., 85

Lowry S.C., Fitzsimmons A., Cartwright I.M., Williams I.P., 1999, A&A 349, 649

Kiss L.L., Szabó Gy., Sárneczky K., 1999, A&AS 140, 21

Michałowski T., 1993, Icarus 106, 563

O'Ceallaigh D.P., Fitzsimmons A., Williams I.P., 1995, A&A 297, L17

Ostro S.J., Campbell D.B., Hine A.A. et al., 1990, AJ 99, 2012

Sárneczky K., Szabó Gy., Kiss L.L., 1999, A&AS 137, 363

Szabó Gy., Csák B., Sárneczky K., Kiss L.L., 2001, A&A, submitted